EFFECTS OF OFF-AXIS MELT SUPPLY AT FAST-SPREADING MID-OCEAN RIDGES: A STUDY OF THE 9°-10°N REGION OF THE EAST PACIFIC RISE

by

DOUGLAS TROY DURANT

A DISSERTATION

Presented to the Department of Geological Sciences
and the Graduate School of the University of Oregon
in partial fulfillment of the requirements
for the degree of
Doctor of Philosophy

June 2011

DISSERTATION APPROVAL PAGE

Student: Douglas Troy Durant

Title: Effects of Off-Axis Melt Supply at Fast-Spreading Mid-Ocean Ridges: A Study of the 9°-10°N Region of the East Pacific Rise

This dissertation has been accepted and approved in partial fulfillment of the requirements for the Doctor of Philosophy degree in the Department of Geological Sciences by:

Dr. Douglas R. Toomey	Chairperson
Dr. Paul J. Wallace	Member
Dr. Eugene Humphreys	Member
Dr. James Isenberg	Outside Member

and

Richard Linton	Vice President for Research and Graduate Studies/Dean of the Graduate School

Original approval signatures are on file with the University of Oregon Graduate School.

Degree awarded June 2011

DISSERTATION ABSTRACT

Douglas Troy Durant

Doctor of Philosophy

Department of Geological Sciences

June 2011

Title: Effects of Off-Axis Melt Supply at Fast-Spreading Mid-Ocean Ridges: A Study of the 9°-10°N Region of the East Pacific Rise

Approved: _____
Douglas R. Toomey

Results from a recent mid-ocean ridge tomography study along the fast-spreading, northern East Pacific Rise (EPR) reveal that the axis of mantle upwelling beneath the ridge is skewed with respect to the spreading axis, giving rise to regions of both rise-centered and off-axis mantle melt accumulation. Here, we investigate the effects of off-axis melt accumulation on the architecture of overlying crust as well as off-axis melt delivery on crustal construction along the ridge axis. We first present evidence for off-axis magmatism 20 km from the spreading center in 300-ka-old crust overlying a region of off-axis melt supply. Seismic data reveal an intrusive complex ~2 km beneath the seafloor that is limited in lateral extent (<5 km) and comprises a melt lens underlain by low-velocity, high-attenuation crust, which provides the necessary conditions to drive off-axis volcanic and hydrothermal activity. We next present results from thermodynamic modeling that show systematic, along-axis variations in the depth of crystallization and degree of differentiation of magma produce crustal density variations of ~0.1 g/cm^3. These density anomalies are on the order inferred from a recent study that shows increasing axial depth along the northern EPR correlates with an increase in

crustal density and offset of mantle upwelling with respect to the ridge axis. Our results, along with geophysical and geochemical data from the 9°-10°N region of the EPR, suggest that along-axis deeps correspond with magmatic systems that have significant near-Moho (i.e., crust-mantle transition) crystallization, which we attribute to off-axis delivery of mantle melt. As this investigation is motivated by the EPR tomography results, we conclude with a numerical study that examines the travel time sensitivity of *Pn*, a sub-crustal head wave commonly used in local travel time tomography, to crustal and mantle heterogeneity. Our results indicate that *Pn* travel times and Fresnel zones are insensitive to normal sub-axial crustal thickness anomalies, mantle velocity gradients and crust-mantle velocity contrast variations and that mantle low-velocity zones must be at least 3 km thick to produce significant, near-constant *Pn* delay times. Our data support the validity and interpretation of the EPR tomography results.

This dissertation includes both previously published and unpublished co-authored material.

CURRICULUM VITAE

NAME OF AUTHOR: Douglas Troy Durant

GRADUATE AND UNDERGRADUATE SCHOOLS ATTENDED:

University of Oregon, Eugene
University of West Florida, Pensacola

DEGREES AWARDED:

Doctor of Philosophy, Geological Sciences, 2011, University of Oregon
Bachelor of Science, Physics, 2003, University of West Florida

AREAS OF SPECIAL INTEREST:

Geophysics
Seismology

PROFESSIONAL EXPERIENCE:

Teaching and Research Assistant, University of Oregon, 2003-2011

Associate Retail Manager, Zany Brainy, Inc., Fairfax, VA, 1994-1995

Scuba Diving Instructor/Consultant, The Dive Shop, Fairfax, VA, 1992-1993

Air Traffic Controller, United States Marine Corps, 1983-1992

GRANTS, AWARDS, AND HONORS:

Graduate Research Fellowship, University of Oregon, 2005-2011

Graduate School Research Award, University of Oregon, 2008

Graduate Teaching Fellowship, University of Oregon, 2003-2005

Thayer Scholarship, Dept. of Geological Sciences, University of Oregon, 2004

Physics Student of the Year, University of West Florida, 2001 & 2003

Lowell Edwards Memorial Scholarship, University of West Florida, 2001-2003

President's List, University of West Florida, 2001-2003

PUBLICATIONS:

Durant, D. T., Toomey, D. R., 2009. Evidence and implications of crustal magmatism on the flanks of the East Pacific Rise. Earth Planet. Sci. Lett. 287 (1-2), 130-136.

ACKNOWLEDGMENTS

I wish to thank Professors Douglas R. Toomey, Paul J. Wallace, Eugene Humphreys and James Isenberg for serving on my advisory committee. I also wish to express sincere appreciation to Professor Douglas R. Toomey for his generous guidance and support, as well as Professor Emilie Hooft-Toomey, Craig Thornley, Darwin Villagómez and the graduate students, faculty and staff in the Department of Geological Sciences who have provided their assistance and friendship over the past few years. This work was supported by the RIDGE and RIDGE 2000 Programs as well as NSF grants OCE-0732751, OCE-0118597, OCE-9633264 and EAR-0651123.

For my family, especially my wife, Kristi, and my daughters, Tina, Natalie, Eliana and Portia, for helping me to discover what is truly meaningful on this journey.

TABLE OF CONTENTS

Chapter Page

LIST OF FIGURES

Figure Page

LIST OF TABLES

Table Page

CHAPTER I

INTRODUCTION

Oceanic crust covers ~70% of the Earth's surface and forms as a result of tectonic plates spreading at constructional or divergent plate margins along the seafloor (i.e., mid-ocean ridges). As plates diverge, the underlying mantle adiabatically flows upward to fill the potential gap. Upon reaching the solidus, the upwelling mantle undergoes partial melting, and the resulting melt flows upward and toward the spreading center. This melt eventually crystallizes atop the trailing edges of the diverging plates to form gabbroic and basaltic oceanic crust.

Over the past several decades, models of oceanic crustal formation and its associated geophysical and geochemical processes (e.g., magmatic differentiation, volcanism, hydrothermal circulation, tectonic faulting) along fast-spreading mid-ocean ridges, like the East Pacific Rise (EPR), have been predicated on the hypothesis that the axis of mantle upwelling beneath the ridge is parallel to the spreading axis and mantle melt delivery and accumulation is rise-centered (e.g., Langmuir et al., 1986; Phipps Morgan, 1987; Macdonald et al., 1988, 1991; Buck and Su, 1989; Haymon et al., 1991; Carbotte and Macdonald, 1992; Batiza and Niu, 1992; Phipps Morgan and Chen, 1993; Scheirer and Macdonald, 1993; Perfit et al., 1994; Smith et al., 2001). Recent travel time tomography results from the UNDERSHOOT experiment (Toomey et al., 2007), however, reveal that the axis of mantle divergence and melt delivery beneath the northern

EPR between the Clipperton and Siqueiros transform faults trends obliquely to the axis of plate spreading (Fig. 1.1; modified from Toomey et al. (2007)).

Figure 1.1b shows that the flow direction of the shallow mantle, constrained by the azimuth of seismic anisotropy (green arrows), is rotated nearly 10° anticlockwise from the direction of plate spreading (Fig.1.1b, black arrows). The geometry of the imaged mantle low-velocity zone, inferred to be regions of melt accumulation beneath the base of the crust, results from the misalignment between the axes of mantle upwelling and plate spreading, indicating that mantle melt accumulation occurs both beneath the rise axis as well as off-axis. We expect that off-axis melt accumulation will affect the architecture of the overlying crust and that off-axis melt delivery will have an impact on crustal construction along the ridge axis.

In this dissertation, I present results from three separate studies, which examine the geologic consequences associated with off-axis mantle melt accumulation and its subsequent delivery to the rise axis as well as potential factors affecting the tomography results. These studies, along with their associated conclusions, are presented as follows:

1) Formation of oceanic crust along the EPR is thought to be complete within a few kilometers of the rise axis. In Chapter II, however, we present evidence for magmatism 20 km from the rise axis in crust that is over 300 ka. The crustal magma body overlies a region of off-axis delivery of mantle melt (Fig.1.1b, red star). We use a combination of seismic refraction data from the UNDERSHOOT experiment and finite

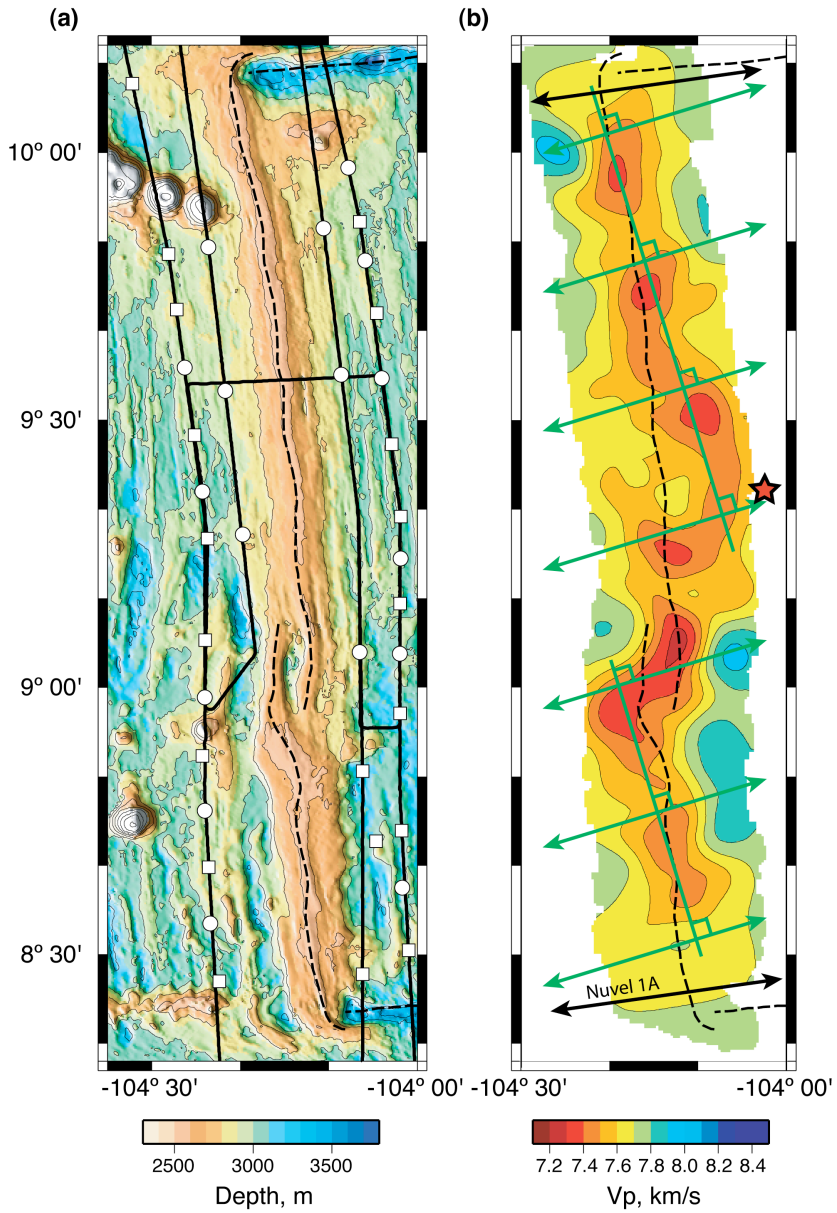

Figure 1.1. Location and geometry of the UNDERSHOOT seismic experiment and tomographic results. (a) The Clipperton and Siqueiros transform faults bound the study area. Dashed lines show the location of the plate boundary. Four-component seismometer and ocean-bottom hydrophone locations are shown by open squares and circles, respectively; shooting tracks indicated by solid black lines. (b) Tomographic image of mantle *P* wave velocity; contour interval is 0.1 km s^{-1} and depth of section is 9 km beneath the sea floor. Green lines with arrowheads indicate azimuth of seismic anisotropy; black lines with arrowheads indicate plate-spreading direction (Gripp and Gordan, 2002). Green lines without arrowheads are perpendicular to seismic anisotropy and indicate locations of en echelon segments of the mantle low-velocity zone. Red star indicates location of crustal magmatism discussed in Chapter II. Figure modified from Toomey et al. (2007).

difference waveform modeling to constrain the intrusive complex's location, size and physical properties. This chapter is co-authored by Douglas R. Toomey and is published in *Earth and Planetary Science Letters* as Durant and Toomey (2009).

2) Segment-scale axial depth variations along fast-spreading mid-ocean ridges like the EPR have traditionally been associated with magma supply and/or mantle temperature, yet geophysical observations along the northern EPR preclude these hypotheses. Recent studies show instead that increasing axial depth correlates with an increase in both crustal density (~0.1 g/cm^3) and offset of mantle upwelling with respect to the ridge axis. In Chapter III, we use thermodynamic modeling to show that systematic variations in the depth of crystallization and degree of differentiation produce crustal density variations on the order inferred along the northern EPR. This chapter is co-authored by Douglas R. Toomey and Paul J. Wallace and is currently being submitted for publication in the *Journal of Geophysical Research*.

3) Sub-crustal head waves, known as *Pn*, are commonly used in local travel time tomography for determining topmost mantle structure. In Chapter IV, we examine the sensitivity of *Pn* travel time data to marine crustal and mantle heterogeneity. We conduct numerical studies of *Pn* propagation through a 60-km-wide, cross-axis, mid-ocean ridge model and evaluate the effects of crustal and mantle low-velocity zone thickness variations, mantle velocity gradients and crust-mantle velocity contrast variations on *Pn* travel times and Fresnel zones. This chapter is co-authored by Douglas R. Toomey and is in preparation for publication.

4) In Chapter V, I summarize the conclusions and inferences from all three studies.

CHAPTER II

EVIDENCE AND IMPLICATIONS OF CRUSTAL MAGMATISM ON THE FLANKS OF THE EAST PACIFIC RISE

This chapter is co-authored by Douglas R. Toomey and is published as follows:

Durant, D. T., Toomey, D. R., 2009. Evidence and implications of crustal magmatism on the flanks of the East Pacific Rise. Earth Planet. Sci. Lett. 287, 130-136.

2.1. Introduction

Crustal accretion along the fast-spreading East Pacific Rise (EPR) occurs primarily within a narrow cross-axis window centered on the axis of plate spreading. Seafloor mapping shows that the eruptive fissures defining the neovolcanic zone occur within a kilometer-wide region centered on the axial high (Fornari et al., 1998; Haymon et al., 1991; Macdonald and Fox, 1988). Geophysical studies further reveal that directly beneath the axial high lies a narrow, steep-sided, crustal magma chamber and a seismically detectable crust-mantle transition zone or Moho (Detrick et al., 1987; Dunn et al., 2000; Kent et al., 1990). These observations have been used to infer that mantle melt is efficiently focused beneath the rise axis and that the emplacement of crust is effectively complete at zero age (e.g., Korenaga and Kelemen, 1997). Yet there is evidence that magmatic and hydrothermal activity do occur off-axis. Seafloor mapping reveals venting of hydrothermal fluids at off-axis locales (Haymon et al., 2005) and the ages of some off-axis lavas are anomalously young (Sims et al., 2003; Zou et al., 2002).

Here we present evidence of off-axis crustal magmatism from seismic refraction data (Fig. 2.1) that constrain the intrusive complex's location, size and physical properties. The seismic experiment used 28 four-component ocean-bottom seismometers (OBSs) and 29 ocean-bottom hydrophones (OBHs) to record rise parallel and perpendicular shooting lines; the source was the 20-gun, 8420 in^3 *R/V Ewing* airgun array. Previous analyses of the data constrain regional scale variations in crustal thickness (Canales et al., 2003) and the structure of a mantle-low velocity zone (MLVZ) that is skewed beneath the spreading axis (Toomey et al., 2007).

2.2. Seismic observations

The off-axis magmatic complex is defined by the following three observations (Fig. 2.1): (i) *P* waveforms that diffract around a low-velocity body in the mid-crust, (ii) an abrupt attenuation of energy that propagates through the anomalous region and (iii) a large amplitude *P*-to-*S* wave conversion that requires a solid-liquid interface. We first describe each of these waveform anomalies and then present forward modeling results to show that they are consistent with a pronounced low-velocity, high-attenuation crustal anomaly located ~2 km beneath the seafloor.

Anomalous *P* waveforms are observed in data from two instruments, one located north (OBH 16) and the other south (ORB 2) of the crustal magma body (Fig. 2.1a and b, Fig. 2.2). The record sections in Figures 2.1b and 2.2 are aligned by shot number in order to illustrate that the anomalous waveforms occur within a limited geographic region. The character of the observed waveforms is similar to that of diffracted arrivals

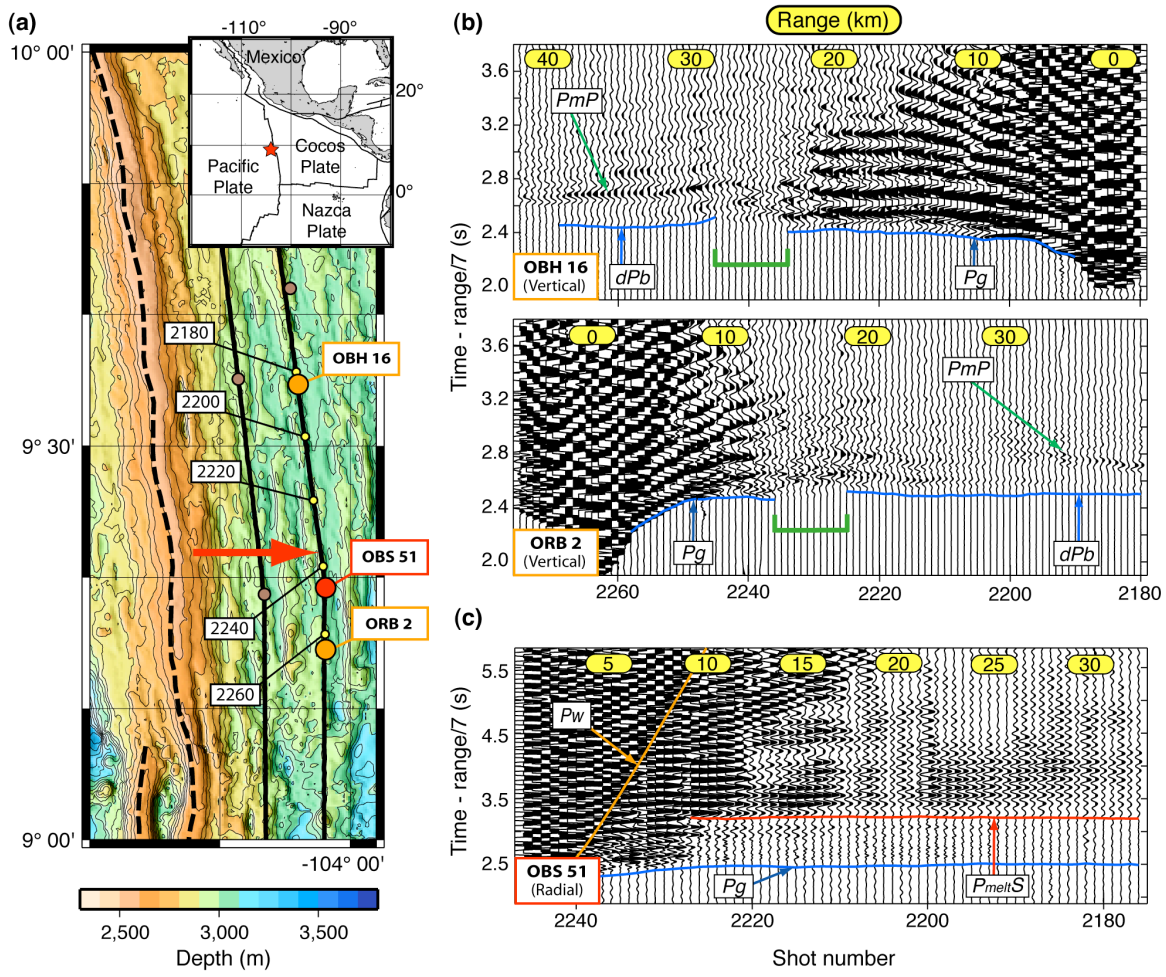

Figure 2.1. Map of experimental geometry and seismic record sections. (a) Map of the 9°20′N region of the EPR, showing locations of instruments that recorded *P* wave diffractions (orange circles) and $P_{melt}S$ arrivals (red circle), shown in record sections (b) and (c), respectively. Other instruments in the region are shown as small, brown circles. Shot locations (yellow circles) associated with record sections are labeled. The red arrow points to the center of the magmatic complex's location. Inset shows regional location of study area. (b) Record sections for hydrophones OBH 16 (top) and ORB 2 (bottom), which show diffracted *P* wave arrivals and an abrupt decrease in waveform amplitudes. Record sections are aligned by shot number (bottom axis), ranges are shown in yellow ovals (top axis); amplitudes are fixed scaled. Diffracted *P* wave arrivals are shown by green bar. (c) Radial record section for OBS 51, which shows $P_{melt}S$ (red line). *Pg* (blue line) and *Pw* (water wave; orange line) phases are also shown; amplitudes are fixed scaled. Note the large amplitude of $P_{melt}S$ arrivals out to ranges of 30 km. All record sections are plotted with a velocity reduction of 7 km s^{-1} and are band-pass filtered between 5 and 30 Hz.

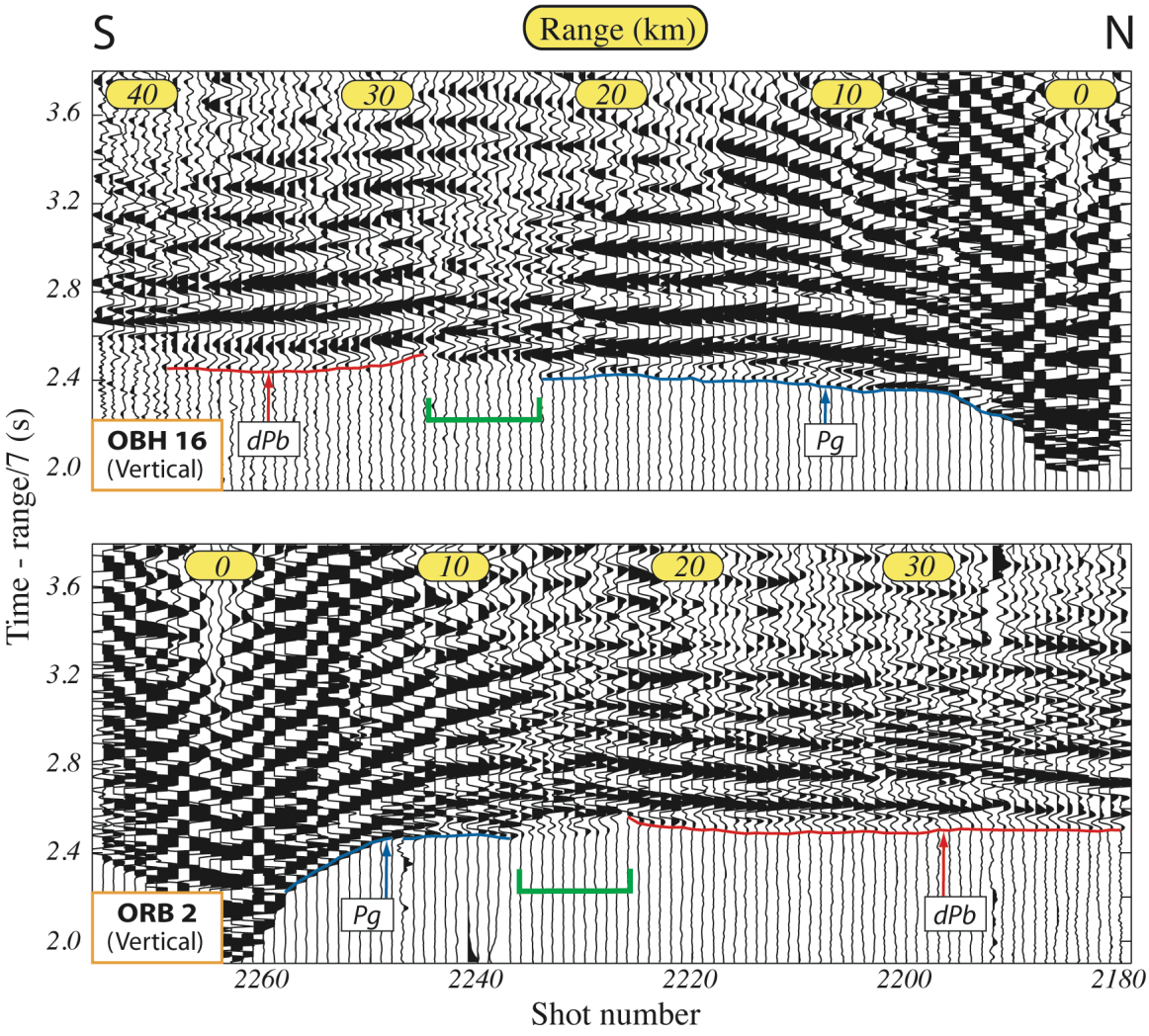

Figure 2.2. Vertical record sections showing diffracted *P* wave arrivals. Same as Figure 2.1b except data are plotted with increased amplitude and are range scaled so that *dPb* arrivals can be more easily seen (red line). A characteristic gap preceding *dPb* arrivals is observed in the data from both receivers where first arrival amplitudes are very small (green bracket). Ranges between where the gap begins and the receiving station constrain the depth of the crustal anomaly causing the *P* wave diffractions, and the gap's width constrains the length of the anomaly as noted in the main article. The record sections are plotted with a velocity reduction of 7 km s^{-1} and are band-pass filtered between 5 and 30 Hz.

predicted by waveform modeling of the axial magma chamber (Wilcock et al., 1993). Diffractions occur when a *P* wave turning in the crust encounters a pronounced low-velocity anomaly whose vertical dimension is less than the seismic wavelength, which gives rise to energy that propagates above (*dPa*) and below (*dPb*) the anomalous feature (Fig. 2.3). Figure 2.1b also shows that, at longer ranges, the first-arriving energy (*dPb*) is strongly attenuated. This energy propagates at mid-crustal depths, which indicates that the anomaly causing the *P* wave diffractions may be underlain by high attenuation crust.

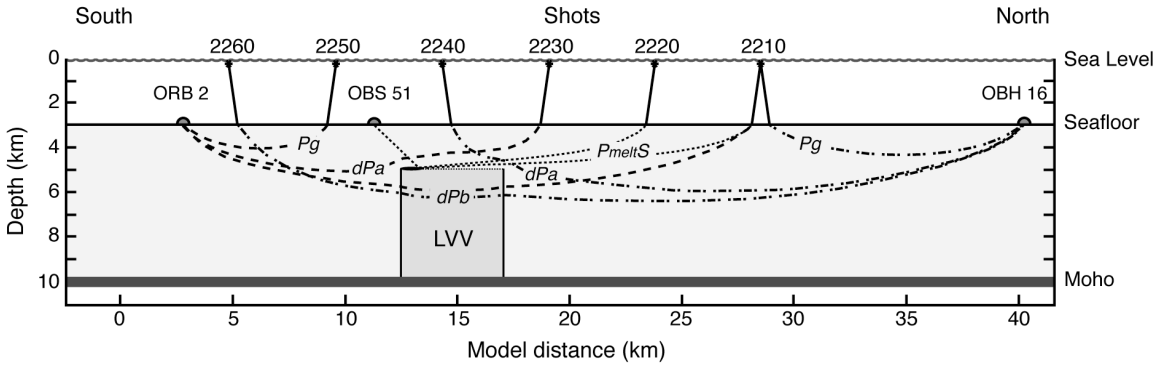

Figure 2.3. Source-receiver locations and examples of seismic ray paths. Illustration shows rise-parallel cross-sectional view of crust from south (left) to north (right). Geometry of the LVV with respect to instruments ORB 2, OBS 51 and OBH 16 is roughly to scale. Shot locations along with the region of low velocity and high attenuation below the melt sill are shown. Example ray paths for *Pg*, *dPa* and *dPb* are shown for instruments ORB 2 (dashed line) and OBH 16 (dot-dashed line); $P_{melt}S$ is shown for OBS 51 (dotted line).

The third observation that defines the crustal magma body is a large amplitude secondary arrival on the radial channel of a seismometer (OBS 51) positioned ~1 km south of the anomaly (Fig. 2.1a and c). The OBS orientation was obtained by conducting a particle motion analysis of the direct water wave on horizontal channels; data were

subsequently rotated to radial and transverse components. The polarization of the secondary arrival indicates that it is a shear wave, and the character of the phase is consistent with a *P*-to-*S* conversion at a melt lens ($P_{melt}S$) (Garmany, 1989; Singh et al., 1998). The converted phase (Fig. 2.1c, red line) arrives ~0.7 seconds after the primary phase *Pg* (Fig. 2.1c, blue line), and the high-amplitude arrivals are easily observable between 10 and 35 km range north of the receiver. A $P_{melt}S$ phase, however, is not observed south of the receiver (Fig. 2.4, bottom), constraining the reflecting interface to the northern side of OBS 51 in the same region where the *P* wave anomalies are generated.

The pronounced asymmetry observed in the OBS 51 data (Fig. 2.4, bottom) is a unique phenomenon among all of the radial data from the region. A typical radial record section from an OBS (OBS 64), located 20 km east of the rise axis and ~60 km north of OBS 51, is shown in Figure 2.4 (top) for comparison. We considered the possibility that the high-energy secondary phase observed on the north side is *Ps*, a *P*-to-*S* wave conversion at the base of the upper-most basaltic layer (layer 2A) of the crust (Christeson et al., 1997). This possibility, however, is unlikely for several reasons. In the absence of an abrupt velocity change, the difference in *Ps* arrival times between the north and south sides of OBS 51 would require an increase of 300 m in layer 2A thickness over a lateral distance of less than 1 km. The 0.7-second time difference between *Pg* and *P*-to-*S* wave arrivals on the north side would require a layer 2A thickness of ~800 m as well, which is inconsistent with previous studies of this region (Bazin et al., 2001). Moreover, the T-X curve (arrival time with respect to range) for *Ps* parallels that of *Pg*, but the T-X curve for

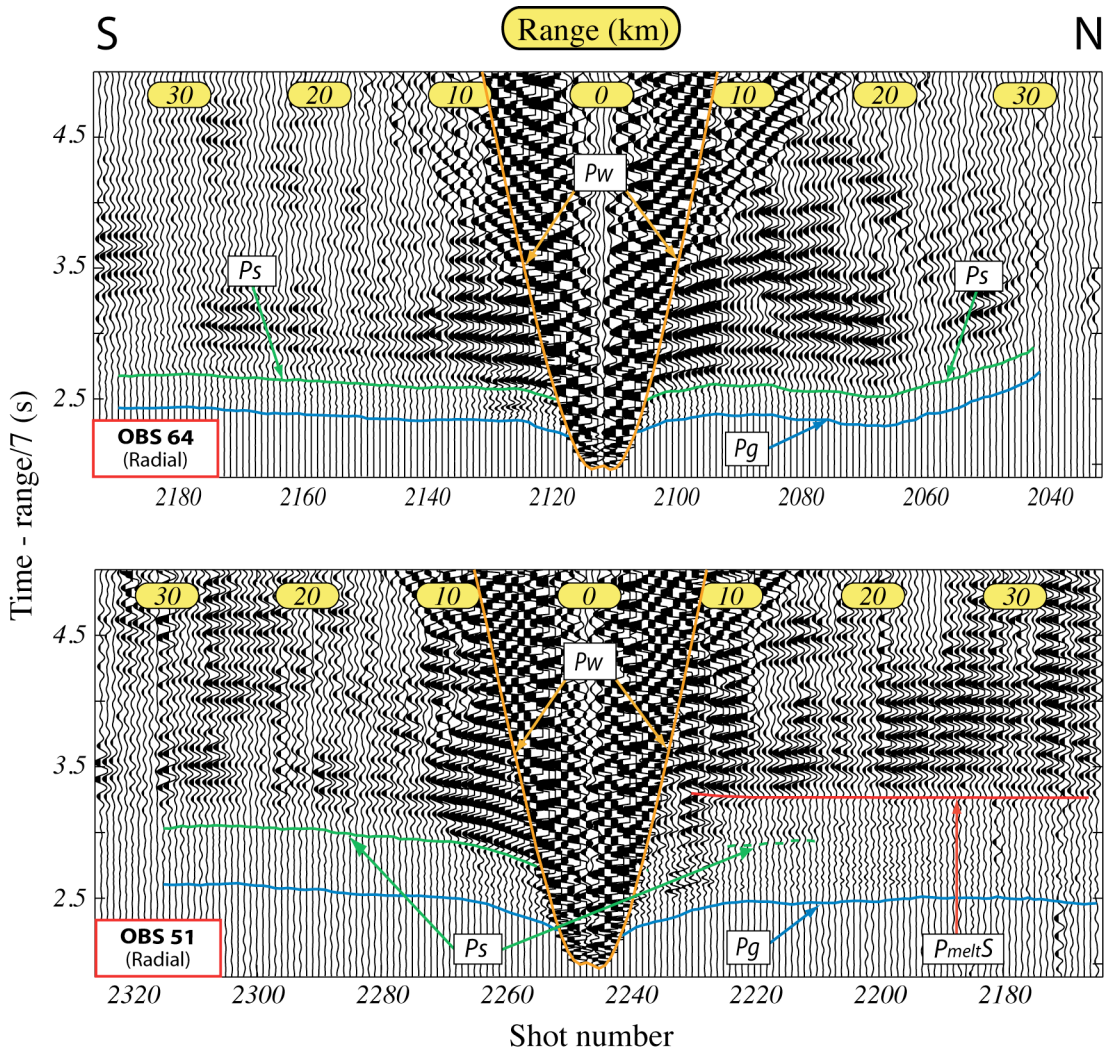

Figure 2.4. Radial record sections showing *Ps* and $P_{melt}S$ arrivals. Waveform data from OBS 51 (bottom) show $P_{melt}S$ arrivals (red line) only to the north of the receiver. *Ps* arrivals (green line) are observed south of the receiver, and some low-amplitude *Ps* arrivals can be seen north of the receiver as well (dashed green line). *Pg* (blue line) and *Pw* (water wave; orange line) phases are also shown. Data from OBS 64 (top) represent typical radial OBS data from the region. In each data set, T-X curves for *Ps* parallel those of *Pg*, whereas the T-X curve for $P_{melt}S$ diverges from *Pg* with decreasing range and is characteristic of a reflected phase. The record sections are range scaled, plotted with a velocity reduction of 7 km s^{-1} and are band-pass filtered between 5 and 30 Hz.

the high-amplitude phase on the north side of OBS 51 diverges from *Pg* at close range (Fig. 2.4, bottom). As range decreases below 10 km, the T-X curve for the high-amplitude phase monotonically increases in a hyperbolic manner, which is characteristic of a reflected phase. There is also subtle evidence of low-amplitude *Ps* arrivals observed on the north side of OBS 51 with similar arrival times as those to the south, which suggests that the crustal anomaly may be affecting the generation of *Ps* to the north of the OBS.

2.3. Seismic modeling

We use travel time (Toomey et al., 1994), and finite difference waveform (Larsen and Harris, 1993; Levander, 1988) modeling to determine the geometry and physical properties of the crustal anomaly. Two-dimensional finite difference models consist of a 50-km-long, rise-parallel cross-section that includes a 3-km-deep water layer, 7-km-thick crust, 1-km-thick Moho transition zone (MTZ) and 3-km-thick upper mantle region. Embedded in the crust is a low-velocity volume (LVV) that includes a 100-m-thick sill with low shear modulus atop a low-velocity region extending to the base of the crust (Fig. 2.5a, see Appendix A). We perform over 50 separate forward modeling experiments where we vary the length, depth and physical properties of the LVV in order to find a model whose resultant waveform anomalies are comparable to the actual data. Synthetic data from stations S1, S2 and S3 (Fig. 2.5) are selected for comparison with ORB 2, OBS 51 and OBH 16 data (Fig. 2.1), respectively. Waveform data from a model without an LVV are shown for comparison (Fig. 2.5b and c, bottom).

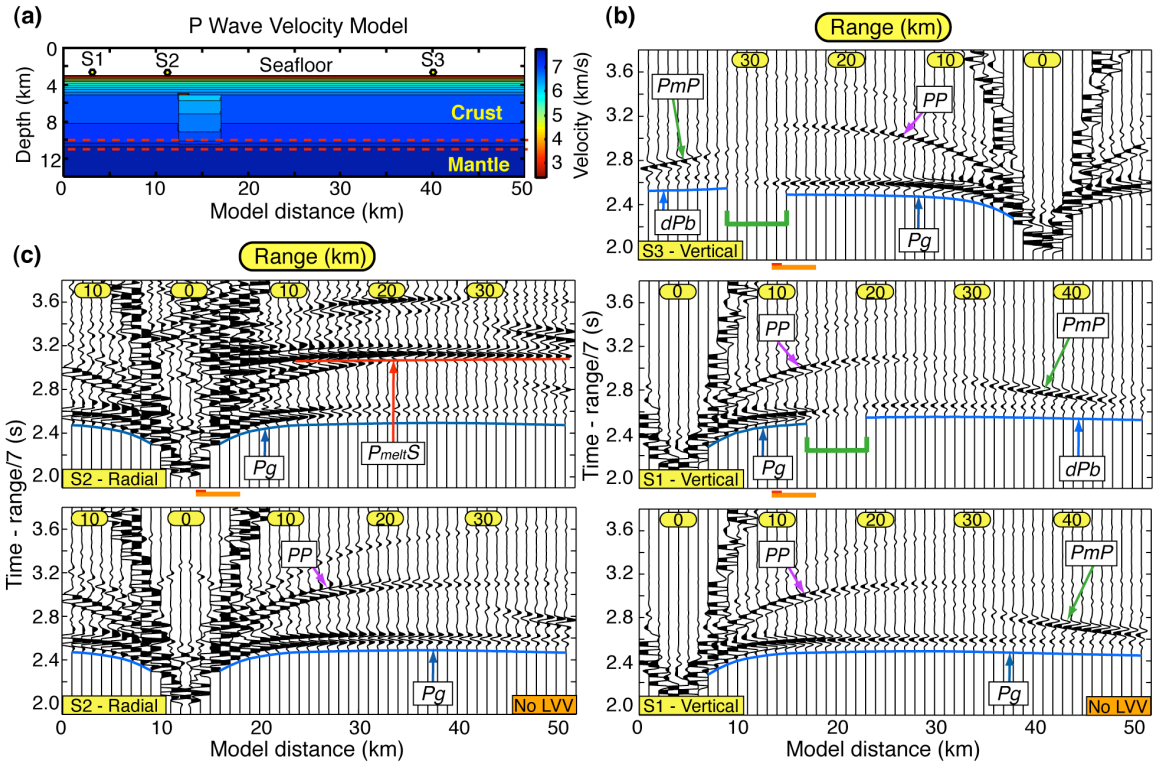

Figure 2.5. Finite difference model and synthetic record sections. (a) *P* wave velocity model with embedded LVV beginning 2 km below the seafloor. Yellow circles show synthetic station locations (S1-S3) associated with record sections shown in (b) and (c). (b) Synthetic vertical record sections for stations S1 (middle) and S3 (top) showing *P* wave diffractions and attenuated arrivals. Diffracted *P* wave arrivals are shown by green bar. A synthetic vertical record section for station S1 (bottom) from a model without an LVV is shown for comparison. *PP* and *PmP* phases are also shown in each record section. Orange bar along bottom axes of record sections indicates LVV's position in the model space; red bar shows the sill location. (c) Synthetic radial record sections for station S2 from models with (top) and without (bottom) an embedded LVV. High-amplitude $P_{melt}S$ arrivals (red line) are observed at ranges of ~5 to more than 30 km when a sill is present. All record sections are plotted with a velocity reduction of 7 km s^{-1} and are band-pass filtered between 5 and 30 Hz.

2.4. Modeling results

The observed *P* wave diffractions fix the location, length and average velocity of the LVV. Modeling results show that as the depth of the LVV increases, the range between the receiving station and the observed split in *Pg* energy increases, and waveform diffractions become more difficult to identify. No *P* wave diffractions are observed when the LVV is modeled at depths of 4 km or more. Modeling results further show that the time difference between *Pg* and *dPb* arrivals is sensitive to the velocity beneath the melt sill (i.e., the underlying LVV). Synthetic vertical record sections for S1 and S3 (Fig. 2.5b), aligned by shot number, show evidence for *P* wave diffractions similar to those observed in ORB 2 and OBH 16 data when we use a 4.5-km-long LVV that begins 2 km below the seafloor (Fig. 2.5a).

We presume in our model that the sudden decrease in waveform amplitude that is observed in ORB 2 and OBH 16 data (Fig. 2.1b) is a result of increased crustal attenuation. We estimate the degree of attenuation by comparing synthetic and observed waveform amplitudes. ORB 2 and OBH 16 data consistently show a smaller average for first-arrival amplitudes at post-anomaly ranges compared to similar ranged arrivals on the opposite side of each receiver. Waveform modeling confirms that an LVV with an attenuation anomaly in the mid- to lower-crust decreases the amplitude of both first and secondary arrivals. Synthetic data (Fig. 2.5b) are comparable to ORB 2 and OBH 16 data when the attenuating region is modeled with quality factor (Q) values between 30 and 70, which is an order of magnitude less than Q values for normal, off-axis oceanic crust at similar depths (Wilcock et al., 1992).

The high amplitude *S* wave arrival observed on the radial channel of OBS 51 constrains the physical properties of a sill located at the top of the LVV. The amplitude and observable range of *P-to-S* reflections are primarily sensitive to the shear modulus (μ) of the medium below the reflecting interface. An energy coefficient versus incident angle analysis indicates efficient *P*-to-*S* wave conversion occurs at a solid-liquid interface (Fig. 2.6). At wide angles (or large offsets), ~50% of the *P* wave's energy is reflected as an *S* wave, since no *S* wave energy is transmitted into the liquid.

Waveform modeling confirms that a finite-length sill also generates large amplitude *P*-to-*S* arrivals. Figure 2.5c (top) shows high-amplitude *P-to-S* arrivals (labeled $P_{melt}S$) on the radial channel for synthetic station S2, which is located ~1 km from a fluid-filled sill (Fig. 2.5a). We use the term "$P_{melt}S$ " to include both specular and diffracted reflections. The converted *S* wave appears at ranges of ~5 to more than 30 km; this is true for all of our models that contain a crustal melt lens, regardless of lens depth. When the lens is semi-rigid or mush-like, reflection amplitudes drop significantly. We thus attribute the large amplitude arrival observed on the radial channel of OBS 51 to a *P-to-S* conversion from a sill with zero or near-zero shear modulus. Modeling results also show that the time difference between *Pg* and $P_{melt}S$, as well as the appearance of $P_{melt}S$ at close range (< 5 km), constrain the depth to the top of the sill. As sill depth increases, so does the *Pg*-$P_{melt}S$ time difference, and $P_{melt}S$ at close range becomes more visible as its energy separates from that of the water wave. A comparable fit between S2 and OBS 51 data occurs when we model a sill at 2 km depth.

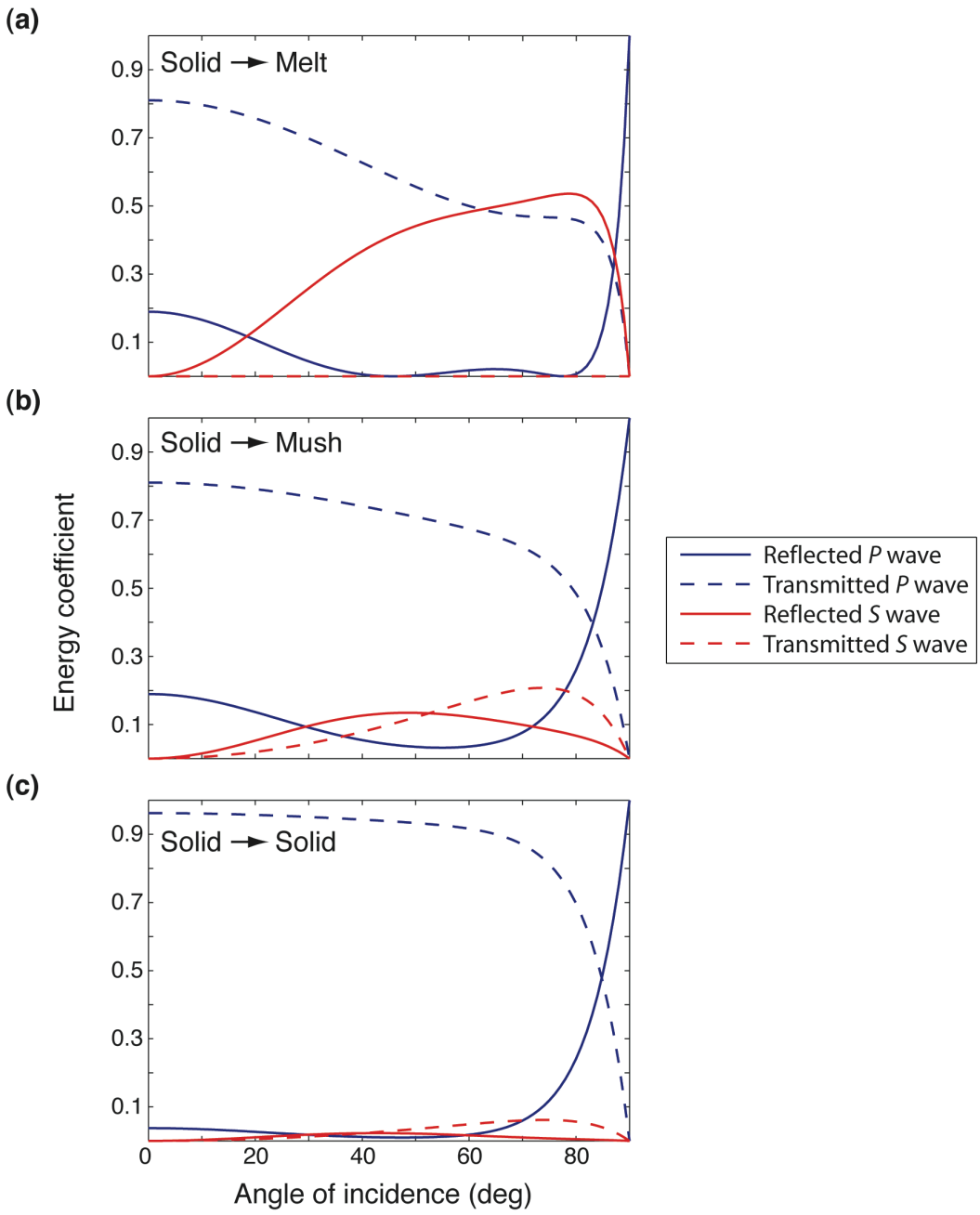

Figure 2.6. Theoretical energy coefficient calculations for a *P* wave incident upon a half-space interface. The upper layer in all three cases is solid (Vp = 6.7 km s^{-1}, Vs = 3.6 km s^{-1}, ρ = 2.96 Mg m^{-3}), (a) liquid bottom layer (Vp = 3.0 km s^{-1}, Vs = 0.0 km s^{-1}, ρ = 2.60 Mg m^{-3}); efficient conversion to reflected *S* wave energy (solid red line) at wide angles, (b) semi-rigid bottom layer (Vp = 3.0 km s^{-1}, Vs = 1.5 km s^{-1}, ρ = 2.60 Mg m^{-3}); conversion to reflected *S* wave energy drops considerably, (c) solid bottom layer (Vp = 5.0 km s^{-1}, Vs = 2.6 km s^{-1}, ρ = 2.68 Mg m^{-3}); conversion to reflected *S* wave energy is negligible.

We investigate layer 2A waveform effects, both with and without a melt sill, to determine if either *Ps* or any multiple phases (e.g., *PP* and *PPs*) appear similar to $P_{melt}S$ (Fig. 2.7). These phases are created when a velocity discontinuity between layers 2A and 2B is added to our waveform models. As noted above, $P_{melt}S$ results when a melt sill is present, and Figure 2.7 (bottom) shows that its associated T-X curve hyperbolically increases while diverging from *Pg* as range decreases (<10 km). The T-X curve for *Ps*, however, parallels that of *Pg*, and, in the melt sill model, *Ps* becomes highly attenuated at ranges beyond 10 km. These results correlate well with the OBS 51 data. When no melt sill is present, *Ps* is easily observed out to ranges beyond 30 km (Fig. 2.7, top). The T-X curvature for *P* wave (*PP*) and converted *P*-to-*S* wave (*PPs*) multiples is similar to that of *Pg* and *Ps*, which distinguishes these phases from $P_{melt}S$ as well.

2.5. Discussion

On the basis of our modeling, we conclude that a seismic velocity and attenuation anomaly located ~20 km east of the rise is the result of a crustal-level magmatic complex. The simplest structure consistent with our data is a 1-km-long (±0.5 km) melt sill located at a depth of 2 km beneath the seafloor that is underlain by a broader region (4.5-km-long, ±1 km) of crust that is anomalously hot and perhaps partially molten. The exact degree of attenuation within the LVV is difficult to resolve because of its limited spatial extent, nevertheless our *Q* estimates do indicate an order of magnitude increase in attenuation compared to normal, off-axis crustal values. We note that the LVV was not detected in a previous two-dimensional tomographic study of the region (Canales et al., 2003). The limited spatial extent of the LVV allows for rapid, post-anomaly wavefront

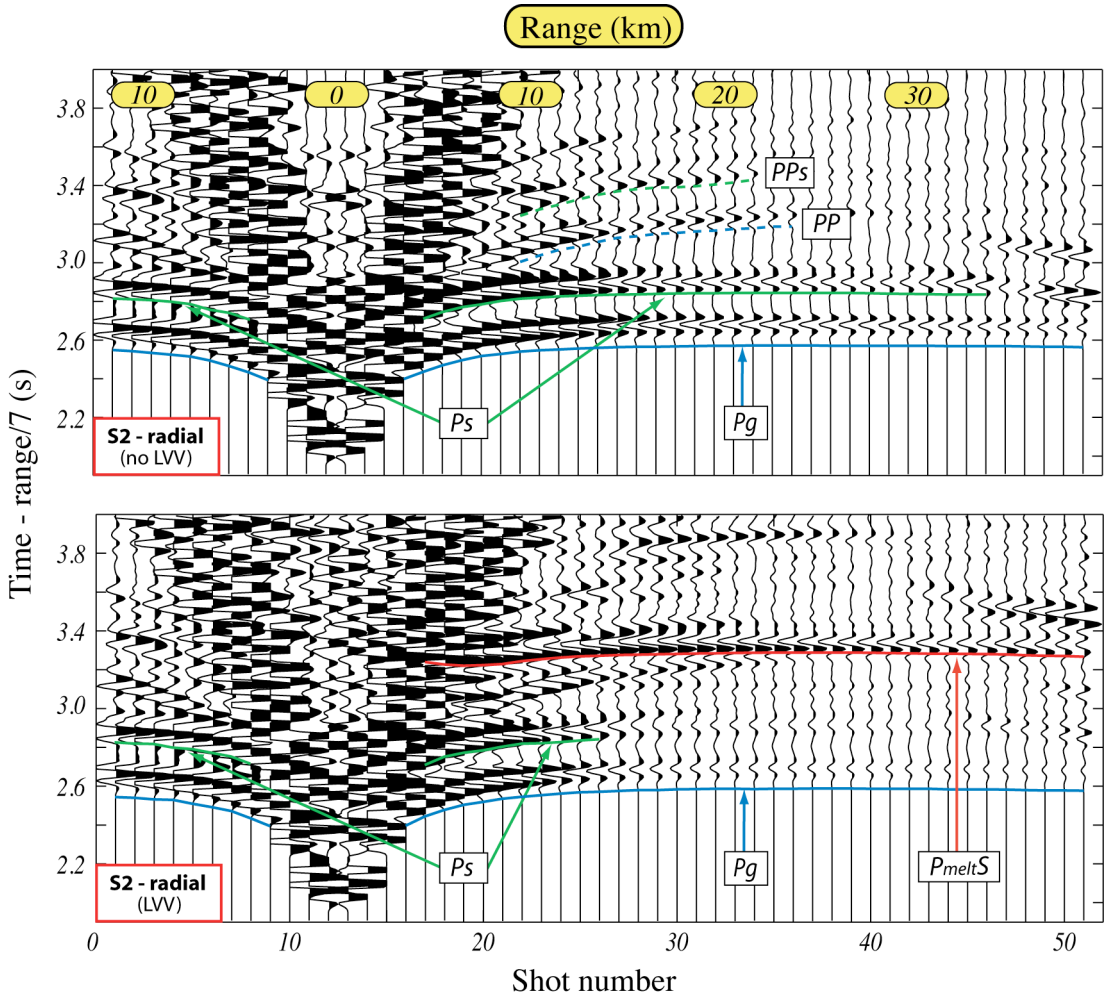

Figure 2.7. Synthetic radial record sections showing layer 2A effects. Synthetic radial waveform data for station S2 with (bottom) and without (top) a melt sill. These models include a layer 2A-2B velocity discontinuity in order to determine its waveform effects. Note that when a melt sill is present (bottom), $P_{melt}S$ is generated (red line), and *Ps* (green line) becomes highly attenuated at ranges beyond 10 km. When no melt sill is present (top) *Ps* is easily observed out to ranges beyond 30 km. In each data set, T-X curves for *Ps* parallel those of *Pg* (blue line). T-X curvature for multiple and converted multiple phases [*PP* (top, dashed blue line) and *PPs* (top, dashed green line), respectively] resembles that of *Pg* and *Ps*. The T-X curve for $P_{melt}S$, however, diverges from *Pg* with decreasing range and is characteristic of a reflected phase. Both record sections are plotted with a velocity reduction of 7 km s^{-1} and are band-pass filtered between 5 and 30 Hz.

healing, which results in a travel-time effect for first arrivals that is not large (<50 ms) and that is limited to a small number of shots. This makes the anomaly difficult to resolve by delay-time tomographic methods. Our results indicate that waveform data can better reveal crustal magma bodies such as the one we have found, particularly when compared to a two-dimensional tomographic study.

The high-attenuation LVV we detect is consistent with the injection of a significant amount of heat into the ridge flank. If the cross-axis width of the anomaly is only 1 km, we conservatively estimate ~1 x 10^{19} J of anomalous heat has been supplied to the crust compared to average off-axis mid- to lower-crustal reference temperatures between 400 and 800 °C (see Appendix B). The latent heat of crystallization associated with a single melt sill like the one in our model accounts for less than 2% of the estimated heat. We thus conclude that the high-attenuation LVV marks a site of repeated intrusive activity.

We attribute the occurrence of repeated, off-axis magmatic activity to a long-lived skew between the axes of mantle upwelling and plate spreading (Toomey et al., 2007; Toomey and Hooft, 2008) (Fig. 2.8). As a consequence of this skew the MLVZ – which defines the pattern of magma delivery from the mantle to the crust – is offset to the east of the rise, roughly underlying the high-attenuation, crustal-level LVV. Analyses of bathymetry, seismic crustal thickness and gravity data indicate that a skewed pattern of mantle upwelling has persisted in this region for at least 1 Ma (Toomey and Hooft, 2008).

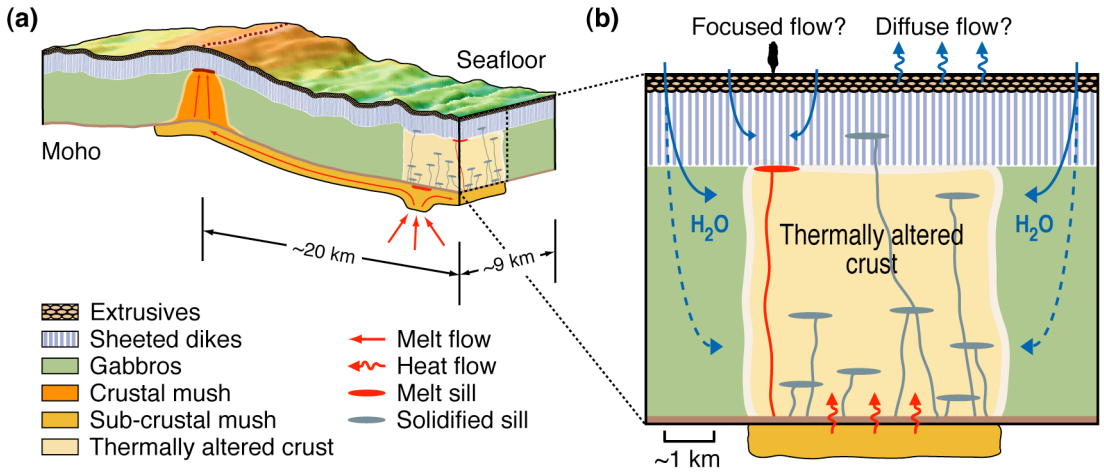

Figure 2.8. Crustal alteration due to the off-axis delivery of mantle melt. (a) Perspective view of study area (right side) with respect to the ridge axis (dotted red line); bathymetry is exaggerated. Diagram shows an area of thermally altered crust (tan region) associated with the off-axis delivery of mantle melt. Melt migration (solid red arrows) toward the rise axis likely occurs at sub-Moho depths within a mushy layer (orange region). (b) Close-up of the rise-parallel crustal face associated with the results of our study. Diagram shows a region of crust that has been thermally altered due to the release of heat from crystallizing sub-crustal melt (wavy red arrows) as well as solidifying crustal intrusions (gray ellipses). Blue arrows illustrate possible upper-crustal (solid) and deep-crustal (dashed) penetration of seawater. High-temperature vents (black cloud) may be generated by focused hydrothermal flow near shallow magma bodies like the one we detect (red ellipse), but diffuse flow venting (wavy blue arrows) likely dominates the thermally altered region.

In addition, where we have imaged a crustal magmatic intrusion, both the MTZ (Vera et al., 1990) and the crust (Canales et al., 2003) are anomalously thick and the average crustal density is elevated (Canales et al., 2003, Toomey and Hooft, 2008). We thus infer that the off-axis delivery of mantle melt gives rise to magmatic underplating and intrusive activity that thickens both the MTZ and the crust, thereby fundamentally altering crustal architecture (Fig. 2.8). Our discovery of off-axis magmatic activity may thus explain the large number of crosscutting dikes, sills and intrusions of ultra-mafic and mafic

composition in the crust as observed in the Oman ophiolite complex (Juteau et al., 1988; Nicolas et al., 1996). In regions of the ophiolite complex where there is a thick Moho, wehrlitic intrusions are found in every level of the crustal section, and it is estimated that they can make up as much as 20 to 40% of the total volume of the crustal plutonic sequence (Juteau et al., 1988).

Repeated intrusive activity may act as a source for off-axis lava flows and drive off-axis hydrothermal circulation (Fig. 2.8). Although there are no currently known bathymetric or morphologic features that indicate extrusive volcanism immediately above the magma body we image, anomalously young lavas have been found nearby (Zou et al., 2002). Off-axis hydrothermal activity is likely dominated by diffuse flow venting, although focused, high-temperature vents (i.e., black smokers) near shallow-crustal magma bodies could be present. Deep crustal penetration of seawater through fractures and microcracks (Nicolas and Mainprice, 2005) also provides a mechanism for driving off-axis wehrlite formation (Feig et al., 2006). Hydrothermal venting, whether focused or diffuse, would produce a chemically life-sustainable environment for biological communities to thrive at off-axis locales. Our results provide compelling motivation for expanding the search for seafloor hydrothermal activity and its associated ecosystems beyond the axis of seafloor spreading.

In this chapter, I have addressed the impact of off-axis mantle melt accumulation on the architecture of the overlying crust. In the next chapter, I examine effects on crustal construction associated with the off-axis delivery of mantle melt to the ridge axis.

CHAPTER III

THE EFFECTS OF CRYSTALLIZATION DEPTH AND RESIDENCE TIME ON CRUSTAL DENSITY AT FAST-SPREADING RIDGES

This chapter is co-authored by Douglas R. Toomey and Paul J. Wallace. I conducted the thermodynamic modeling and analysis and wrote the chapter. Douglas R. Toomey and Paul J. Wallace provided essential guidance with the research and edits to the chapter. This chapter is currently being submitted for publication in the *Journal of Geophysical Research*.

3.1. Introduction

Since the ground-breaking work of Klein and Langmuir (1987), it has long been held that axial depth and crustal thickness variations along mid-ocean ridges (MORs) are primarily related to variations in melt supply from the mantle, with axial highs and thicker crust being associated with more melt. This idea works well for slow-spreading ridges (<40 mm/a, full rate), where very large along-axis variations in axial depth, crustal thickness and gravity anomalies (e.g., Lin et al., 1990; Tolstoy et al., 1993; Detrick et al., 1995; Hooft et al., 2000) suggest pronounced spatial and temporal variability in mantle melting and/or magma transport. Fast-spreading ridges (>80 mm/a, full rate), however, have much more subtle and apparently inconsistent along-axis crustal thickness and gravity variations (e.g., Madsen et al., 1990; Barth and Mutter, 1996; Wang et al., 1996; Canales et al., 2003; Toomey and Hooft, 2008), which suggests axial depth is not related to melt supply. What then explains axial depth variations at fast-spreading ridges?

The 9°-10°N segment of the fast-spreading East Pacific Rise (EPR) (~111 mm/a, full rate) (Carbotte and Macdonald, 1992), defined by the Clipperton transform fault to the north and a large overlapping spreading center (OSC) to the south (Fig. 3.1), has been the target of numerous studies over the past few decades (a Ridge 2000 Integrated Study Site). These studies provide complementary data sets that constrain axial depth, crustal thickness, gravity anomalies, basalt chemistry and the distribution of mantle melt (e.g., Tighe et al., 1988; Batiza and Niu, 1992; Wang et al., 1996; Canales et al., 2003; Toomey et al., 2007), making this an ideal location for investigating the axial depth enigma.

Axial depth variation observed along this segment of the EPR (Tighe et al., 1988; Carbotte et al., 2004) has traditionally been explained using the magma supply hypothesis (Macdonald et al., 1988, 1991). In this view, the intrasegment axial high (~9°50′N) results from increased melt supply, so the axial high should either be underlain by thicker crust or there should be along-axis redistribution of magma. Geophysical and geochemical studies (e.g., Langmuir et al., 1986; Kent et al., 1993; Toomey et al., 1990; Dunn et al., 2000; Canales et al., 2003; Toomey et al., 2007), however, preclude either of these scenarios. Moreover, seismic studies (Barth and Mutter, 1996; Canales et al., 2003) show a systematic increase in crustal thickness from the axial high at 9°50′N toward the axial low near the 9°03′N OSC, and gravity studies (Madsen et al., 1990; Wang et al., 1996) paradoxically show that axial gravity increases with crustal thickness.

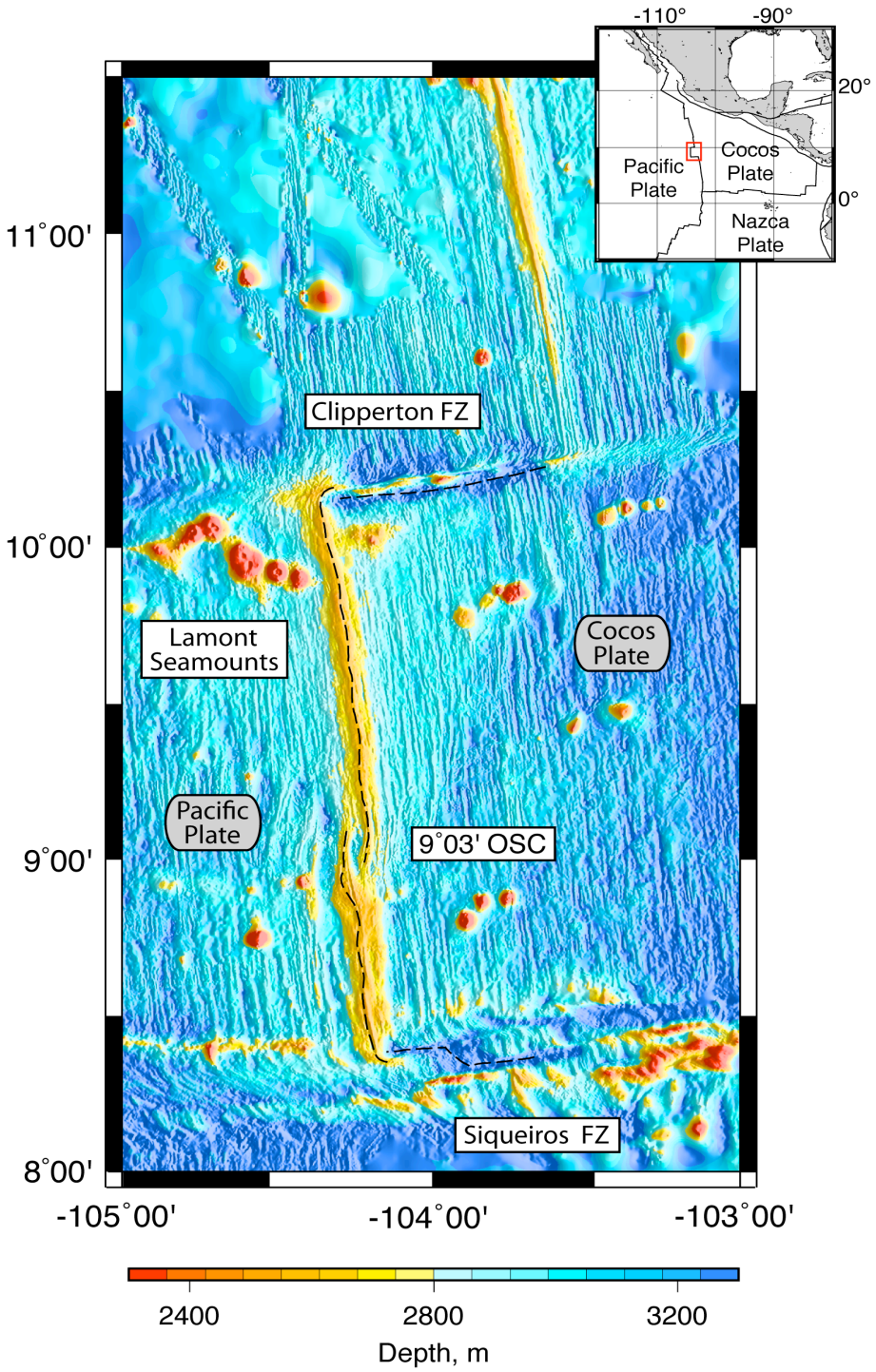

Figure 3.1. Map of the northern East Pacific Rise. Bathymetric map showing changes in axial depth and seafloor morphology between 8°00′N and 11°30′N along the northern East Pacific Rise. Geophysical and geochemical data referenced in this study are collected between the Clipperton transform fault or fracture zone (FZ) and the 9°03′N overlapping spreading center (OSC). Inset shows regional location of study area.

A recent alternative hypothesis, however, links segment-scale axial depth variation at fast-spreading MORs with variations in crustal density (Toomey and Hooft, 2008). Results from a synthesis of geophysical and geochemical data show that increasing axial depth along the northern EPR correlates with an increase in crustal density, magmatic differentiation and offset of mantle upwelling with respect to the ridge axis, and that the observed increase in axial depth can be accounted for by a 0.1 g/cm^3 increase in bulk crustal density (Toomey and Hooft, 2008). In this view, crustal density increases with greater amounts of magmatic differentiation, which is associated with off-axis melt supply. We refer to this hypothesis as the magma differentiation hypothesis.

Here we demonstrate the viability of the magma differentiation hypothesis by using thermodynamic modeling to show that systematic variations in the depth of crystallization, as well as the degree of differentiation, produce crustal density variations on the order inferred from the geophysical and petrologic data collected along the northern EPR. We confine our study to density variation in the mid- and lower crust, since upper-crustal density is highly influenced by the porosity of the extrusive layer (e.g., Carlson and Herrick, 1990). For simplicity, we refer to both the mid- and lower crust as lower crust, meaning everything at or below axial magma chamber (AMC) depth (typically comprising ~70% of the crust).

3.2. Thermodynamic modeling

For our thermodynamic modeling we chose MELTS (Ghiorso and Sack, 1995; Asimow and Ghiorso, 1998), a software package designed for modeling magmatic phase

relations at low pressures (<20 kbar). MELTS is best calibrated for mafic systems (see http://melts.ofm-research.org) and is well suited for the fast-spreading MOR environment. To evaluate the feasibility of our models, we compared the liquid line of descent (LLD) from each model with major element data obtained from glass samples collected along the northern EPR between 9° and 10°N. The glass data consist of over 900 samples (Allan et al., 1989; Batiza and Niu, 1992; Perfit et al., 1994; Batiza et al., 1995, 1996; Langmuir, 1999; Danyushevsky et al., 2000; Perfit, 2000; Melson and O'Hearn, 2003) collected within 5 km of the ridge axis and were obtained from the PetDB database (Lehnert et al., 2000; www.petdb.org). We also filtered the glass data to samples collected within 1 km of the ridge axis (see Section 3.4) but found no significant differences in major element data trends. Samples with very low MgO values (<5 weight percent (wt%)) collected near the 9°03′ overlapping spreading center (OSC) were removed to avoid samples that have undergone extensive fractional crystallization and that may have been formed by processes related to the complexity of the OSC itself (e.g., Combier et al., 2008; White et al., 2009).

We computed ~170 models in order to optimize modeling parameters and evaluate effects of melt composition, H_2O content and crystallization depth on cumulate density. In each case, thermodynamic calculations were made for the geochemical system at 1°C increments from the liquidus until crystallization was more than 90% complete. We compared equilibrium and fractional crystallization methods but chose fractional crystallization for our modeling because it most closely simulates what occurs in the MOR environment (e.g., Langmuir, 1989). Although the type of crystallization

may affect the LLD for a particular starting composition, our modeling results indicate it has little effect on cumulate density. We found that our melt compositions best matched the EPR data when we used an oxygen fugacity that was slightly reduced (f_{O2} = QFM-1). This is slightly more reduced than the average value for global MORB glasses of 0.4 ± 0.4 log units below QFM reported by Bezos and Humler (2005).

We used four different parental melt compositions to evaluate compositional effects on cumulate density, which include: (1) a primitive mid-ocean ridge basalt (MORB) composition (Ghiorso, 1997) that is representative of EPR glass samples from the Lamont seamount chain (Allan et al., 1989); (2) the previous MORB composition back-corrected for olivine fractionation to a melt in equilibrium with mantle olivine (constructed by adding 5.2% equilibrium olivine in 0.1% increments so that the final composition is in equilibrium with Fo_{91} olivine); (3) an average composition of primitive, high-Mg glass from the Siqueiros Transform zone (Perfit et al., 1996) and (4) the previous Siqueiros composition that has undergone a small amount (3%) of upper mantle crystallization (see Section 3.3.1). For simplicity, we refer to these compositions as C1-C4, respectively. A small amount of Cr (~300-500 ppm) was included in each composition to allow for correct Cr-spinel crystallization, and 0.2 wt% H_2O was included in compositions C3 and C4 (based on the values of H_2O that have been found in MORB glasses (e.g., Danyushevsky et al., 2000; le Roux et al., 2006), since we found that no anhydrous composition produces an LLD that fits the EPR geochemical data trends well (see Section 3.3.2). All compositions are listed in Table 3.1.

Table 3.1. Major element data (by weight %) for normalized melt compositions used in thermodynamic models.

	Parental melt composition variation				Initial H_2O content variation (weight % H_2O)					Moho crystallization (% crystallization)					Upper mantle crystallization (% crystallization)				
	C1	C2	C3	C4	0.0	0.1	0.2	0.3	0.4	10	20	30	40	50	10	20	30	40	50
SiO_2	48.50	48.09	48.98	49.19	49.29	49.24	49.19	49.14	49.10	49.55	49.75	49.83	49.92	50.00	49.28	49.32	49.36	49.36	49.11
TiO_2	1.01	0.96	0.95	0.97	0.98	0.97	0.97	0.97	0.97	1.08	1.22	1.36	1.55	1.83	1.09	1.19	1.35	1.54	1.82
Al_2O_3	17.58	16.70	17.35	17.57	17.60	17.59	17.57	17.55	17.53	16.77	16.31	16.10	15.82	15.42	17.37	17.23	17.01	16.77	16.40
Fe_2O_3	0.89	1.32	0.00	0.88	0.88	0.88	0.88	0.88	0.88	0.96	1.02	1.09	1.17	1.28	0.93	0.98	1.05	1.13	1.23
Cr_2O_3	0.04	0.07	0.07	0.04	0.04	0.04	0.04	0.04	0.04	0.05	0.06	0.06	0.06	0.06	0.05	0.05	0.05	0.05	0.05
FeO	7.56	7.22	7.90	7.04	7.05	7.04	7.04	7.03	7.02	7.45	7.98	8.55	9.33	10.35	7.52	7.95	8.61	9.33	10.28
MnO	0.00	0.00	0.12	0.12	0.12	0.12	0.12	0.12	0.12	0.13	0.14	0.15	0.17	0.20	0.13	0.14	0.16	0.18	0.22
MgO	9.07	11.05	9.91	9.17	9.19	9.18	9.17	9.17	9.16	8.89	8.49	8.07	7.52	6.81	8.82	8.51	8.04	7.56	6.94
CaO	12.41	11.78	12.04	12.26	12.29	12.27	12.26	12.25	12.24	12.27	11.98	11.50	10.87	10.09	11.88	11.53	10.99	10.45	9.93
Na_2O	2.64	2.51	2.42	2.47	2.48	2.48	2.47	2.47	2.47	2.56	2.71	2.89	3.12	3.41	2.63	2.76	2.97	3.19	3.48
K_2O	0.03	0.03	0.01	0.01	0.01	0.01	0.01	0.01	0.01	0.01	0.01	0.01	0.02	0.02	0.01	0.01	0.01	0.02	0.02
P_2O_5	0.08	0.08	0.06	0.06	0.06	0.06	0.06	0.06	0.06	0.07	0.08	0.09	0.10	0.12	0.07	0.08	0.09	0.10	0.12
H_2O	0.20	0.20	0.20	0.21	0.00	0.10	0.21	0.30	0.40	0.23	0.26	0.29	0.34	0.41	0.23	0.26	0.30	0.34	0.41
Total	100.00	100.00	100.00	100.00	100.00	100.00	100.00	100.00	100.00	100.00	100.00	100.00	100.00	100.00	100.00	100.00	100.00	100.00	100.00

We used composition C4 in our modeling to determine the effects of H_2O content and depth of crystallization on cumulate density, because C4 is a primitive EPR composition and its calculated LLDs match the overall EPR data well (see Section 3.3.1). For determining H_2O content effects, we varied the wt% of H_2O in C4 from 0.0 (anhydrous) to 0.4 (Table 1). We continued to use C4 with 0.2 wt% H_2O for evaluating depth (pressure) effects on cumulate density as this composition and H_2O content best fit the EPR data (see Section 3.3.2). To constrain pressure of crystallization analyses, we simulated AMC crystallization by using a pressure of 0.5 kbar (~1.5 km), crust-mantle transition zone or Moho crystallization using 2.0 kbar (~6 km) and upper mantle crystallization using 3.0 kbar (~9 km).

Model sequences used to evaluate pressure effects on cumulate density during crystallization were set up to represent different methods of lower crustal formation. We used a single-stage model to represent a "gabbro-glacier" system (e.g., Nicolas et al., 1988; Henstock et al., 1993; Phipps Morgan and Chen, 1993; Quick and Denlinger, 1993), where crystallization solely occurs in the AMC, and the lower crust forms by gravitational settling and subsidence of cumulates (Fig. 3.2a). A two-stage model was used to represent lower crustal formation by a combination of Moho and AMC crystallization (e.g., Schouten and Denham, 1995) (Fig. 3.2b). We did this by using melt compositions extracted after 10-50% crystallization (in 10% increments) at Moho depth and placing them at AMC depth for additional crystallization. We also used this two-stage method to investigate the effects of initial upper mantle crystallization on cumulate densities. Here, however, we calculated cumulate densities resulting from additional

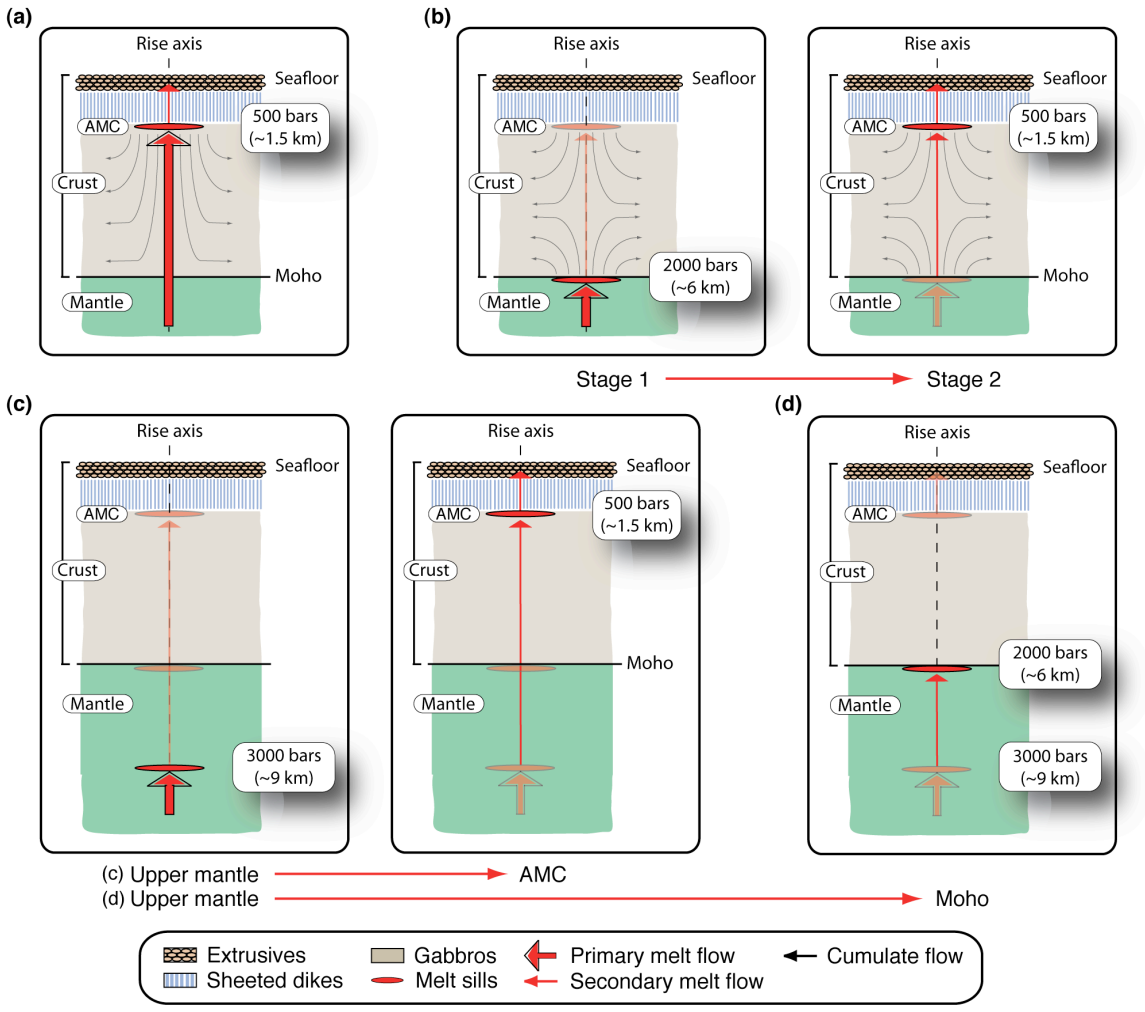

Figure 3.2. Depth of crystallization models. (a) Single-stage crustal construction model associated with a "gabbro-glacier" system (e.g., Nicolas et al., 1988; Henstock et al., 1993; Phipps Morgan and Chen, 1993; Quick and Denlinger, 1993), where crystallization solely occurs in the axial magma chamber (AMC), and the lower crust forms by gravitational settling and subsidence of cumulates. (b) Two-stage crustal construction model representing lower crustal formation by a combination of crust-mantle transition (Moho) and AMC crystallization (e.g., Schouten and Denham, 1995). Melt compositions are extracted at 10-50% Moho crystallization stages in 10% increments and are placed at AMC depth for additional crystallization. (c) Upper mantle to AMC crystallization. Same method as (b), but extracted melt compositions come from upper mantle crystallization. (d) Upper mantle to Moho crystallization. Melt compositions are extracted from up to 23% upper mantle crystallization and are placed at Moho depth for additional crystallization.

(second-stage) crystallization at both AMC and Moho depths (Fig. 3.2c and 3.2d, respectively).

3.3. Modeling results

In the following subsections, we show our thermodynamic modeling results for the effects of melt composition, H_2O content and crystallization depth on cumulate density. Density data are plotted for cumulates and residual melt with crystallization markers placed along the data curves (Fig. 3.3). The markers identify progressive stages of crystallization in 10% increments from the beginning of cumulate precipitation until MgO wt% decreases to a value of 5.5, which is below the lower limit of the referenced EPR geochemical data (see Fig. 3.4). At each calculated increment, cumulate density values reflect total cumulate density, which is the weighted sum of all current and previously fractionated phases.

3.3.1. Melt composition

The calculated LLD for compositions C1-C4 crystallizing at AMC depth (0.5 kbar) is plotted with EPR glass data (Fig. 3.4). Data from all four models fit general trends for TiO_2, Al_2O_3 and FeO_T well and fit CaO data in the earlier stages of crystallization (>7.5 wt% MgO). Later stages of crystallization (<7.5 wt% MgO) along each LLD bound the lower values of the CaO data. Some of the higher CaO data in this range may partially be explained by small amounts of prior crystallization in the upper mantle (see Section 3.3.3.2), and remaining data may result from compositional variations in parental melts and/or magma mixing (e.g., Pan and Batiza, 2003). Abrupt

changes in model data trends for Al_2O_3 and CaO occur when clinopyroxene begins to precipitate (see below). Compositions C3 and C4 match FeO_T data the best whereas compositions C1 and C2 trend on the higher side of the glass data. Each of our models spans the full range of compositional evolution along the EPR (5.8-9.1 wt% MgO).

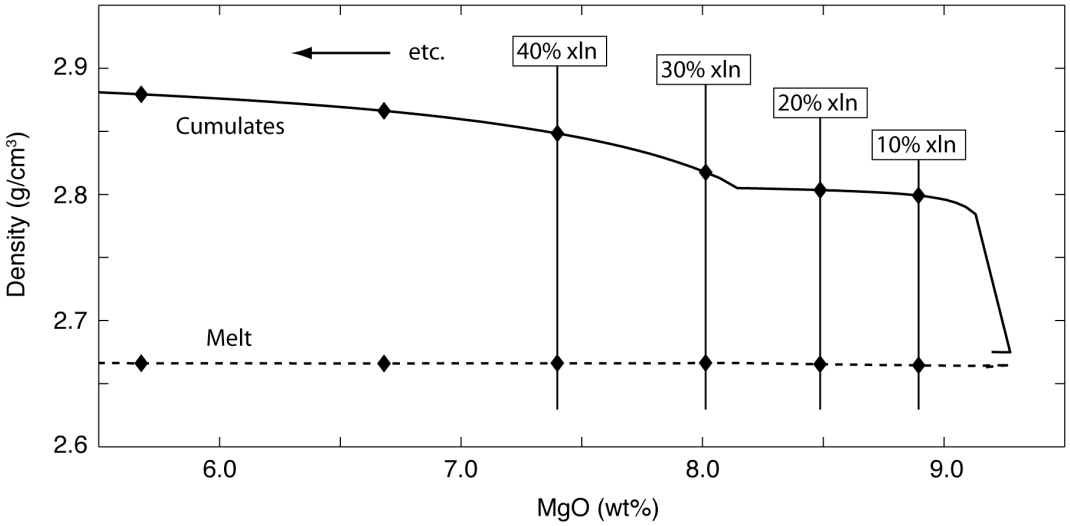

Figure 3.3. Density calculations for the single-stage crustal construction model. Cumulate (solid line) and melt (dashed line) densities from thermodynamic modeling of AMC crystallization (single-stage crustal construction model, Fig. 3.2a) using melt composition C4. Diamond markers along density curves indicate progressive degrees of crystallization in 10% increments until reaching 5.5 wt% MgO, which is the lower limit of the referenced EPR glass data (see Fig. 3.4). These density curves are used for model comparisons in Figures 3.10 and 3.14; they are presented as dashed lines.

Resultant cumulate and residual melt density data for each of our models are shown in Figure 3.5 (solid and dashed lines, respectively). A significant amount of variation in cumulate density occurs during the early stages of crystallization (>8 wt% MgO), but density values converge as crystallization progresses. The cause for the initial

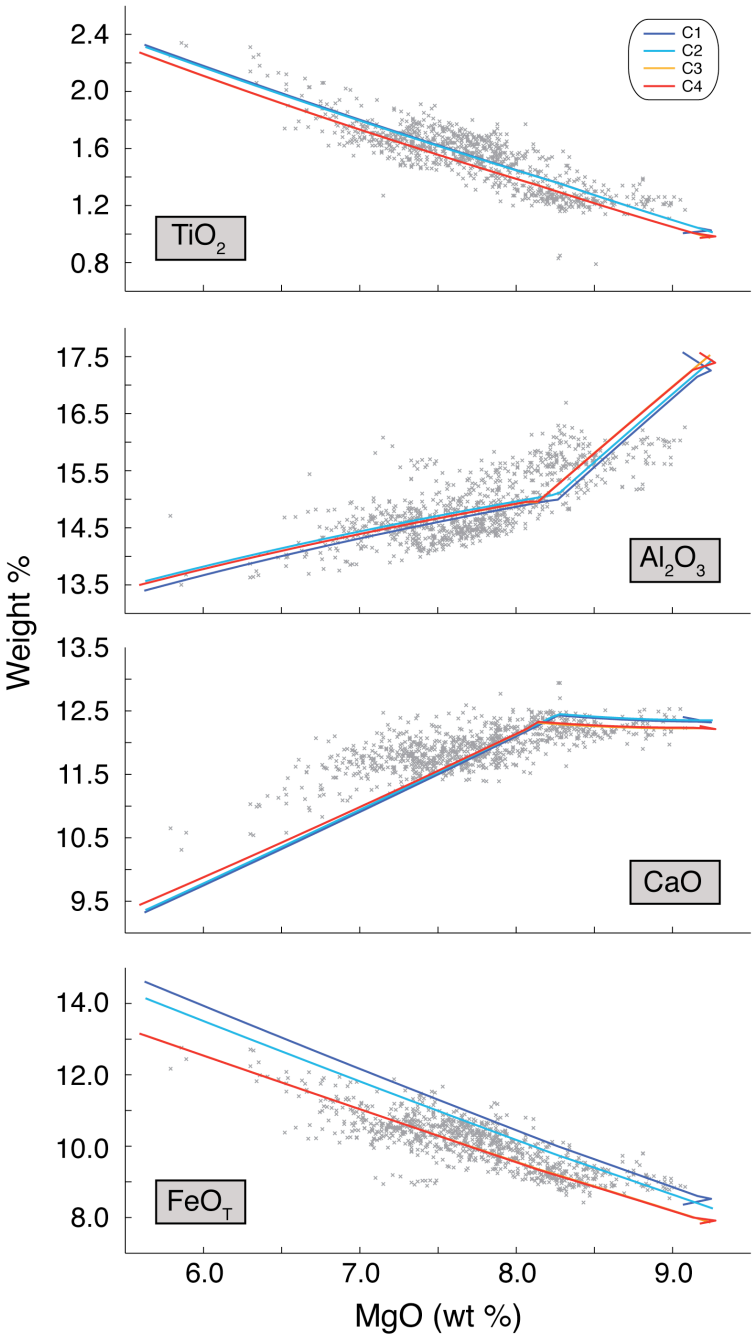

Figure 3.4. Calculated liquid lines of descent for composition variation models. Liquid lines of descent for melt compositions C1-C4, calculated using MELTS (Ghiorso and Sack, 1995; Asimow and Ghiorso, 1998) at 0.5 kbar (AMC depth). Calculations are made assuming fractional crystallization with f_{O2} = QFM-1. Major element data are for glass samples collected from the 9°-10°N region of the EPR (see Section 3.2 for references) and are obtained from the PetDB database (Lehnert et al., 2000; www.petdb.org).

density variation is due to the first mineral phases precipitating in each case (Fig. 3.6). In all cases, plagioclase and olivine precipitate very early in the crystallization sequence (<5% crystallization). With the more primitive compositions (C2 and C3), however, olivine precipitates first, which significantly increases initial cumulate density values. Models C2 and C3 also have a small amount (<5 wt%) of spinel precipitate early, which increases initial cumulate density values even more. As clinopyroxene joins the cumulate assemblage (~8 wt% MgO), density values converge for all four models. There is negligible variation in residual melt density in each of the models throughout the crystallization sequence. Crystallization markers (Fig. 3.5, colored diamonds) along the density lines show variations in % crystallization for the different parental compositions used in the models and reflect variations in mineral-in temperatures for each composition.

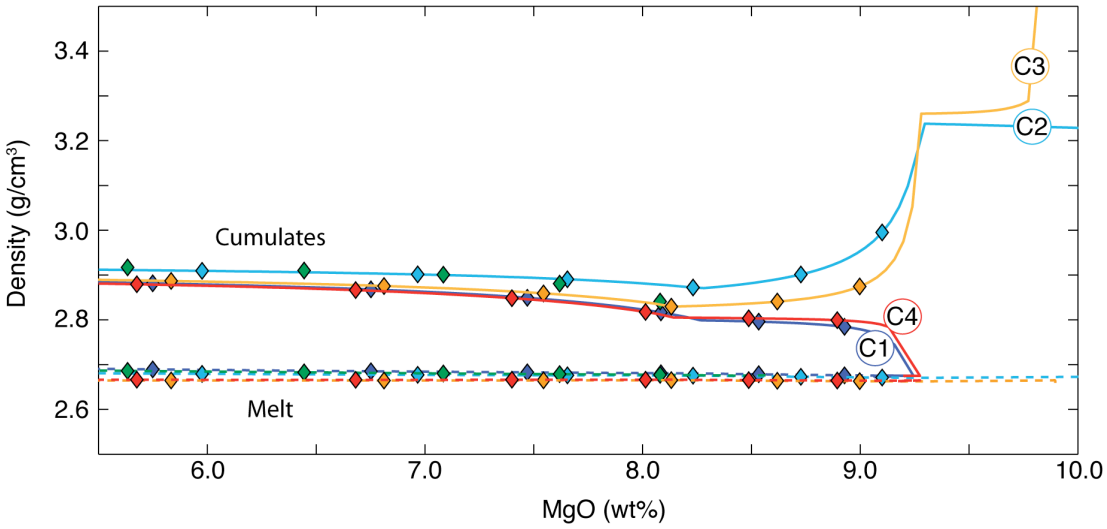

Figure 3.5. Density calculations for composition variation models. Cumulate (solid lines) and melt (dashed lines) densities for melt compositions C1-C4 at 0.5 kbar (AMC depth). Diamond markers along density curves indicate progressive degrees of crystallization in 10% increments (see Fig. 3.3). Cumulate density curves are labeled by melt composition and line colors match corresponding melt density curves and calculated liquid lines of descent (shown in Fig. 3.4).

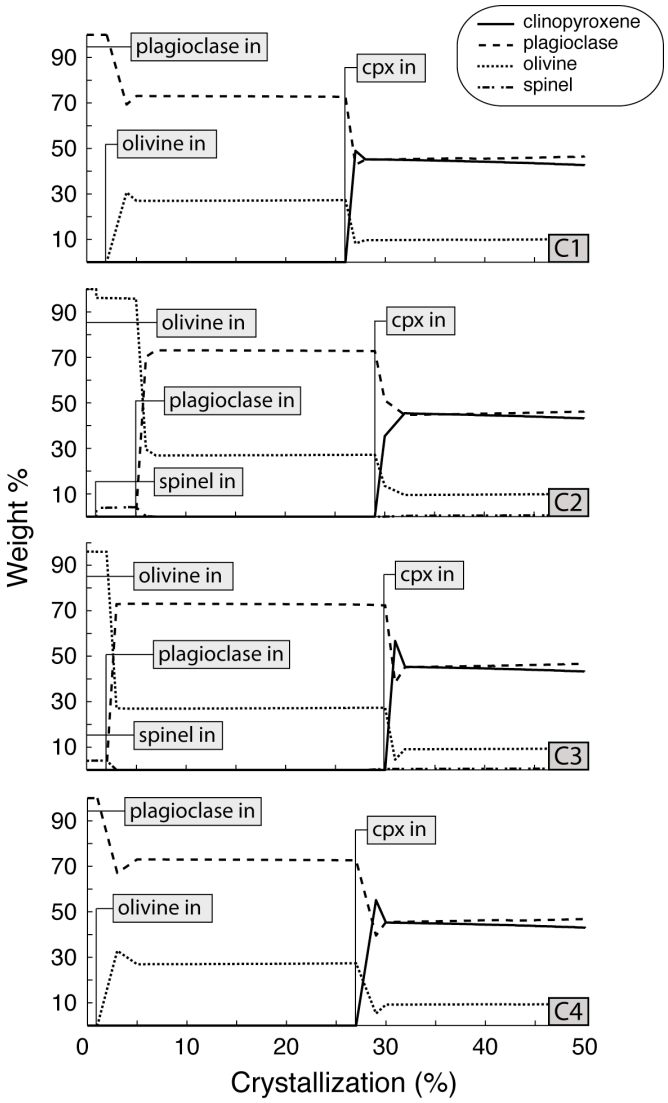

Figure 3.6. Mineral crystallization data for composition variation models. Plots of mineral crystallization data for melt compositions C1-C4 at 0.5 kbar (AMC depth). Mineral crystallization data curves indicate wt% of total cumulates between 0% and 50% crystallization. Lower, right-hand labels indentify the melt composition. Markers identify where minerals first appear in the crystallization sequence.

The effects on cumulate density by different parental melt compositions appear to be related to the extent of fractional crystallization of the parent melt. Spinel and olivine precipitation associated with more primitive melts (C2 and C3) generates high density

cumulates in the earliest stages of crystallization with a rapid decrease in density as crystallization progresses to 10% and beyond. Cumulate densities associated with slightly more evolved melts, on the other hand, begin at much lower values where only plagioclase and olivine precipitate. Only a very small amount of crystallization in the upper mantle (<3%), however, removes the spinel component together with some olivine (see Section 3.3.3.2). This small amount of crystallization results in melt compositions that produce similar cumulate densities, despite their remaining compositional differences (e.g., C1-C2, and C3-C4). Because geochemical evidence suggests that some amount of upper mantle crystallization occurs in melts along the northern EPR (e.g., Goss et al., 2010), we used the slightly more evolved parental melt composition for the remainder of our study, which is C4 as noted in Section 3.2.

3.3.2. H_2O content

The results from our modeling with different H_2O contents at AMC depth indicate that slight variations in H_2O content within the parental melt can account for much of the variation we see in major element data from the EPR (Fig. 3.7). The model with 0.2 wt% H_2O matches the TiO_2, Al_2O_3 and FeO_T data trends the best with the anhydrous and 0.4 wt% models bounding the variance in most of the data. Again, CaO is the exception at less than ~7.5 wt% MgO.

The effects of initial H_2O content on both cumulate and residual melt densities are shown in Figure 3.8. Variance in cumulate density mostly occurs in the earliest stages of crystallization, which is due to the suppression of plagioclase crystallization as H_2O is

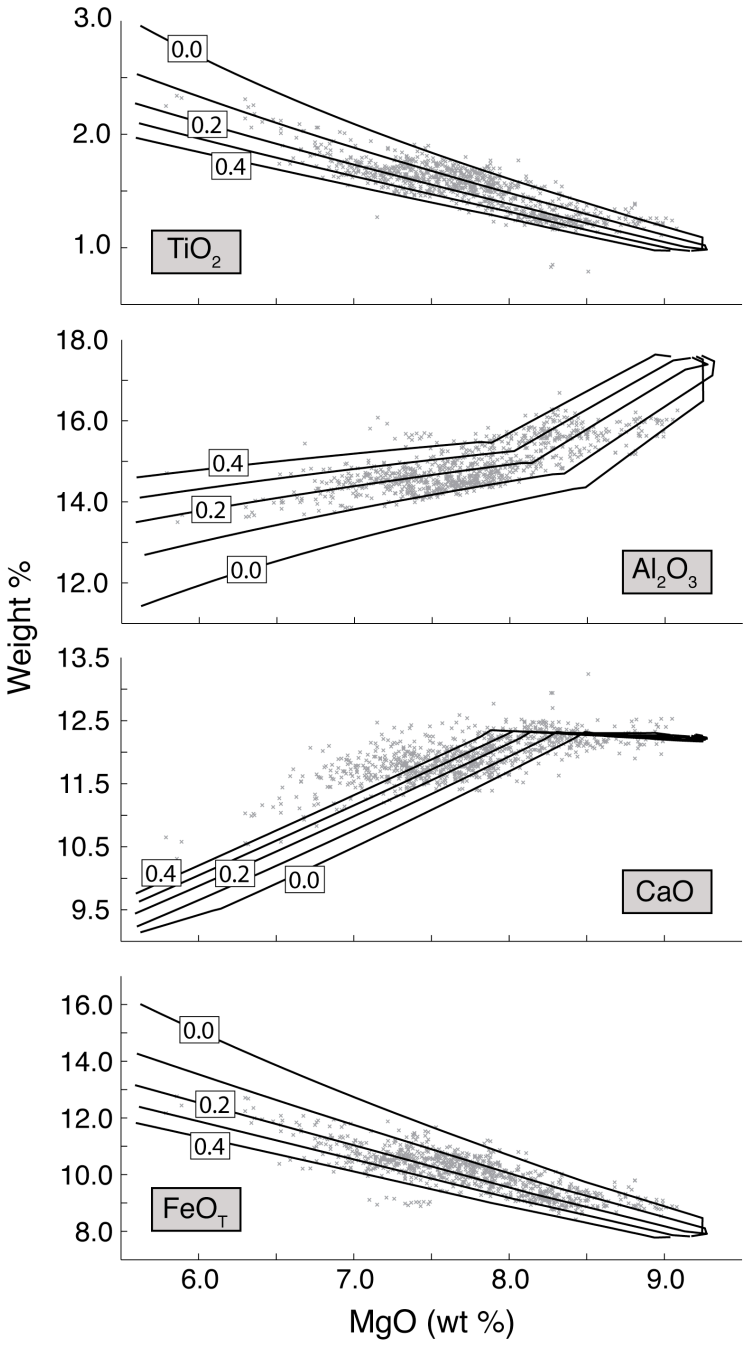

Figure 3.7. Calculated liquid lines of descent for H_2O variation models. Liquid lines of descent for H_2O variation models are calculated at 0.5 kbar (AMC depth). Modeling method, modeling parameters and major element data are the same as Figure 3.4. Starting H_2O concentrations vary between 0.0 (anhydrous) and 0.4 wt% using the general melt composition for C4.

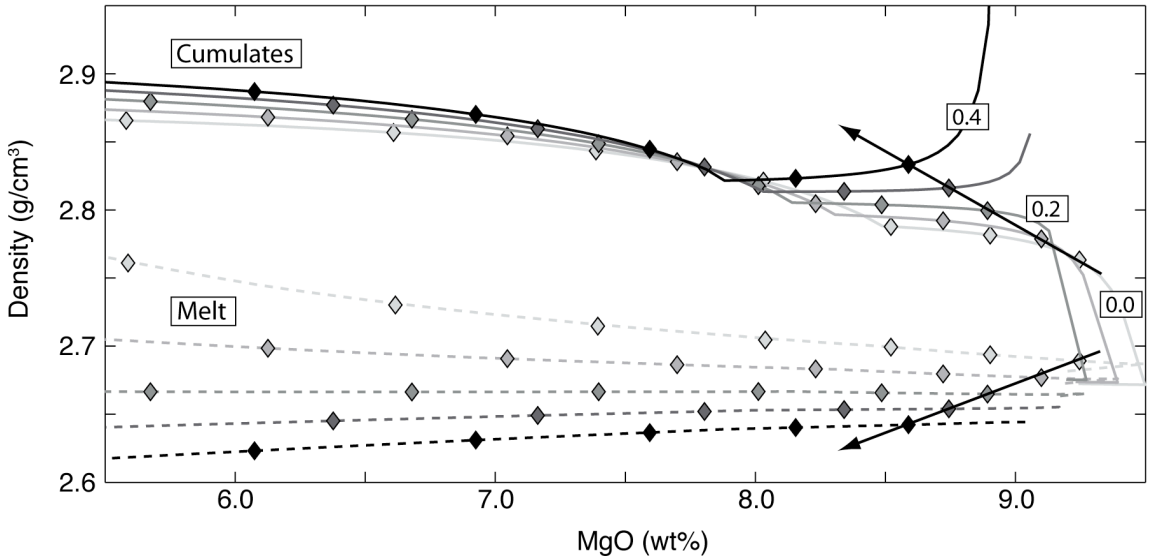

Figure 3.8. Density calculations for H_2O variation models. Cumulate (solid lines) and melt (dashed lines) densities for H_2O variation models at 0.5 kbar (AMC depth). Diamond markers along density curves indicate progressive degrees of crystallization in 10% increments (see Fig. 3.3). Cumulate density curves are labeled by initial H_2O content for the 0.0, 0.2 and 0.4 wt% models, and line shades match corresponding melt density curves. Arrows highlight cumulate and melt data trends at 10% crystallization.

increased (Fig. 3.9). Cumulate densities are initially much lower (~2.7 g/cm^3) in the 0.0-0.2 wt% models, where plagioclase is the first mineral to precipitate. As H_2O content increases to values above 0.2 wt%, olivine precipitates first, which results in much higher starting cumulate densities (>2.85 g/cm^3). Despite the significant density variation observed early on (>8.0 wt% MgO), density values converge for all models as clinopyroxene joins the mineral assemblage. Arrows through the 10% crystallization markers (Fig. 3.8) for these models highlight density data trends due to the effect of increasing H_2O on plagioclase precipitation (i.e., higher density cumulates) as well as suppression of liquidus temperatures as initial H_2O content increases in the parent melt.

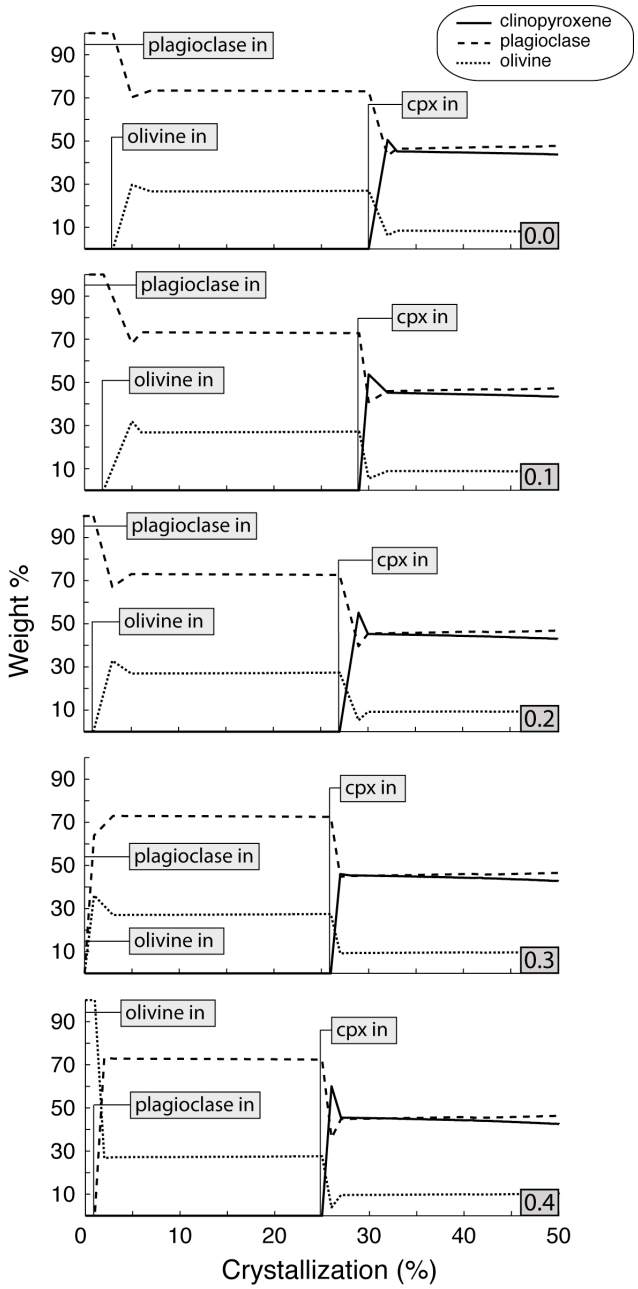

Figure 3.9. Mineral crystallization data for H_2O variation models. Plots of mineral crystallization data for melt composition C4 with H_2O contents varying from 0.0 to 0.4 wt% at 0.5 kbar (AMC depth). Mineral crystallization data curves indicate wt% of total cumulates between 0% and 50% crystallization. Lower, right-hand labels indentify the initial H_2O content. Markers identify where minerals first appear in the crystallization sequence.

Differences in melt density curves are directly related to the initial amount of H_2O present in the system, where more H_2O lowers melt density. The divergence observed in the melt density data between the different models results from an increased concentration of incompatible H_2O in the residual melt as crystallization progresses.

Similar to melt composition, the effects of H_2O content on cumulate density occur in the earliest stages of crystallization. Despite initial differences, cumulate density curves converge when clinopyroxene joins the mineral assemblage (~8 wt% MgO). We note here that variations in H_2O concentration observed in glass samples from the 9°-10°N region of the EPR may be the result of varying degrees of fractionation as opposed to variations in parental sources, especially between on- and off-axis samples (le Roux et al., 2006). According to our results, however, a smaller range of initial H_2O values primarily reduces the range of cumulate densities in the earliest stages of crystallization, since cumulate density curves are similar for all models once clinopyroxene is present.

3.3.3. Crystallization depth

Here we show modeling results from varying the depth of crystallization (pressure). In the following subsections, all density plots include density curves from composition C4 calculated at AMC depth (Fig. 3.3) for reference as it represents our single-stage, AMC crystallization model (see Section 3.2). The C4 density curves are displayed as dashed lines (Figs. 3.10 and 3.14). Throughout the text, we refer to cumulate density and melt density differences between a specific model of interest and

C4 as $\Delta\rho_{cumulate}$ and $\Delta\rho_{melt}$ respectively, and we consider $\Delta\rho$ values to be positive if densities from the model of interest are greater than those of our reference model.

3.3.3.1. Moho crystallization effects

We first compare Moho crystallization with AMC crystallization, which is described as Stage 1 in our two-stage model (see Section 3.2; Fig. 3.2b). Density curves for Moho and AMC crystallization are shown in Figure 3.10a (solid and dashed lines, respectively). Crystallization in each case begins at an MgO value of ~9.2 wt%, with plagioclase precipitating first and olivine joining the assemblage at ~2% crystallization (Fig. 3.11, a and b). A significant change in cumulate density begins to occur, however, at ~14% crystallization, where density curves diverge, with Moho crystallization rapidly rising to higher density values. At similar stages of crystallization, $\Delta\rho_{cumulate}$ reaches values of 0.04 g/cm^3 at 20% and 40% crystallization with a maximum of 0.05 g/cm^3 at 30% crystallization. The increase in $\Delta\rho_{cumulate}$ is due to earlier precipitation of clinopyroxene at Moho depth (Fig. 3.11b) compared with that at AMC depth (Fig 3.11a) in the crystallization sequence (14% vs. 27% crystallization, respectively). Although the cumulate density curves begin to converge as crystallization progresses beyond 27%, density values remain higher for Moho crystallization compared with AMC crystallization. Crystallization markers illustrate that melt at Moho depth also becomes more evolved than melt at AMC depth for a given % crystallization (Fig. 3.10). The difference between the melt density curves for these two models is a result of their pressure differences and is inconsequential, since melt density differences between models disappear at AMC depth (second-stage crystallization, see below).

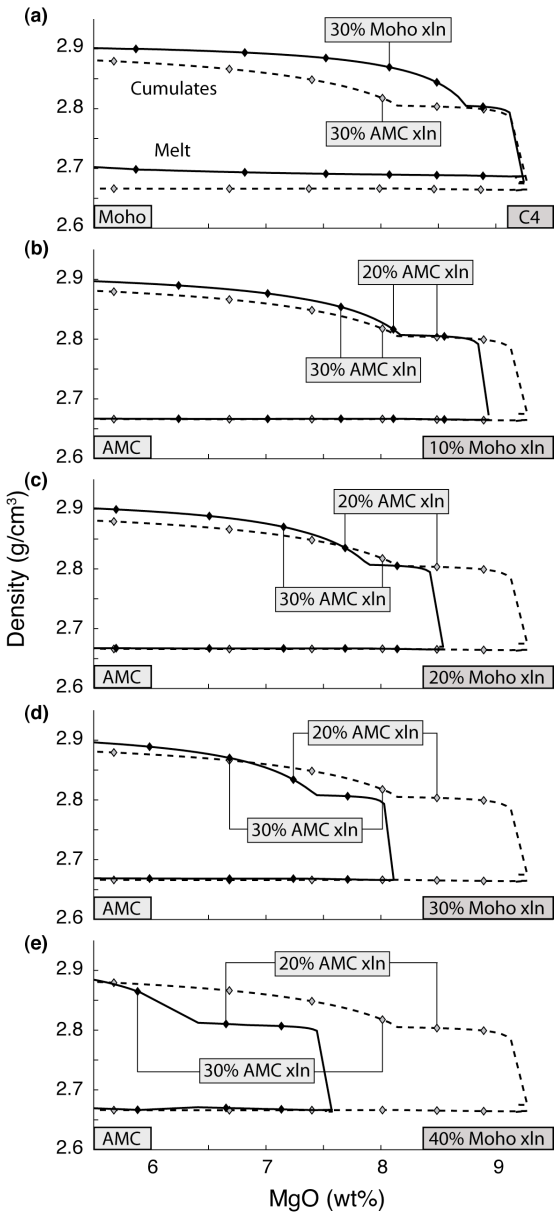

Figure 3.10. Density calculations for the two-stage crustal construction model. Comparisons of cumulate and melt densities (labeled) between the two-stage and single-stage crustal construction models (solid and dashed lines, respectively; see Fig. 3.2b). (a) First stage of two-stage model. Density data comparison between Moho crystallization (2.0 kbar) and AMC crystallization (0.5 kbar) using composition C4. (b)-(e) Second stage of two-stage model. Density data comparisons between melt compositions extracted between 0% and 40% Moho crystallization and composition C4 at AMC depth (0.5 kbar). Diamond markers along density curves in all plots indicate progressive degrees of crystallization in 10% increments (see Fig. 3.3). Lower, left-hand labels identify the depth of crystallization for the two-stage models; lower, right-hand labels identify the melt composition for the two-stage models. Equivalent amounts of crystallization (20% & 30%) between the single-stage and two-stage models are labeled for comparison.

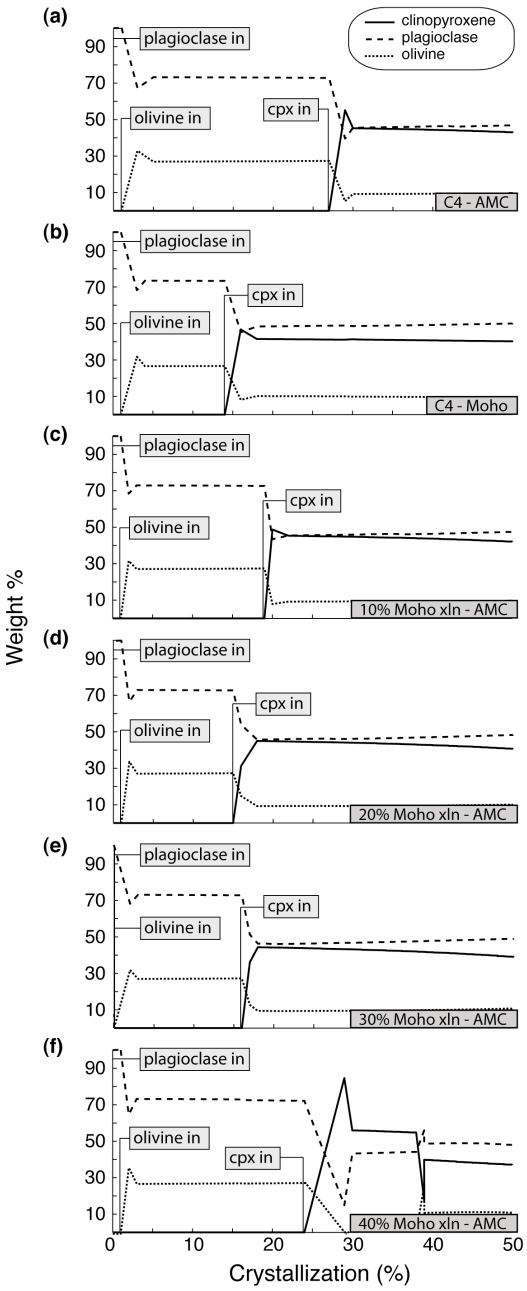

Figure 3.11. Mineral crystallization data for the two-stage crustal construction model. Plots of mineral crystallization data for melt compositions associated with the two-stage crystallization model (Fig. 3.2b). (a) Composition C4 calculated at 0.5 kbar (AMC depth; single-stage model) plotted for comparison. (b) Composition C4 calculated at 2.0 kbar (Moho depth; first stage of two-stage model). (c)-(f) Melt compositions extracted between 0% and 40% Moho crystallization calculated at 0.5 kbar (AMC depth; second stage of two-stage model). Mineral crystallization data curves indicate wt% of total cumulates between 0% and 50% crystallization. Lower, right-hand labels indentify melt composition and model depth. Markers identify where minerals first appear in the crystallization sequence.

Modeling results from the second stage of our two-stage model can account for some of the variation observed in the EPR glass data, especially for Al_2O_3 and CaO (Fig. 3.12). Calculated LLD data for melts that first undergo fractional crystallization at Moho depth (10-50% crystallization) and then are extracted and placed at AMC depth for the remainder of the crystallization sequence (see Section 3.2) help to constrain the amount of deep crystallization that occurs. A comparison with Al_2O_3 and CaO data in particular sets an upper limit on Moho crystallization to ~40% before the LLD moves beyond the bulk of the data. We note that the LLD for melt composition C4 crystallizing at AMC depth only compared to the LLD with 10% initial Moho crystallization are virtually indistinguishable from one another.

Density curves for solid assemblages forming during 10-40% Moho crystallization (solid lines) compared with those of C4 crystallizing at AMC depths only (dashed lines) are shown in Figure 3.10 (b-e). As with the LLD data, the difference between C4 and the 10% Moho crystallization model appears to be insignificant (Fig. 3.10b), but the 10% Moho crystallization model produces melts that are slightly more evolved and, therefore, begin to crystallize later than C4 would at AMC depth only (8.9 versus 9.2 wt% MgO, respectively). Clinopyroxene also joins the existing plagioclase and olivine assemblage at 18% crystallization (Fig. 3.11c) versus 27% crystallization in C4 (Fig. 3.11a). The earlier precipitation of clinopyroxene increases cumulate density sooner in the crystallization sequence, and the density curves between the two models begin to diverge. Only a negligible increase occurs at 10% and 20% crystallization

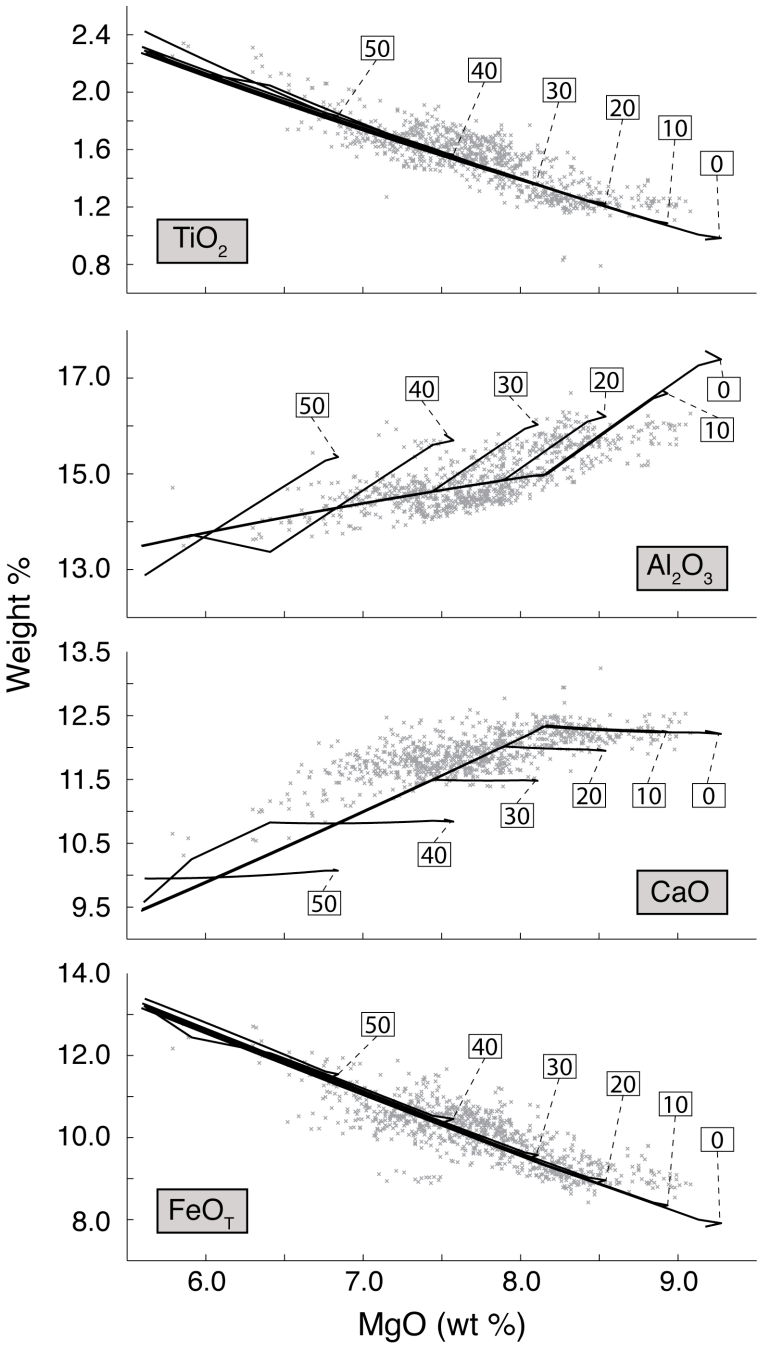

Figure 3.12. Calculated liquid lines of descent for the two-stage crustal construction model. Liquid lines of descent for second stage melt compositions from the two-stage crystallization model calculated at 0.5 kbar (AMC depth). Modeling method, modeling parameters and major element data are the same as Figure 3.4. Starting melt compositions vary between 0% and 50% Moho crystallization starting with composition C4.

($\Delta\rho_{cumulate}$ <= 0.01 g/cm^3), but $\Delta\rho_{cumulate}$ quickly increases and reaches a maximum value of 0.04 g/cm^3 at 30% crystallization.

As our starting melt composition becomes more evolved (i.e., higher degree of crystallization at Moho depth), the plagioclase and olivine crystallization interval shortens and clinopyroxene precipitates earlier (Fig. 3.11). This progression continues until Moho crystallization reaches ~20% (Fig. 3.11d), after which clinopyroxene begins to crystallize later in the sequence (Fig. 3.11e and f). Marked increases in $\Delta\rho_{cumulate}$ for these models (Fig. 3.10), correlate with the timing of the addition of clinopyroxene in the cumulate assemblage. Comparing equivalent stages of crystallization between the 20% Moho crystallization model and C4 (Fig. 3.10c), $\Delta\rho_{cumulate}$ increases to 0.03 and 0.04 g/cm^3 at 20% and 40% crystallization, respectively, and reaches a maximum of 0.05 g/cm^3 at 30% crystallization. Beyond 30% crystallization, density curves begin to converge and $\Delta\rho_{cumulate}$ between the two models continues to diminish. Other than the solidus shift, the density curve for the 30% Moho crystallization model is similar to that of the 20% model with the same $\Delta\rho_{cumulate}$ values between 20% and 40% crystallization (Fig. 3.10d). Although clinopyroxene precipitates later in the crystallization sequence in the 40% model than the three previous models (~24% crystallization sequence), its wt% jumps to >80% (Fig. 3.11f) causing a rapid increase in density (Fig. 3.10e). At 20% crystallization, $\Delta\rho_{cumulate}$ is virtually zero but jumps to 0.05 g/cm^3 at 30% crystallization. Liquid density curves for all Moho crystallization models show no significant deviation from that of C4 ($\Delta\rho_{melt}$ = 0 g/cm^3).

Our cumulate density comparisons between models have, thus far, been limited to equivalent amounts of crystallization. Geochemical data, however, indicate varying degrees of fractionation occur within magmatic/volcanic systems along the northern EPR, where lower average MgO values appear to correlate with axial depth (e.g., Batiza and Niu, 1992; Toomey and Hooft, 2008). We, therefore, also compare densities between models at different stages of crystallization to estimate effects from systems where increased % total crystallization, possibly associated with longer melt residence time, becomes a factor. We consider, for example, systems where the % total crystallization is greater in a Moho crystallization model than C4. Once again matching our 20% Moho crystallization model against C4, this time we compare 30% crystallization to 20% crystallization, respectively. In this case, $\Delta\rho_{cumulate}$ increases to ~0.07 g/cm^3 (Fig. 3.10c). Cumulate density differences continue to increase as crystallization progresses in the 20% Moho crystallization model, and $\Delta\rho_{cumulate}$ reaches ~0.10 g/cm^3 at 50% crystallization, which is within the range of the EPR data (>5.79 wt% MgO). This comparison holds true for all Moho crystallization models, although the extent of crystallization in the more evolved models compared with C4 is constrained by the EPR data.

Our Moho modeling results show that cumulates formed in the lower crust will have a higher density that those formed within the AMC by as much as 0.05 g/cm^3 with equivalent amounts of crystallization. If we consider melt that remains at Moho depth, (i.e., melt sills), cumulate density reaches values of ~2.93 and 2.95 g/cm^3 at 80% and 90% crystallization, respectively ($\Delta\rho_{cumulate}$ ~= 0.12 and 0.14 g/cm^3, respectively,

compared with C4 at 20% crystallization). Moreover, melt compositions that have experienced some degree of crystallization at Moho depth also generate higher density cumulates in the AMC than those with very little (<10%) or no prior Moho crystallization. This paradox seems to result from initial Moho crystallization, which experiences an earlier initiation of clinopyroxene crystallization, producing more evolved melts that continue to precipitate clinopyroxene earlier in the crystallization sequence within the AMC compared with the AMC crystallization only model. Cumulate density increases by as much as 0.05 g/cm^3 with equivalent amounts of crystallization and 0.10 g/cm^3 when factoring in differences in total % fractional crystallization by amounts that are consistent with differences in basaltic glass compositional data. Our modeling results, overall, indicate that a two-stage model with initial Moho crystallization can significantly increase average crustal density. We note here also that the LLD for composition C4 crystallizing at Moho depth only (2.0 kbar), with no subsequent AMC crystallization, does not fit the EPR data (Fig. 3.13), which indicates that melts ascending from the Moho do not likely reach the seafloor without additional shallow crystallization.

3.3.3.2. Upper mantle crystallization effects

Here we show density variation resulting from some initial upper mantle crystallization (3 kbar or ~9 km) compared with AMC crystallization only using a two-stage approach (see Section 3.2; Fig. 3.2c). A significant cumulate density difference occurs at the very beginning of crystallization when comparing upper mantle crystallization with AMC crystallization (Fig. 3.14a; solid and dashed lines, respectively).

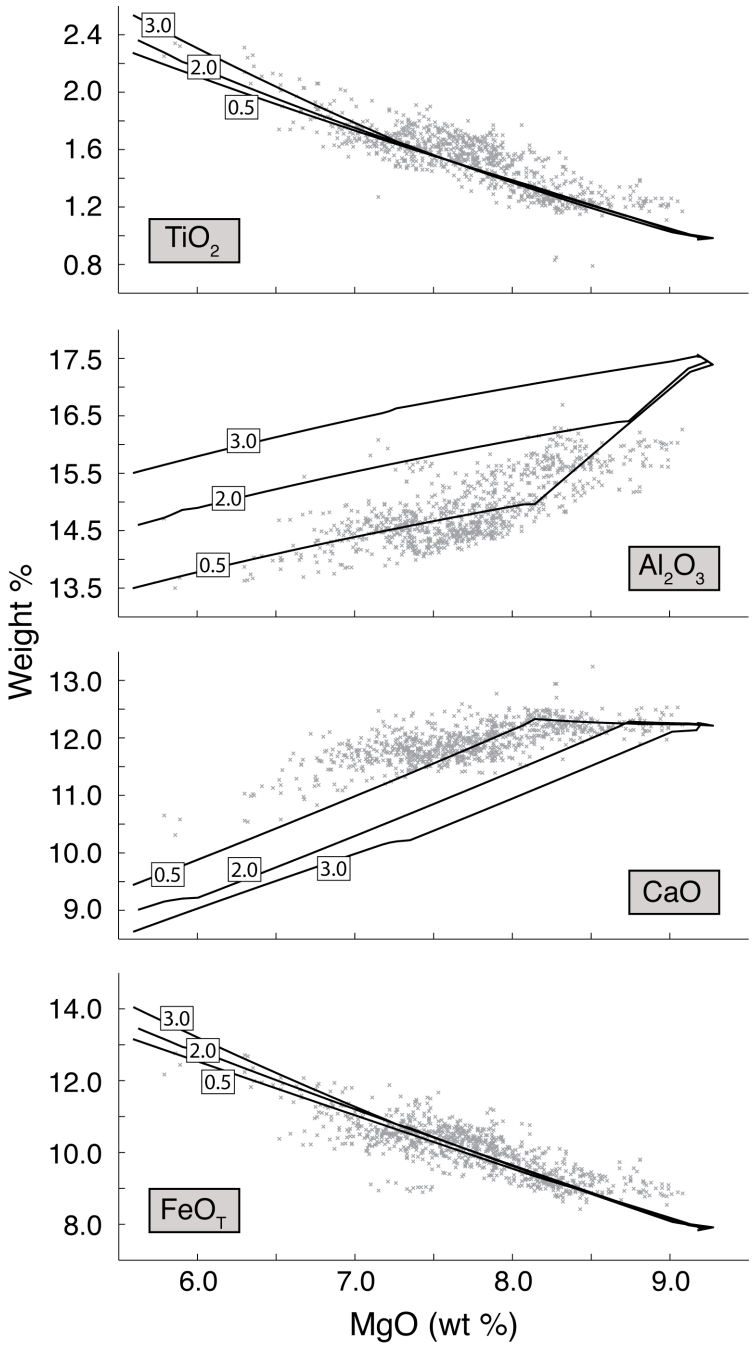

Figure 3.13. Calculated liquid lines of descent for pressure variation models. Liquid lines of descent for composition C4 calculated at 0.5 kbar (AMC), 2.0 kbar (Moho) and 3.0 kbar (upper mantle). Modeling method, modeling parameters and major element data are the same as Figure 3.4.

This difference is due to the very early precipitation of clinopyroxene in the crystallization sequence (Fig. 3.15b). At both 10% and 20% crystallization, $\Delta\rho_{cumulate}$ reaches a maximum value of 0.11 g/cm^3 and then diminishes as cumulate density curves begin to converge when crystallization exceeds ~27% in the AMC crystallization model.

As with our Moho crystallization modeling, we extract melt compositions at 10-50% upper mantle crystallization in 10% increments and compare the models with C4 at AMC depth. The LLD for each of these models is shown in Figure 3.16. The Al_2O_3 data provide an upper bound on mantle crystallization of ~30%, whereas the bulk of the CaO data constrain mantle crystallization to ~20%. Upper mantle crystallization between 10% and 20% may explain some of the higher CaO values observed between 6.5 and 7.5 wt% MgO as well. LLD plots with TiO_2 and FeO_T data do little to provide any constraints because model data overlap and span the entire range of the glass data.

No significant cumulate density differences occur between our 10% upper mantle crystallization model and C4 (Fig. 3.14b), as clinopyroxene precipitates at 27% crystallization in each case (Fig. 3.15, a and c). Unlike Moho crystallization, however, the plagioclase and olivine only crystallization interval actually increases in the 20, 30 and 40% mantle crystallization models, and clinopyroxene joins the assemblage later in the sequence at 38%, 36% and 30%, respectively (Fig. 3.15, d-f). In each of these cases, no cumulate density difference occurs between mantle crystallization models and C4 while crystallization remains below 27% in the C4 model ($\Delta\rho_{cumulate} = 0$ g/cm^3) (Fig. 3.14,

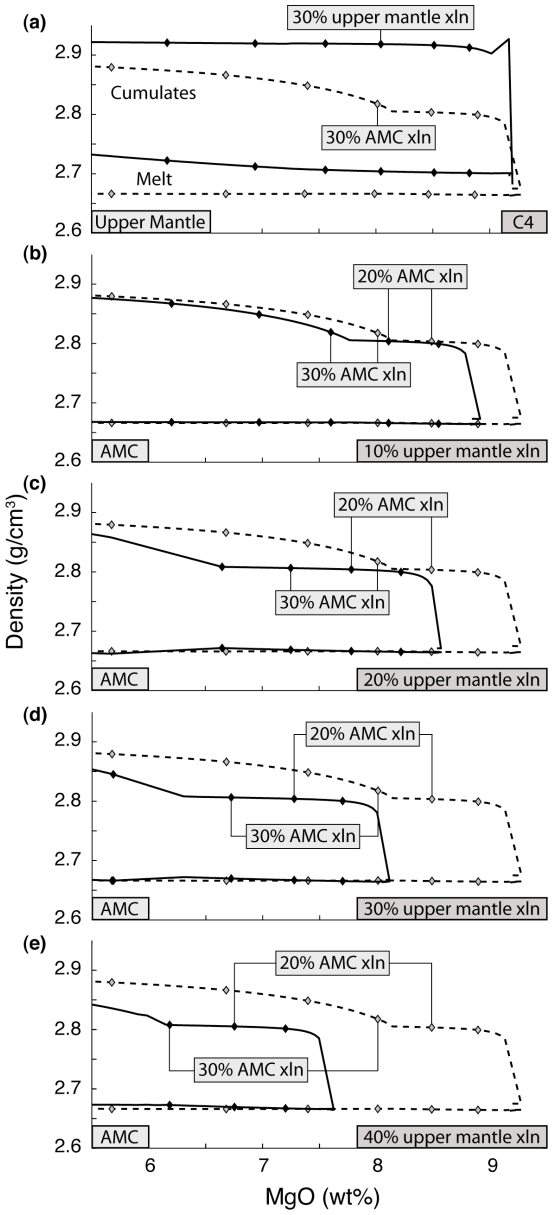

Figure 3.14. Density calculations for upper mantle versus AMC crystallization models. Comparisons of cumulate and melt densities (labeled) between upper mantle and AMC crystallization models (solid and dashed lines, respectively; see Fig. 3.2c). (a) Density data comparison between upper mantle (3.0 kbar) and AMC crystallization (0.5 kbar) using composition C4. (b)-(e) Density data comparisons between melt compositions extracted between 0% and 40% upper mantle crystallization and composition C4 at AMC depth (0.5 kbar). Diamond markers along density curves in all plots indicate progressive degrees of crystallization in 10% increments (see Fig. 3.3). Lower, left-hand labels identify the depth of crystallization for the upper mantle crystallization models; lower, right-hand labels identify the melt composition for the upper mantle crystallization models. Equivalent amounts of crystallization (20% & 30%) between the upper mantle and AMC crystallization models are labeled for comparison.

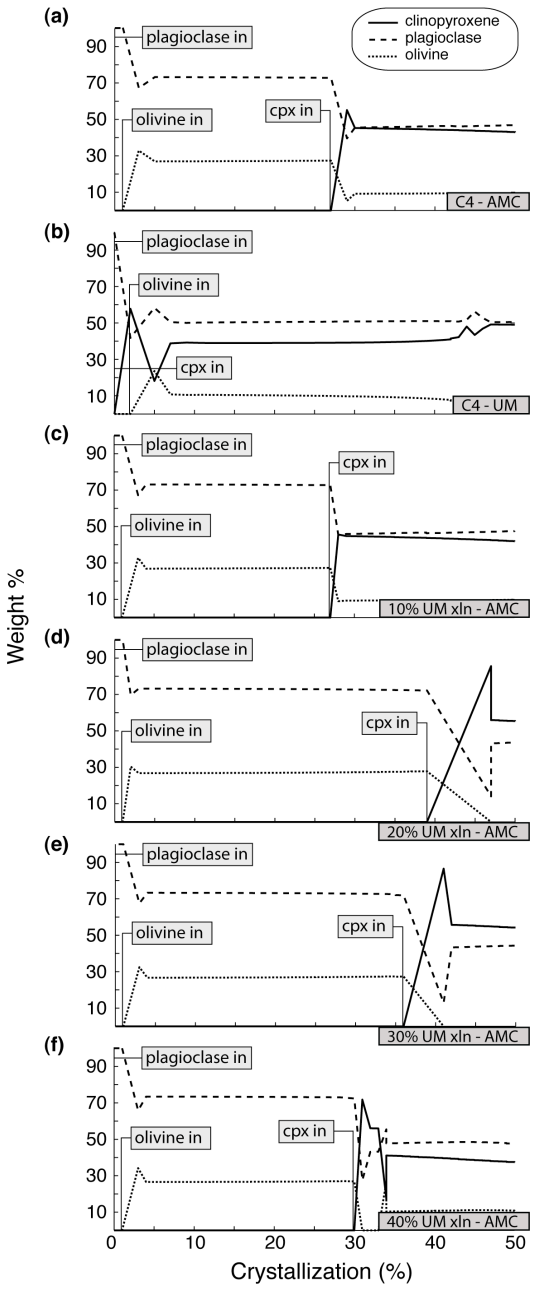

Figure 3.15. Mineral crystallization data for upper mantle versus AMC crystallization models. Plots of mineral crystallization data for melt compositions associated with the upper mantle (UM) crystallization model (Fig. 3.2c). (a) Composition C4 calculated at 0.5 kbar (AMC depth) plotted for comparison. (b) Composition C4 calculated at 3.0 kbar (upper mantle depth). (c)-(f) Melt compositions extracted between 0% and 40% upper mantle crystallization calculated at 0.5 kbar (AMC depth). Mineral crystallization data curves indicate wt% of total cumulates between 0% and 50% crystallization. Lower, right-hand labels indentify melt composition and model depth. Markers identify where minerals first appear in the crystallization sequence.

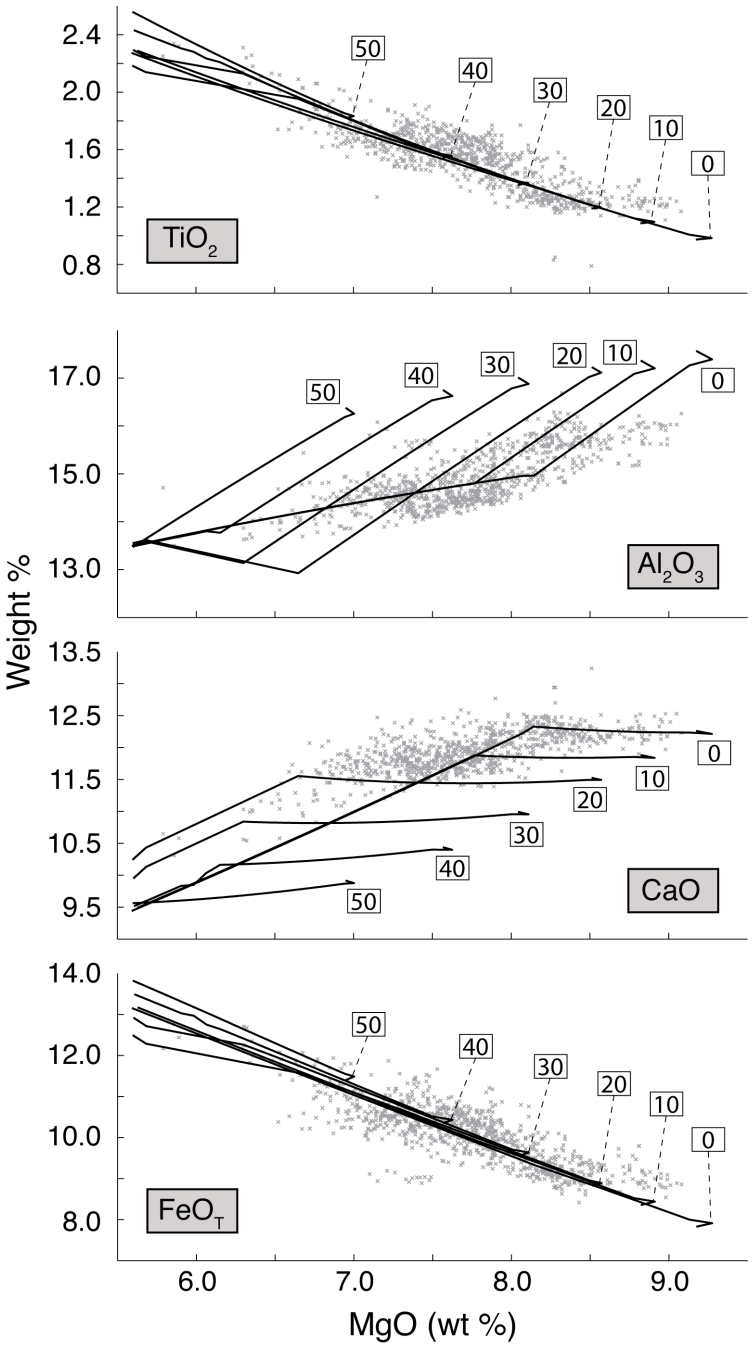

Figure 3.16. Calculated liquid lines of descent for upper mantle versus AMC crystallization models. Liquid lines of descent for melt compositions extracted from the upper mantle crystallization model calculated at 0.5 kbar (AMC depth). Modeling method, modeling parameters and major element data are the same as Figure 3.4. Starting melt compositions vary between 0% and 50% upper mantle crystallization starting with composition C4.

c-e). Beyond 27%, $\Delta\rho_{cumulate}$ values are negative, likely resulting from the exhaustion of clinopyroxene at higher total % upper mantle crystallization.

We also ascertain how upper mantle crystallization affects cumulate density when the melt continues to crystallize at the Moho (Fig. 3.2d). Our results show no significant cumulate density variation occurs, and only the liquidus temperature shifts as the melt composition becomes more evolved (Fig. 3.17) once mantle crystallization reaches 3% (using composition C3; see Section 3.3.1). An initial decrease in cumulate density between 0% and 3% crystallization comes from the removal of spinel and a small amount of olivine at the onset of crystallization. Melt compositions with an additional 10% and 20% upper mantle crystallization behave similarly when crystallizing at Moho depth.

Our modeling results indicate that a significant increase in cumulate density ($\Delta\rho_{cumulate} > 0.1$ g/cm^3) does occur during upper mantle crystallization, although these cumulates are in the mantle and not the crust. Slightly shallower crystallization within a thickened Moho transition zone (MTZ) (e.g., Kelemen et al., 1997; Korenaga and Kelemen, 1997), however, may produce cumulates of similar density that would contribute to higher average crustal density values. Our results also show that 10% upper mantle crystallization has little impact on resultant cumulate densities in the AMC or at the Moho, and the EPR data constrain the extent of upper mantle crystallization to ~20%. As with Moho crystallization, the LLD for composition C4 crystallizing at upper mantle depth (3.0 kbar) does not fit the EPR data (Fig. 3.13), which indicates that melts

ascending from the upper mantle do not likely reach the seafloor without additional crystallization.

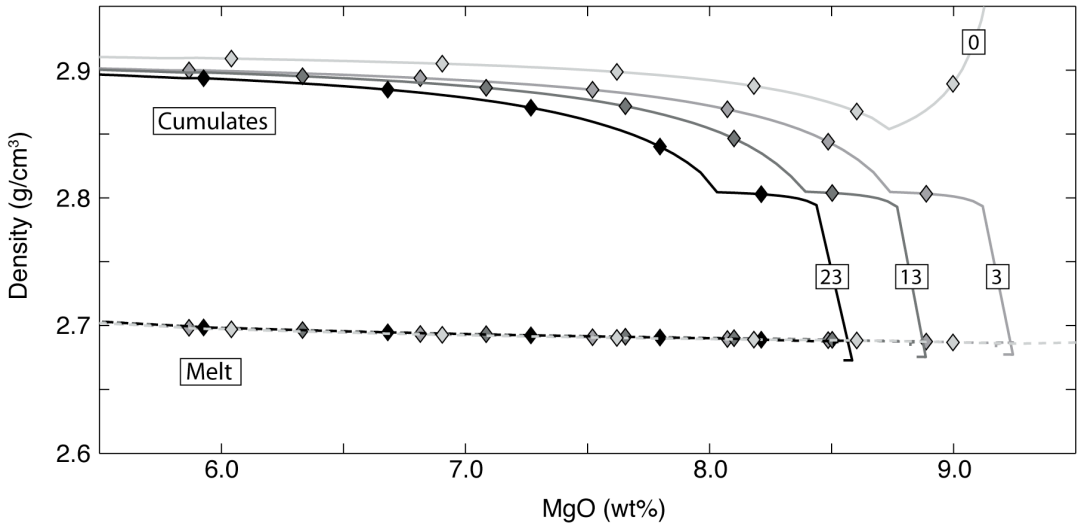

Figure 3.17. Density calculations for upper mantle versus Moho crystallization models. Cumulate (solid lines) and melt (dashed lines) densities for melt compositions extracted during varying stages of upper mantle crystallization (0-23% crystallization starting with composition C3) calculated at Moho depth (2.0 kbar; see Fig. 3.2d). Diamond markers along density curves indicate progressive degrees of crystallization in 10% increments (see Fig. 3.3). Cumulate density curves are labeled by melt composition (i.e., % of upper mantle crystallization), and line shades match corresponding melt density curves.

3.3.4. The significance of clinopyroxene

Based on our modeling results and a comparison with existing glass geochemical data, we conclude that variations in parental melt major element composition or initial H_2O content are not likely to be the primary factors in controlling lower crustal density variations along the northern EPR. Our parental melt comparison shows that a significant amount of cumulate density variation occurs in the earliest stages of crystallization due to

the precipitation of spinel and olivine in the most primitive compositions. Although some slight variations may occur in primary melt compositions (e.g., Perfit et al., 1996; Goss et al., 2010), our modeling results indicate that only a small degree of upper mantle crystallization (<3%) causes resultant cumulate densities associated with further AMC or Moho depth crystallization to be similar, regardless of compositional differences.

Variations in initial H_2O content similarly result in significant amounts of cumulate density variation in the earliest stages of crystallization, which is primarily attributed to the suppression of plagioclase in the crystallization sequence. As previously mentioned, however, a smaller range of initial H_2O content reduces the range of cumulate densities prior to clinopyroxene crystallization and has no significant impact on clinopyroxene precipitation itself.

Our modeling results show that cumulate density curves for both the compositional and H_2O variation models converge when clinopyroxene precipitates (~8 wt% MgO at 0.5 kbar), which indicates that the addition of clinopyroxene to the cumulate assemblage is the common factor governing cumulate density variation. Although it is well know that the clinopyroxene precipitation is pressure sensitive (e.g., Michael and Chase, 1987; Villiger et al., 2007), our modeling results suggest that even small pressure differences, such as that between AMC and Moho depths (~1.5 kbar), can significantly affect the onset of clinopyroxene precipitation in the crystallization sequence. The presence or absence of clinopyroxene in the cumulate assemblage, in turn, generates higher or lower cumulate densities, respectively.

3.4. Discussion

When we consider the relations between clinopyroxene precipitation, crystallization depth and cumulate density in the context of our crustal construction models (Fig. 3.2, a and b), we see that magmatic systems where the majority of crust is formed from shallow AMC crystallization (single-stage model) produce less dense crust than those where the crust has a significant contribution from deeper crustal crystallization (two-stage model), especially if the two-stage model includes an increased % total crystallization and formation of lower crustal sills (e.g., Boudier et al., 1996; Kelemen et al., 1997; Kelemen and Aharonov, 1998). Moreover, when combining our modeling results with geophysical and geochemical data from the 9°-10°N region of the EPR, it is evident that magmatic systems associated with axial highs (less dense crust) appear to be similar to the single-stage model and progressively become more two-stage-like towards axial lows.

Axial variation in magmatic systems along the EPR is supported by plutonic rock data sampled at both Hess Deep and Pito Deep (Coogan et al., 2002; Perk et al., 2007; Natland and Dick, 2009). Samples collected from these two locations indicate that significant differences in the amount of lower crustal crystallization do occur along sections of the EPR with similar spreading rates, evidenced by plutonic rocks exposed at Pito Deep (Perk et al., 2007) that are more primitive than those found at Hess Deep (Coogan et al., 2002). Perk et al. (2007) attribute the differences between these two locations to temporal or spatial heterogeneities in the magma plumbing system, a phenomenon well observed along the 9°-10°N region of the EPR (e.g., Langmuir et al.,

1986; Kent et al., 1993; Toomey et al., 1990; Smith et al., 2001; Canales et al., 2003; Toomey et al., 2007). Perk et al. (2007) also present conceptual models similar to our single-stage and two-stage models, where they associate the more primitive Pito Deep crust with a "gabbro-glacier" like model and the more evolved Hess Deep crust with a hybrid accretion model (which includes in situ crystallization in the lower crust accompanied by cumulates subsiding from the AMC).

Our modeling results also show that sills emplaced in the lower crust that undergo extensive amounts of crystallization (>80%) generate high-density cumulates. In addition to the earlier precipitation of clinopyroxene at depth, significant amounts of melt fractionation will produce iron-titanium (Fe-Ti) enriched oxide gabbros (Grove et al., 1992), which have higher density and lower seismic velocities than do olivine gabbros (Iturrino et al., 1991). A systematic increase in lower crustal crystallization along the northern EPR from the axial high at 9°50′N toward the axial low at the OSC is consistent with seismic and gravity observations (e.g., Madsen et al., 1990; Barth and Mutter, 1996; Wang et al., 1996; Canales et al., 2003). Moreover, evidence for the emplacement of lower crustal sills is found at Hess Deep (Perk et al., 2007; Natland and Dick, 2009) and in the Oman ophiolite complex (e.g., Boudier et al., 1996; Kelemen et al., 1997; Kelemen and Aharonov, 1998).

In addition to crystallization depth, variation in the degree of AMC crystallization also plays a significant role in cumulate density variation. Our modeling results indicate that in order to generate higher density crust on the order observed along the 9°-10°N

region of the EPR, there must be a systematic increase in the degree of AMC crystallization from the axial high to the axial low. Geochemical and geophysical data from this region show that the chemistry of axial lavas does vary along axis, and the variations correlate roughly with axial depth (Detrick et al., 1987; Batiza and Niu, 1992; Toomey and Hooft, 2008). Average MgO values decrease and FeO values increase systematically from the axial high near 9°50′N southward toward the 9°03′N OSC, and eruption temperatures also correlate with axial depth (Batiza and Niu, 1992). We observe the continuity of the MgO trend in the more recent EPR data (see Section 3.2) used in our study. Although the entire data set includes samples collected within 5 km of the rise axis, we eliminate any off-axis geochemical anomalies potentially affecting these results by filtering the data to samples collected within 1 km of the rise axis and find no significant change in the MgO trend.

Because higher crustal density also correlates with regions of off-axis mantle upwelling (Toomey and Hooft, 2008), we suggest that lateral transport of melt to the rise axis, by up to 20 km or more (Toomey et al., 2007; Durant and Toomey, 2009) generates flow conditions favorable for deep crystallization. Moho-depth crystallization is inferred to occur during and/or post-migration, likely thickening the MTZ (e.g., Kelemen et al., 1997; Korenaga and Kelemen, 1997) and delivering a comparatively lower flux of cooler, more evolved melt to the AMC. Axial melts associated with an off-axis melt source are, thereby, less likely to erupt, which results in longer magma chamber residence times and higher degrees of crystallization. We also suggest that regions of rise-centered upwelling generate flow conditions favorable for shallow crystallization, where mantle melt ascends

more efficiently to the AMC before any significant fractionation can occur. A higher flux of hotter and more primitive melts delivered to the AMC will likely drive more frequent eruptions (i.e., shorter magma chamber residence times) with lower degrees of crystallization.

We agree with Perk et al. (2007) that variations in hydrothermal regimes likely also play a significant role in the amount of lower crustal crystallization that occurs along the northern EPR. We infer that axial melts originating from an off-axis melt source will retard volcanic activity, thereby generating a tectonically dominated setting that allows for greater fissure density to develop in the shallow crust and deeper faulting to occur in the lower crust (e.g., Fornari et al., 1998). Deep crustal faults, in turn, may allow for deeper penetration of seawater, which provides a source for heat extraction and lower crustal crystallization. Additional crystallization in the lower crust would reduce melt flux to the AMC and potentially slow volcanic activity even further, creating a positive feedback loop. We suggest that such deep hydrothermal systems are likely associated with more diffuse, low-temperature seafloor venting (e.g., Haymon et al., 1991). Conversely, we infer that axial melts associated with a rise-centered melt source will drive more frequent volcanic activity, which reduces fissure density (e.g., Fornari et al., 1998) as well as the likelihood of deep crustal faulting. Hydrothermal circulation is, therefore, confined to the shallow crust, which results in focused, high temperature venting (e.g., Haymon et al., 1991) and less lower crustal crystallization.

In summary, we illustrate our inferences from our modeling results and geophysical and geochemical observations we have discussed thus far by contrasting two conceptual axial magmatic/volcanic systems at: (1) an axial high, which overlies a region of rise-centered melt accumulation, and (2) an axial low that lies adjacent to a region of off-axis melt accumulation (Fig. 3.18). We associate the system at the axial high with a single-stage or "gabbro-glacier" style model (Fig. 3.18a). In this model, the majority of lower crust is formed from subsiding cumulates originating in the AMC with less than ~25% average crystallization. Small amounts of crystallization (up to ~10%) may occur in the upper mantle or at the Moho without having any significant effect on AMC or lower crustal cumulate densities. Geologic conditions associated with this single-stage model include a shallow AMC, small eruption volumes with relatively short eruption intervals and high eruption temperatures, comparatively high average MgO values and younger lavas, lower fissure density and a shallow (upper crustal) hydrothermal system with focused, high-temperature seafloor venting. Conversely, we associate the system at an axial low with a hybrid, two-stage model (Fig. 3.18b). In this model, the lower crust is formed by a combination of Moho depth crystallization (~20-30%) and AMC crystallization of more evolved melts. This model also includes crystallizing sills in the lower crust or upper mantle, which potentially thicken the MTZ. Geologic conditions associated with the hybrid, two-stage model may include a relatively smaller and deeper AMC, larger eruption volumes with longer eruption intervals and lower eruption temperatures, comparatively low average MgO values and older lavas, higher fissure density with deep crustal faulting and a deep hydrothermal system with diffuse, low-temperature seafloor venting.

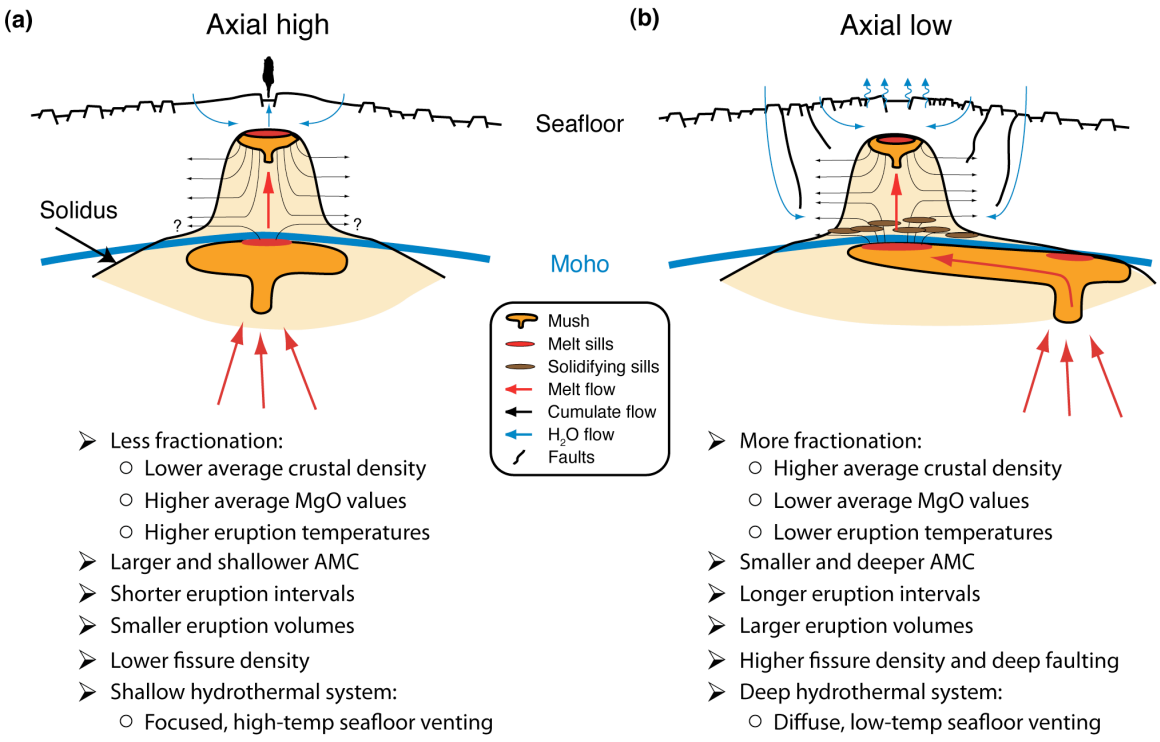

Figure 3.18. Variation in axial magmatic systems due to rise-centered versus off-axis delivery of mantle melt. Conceptual illustration contrasting axial magmatic/volcanic systems associated with (a) rise-centered versus (b) off-axis melt supply. Geophysical and geochemical conditions associated with each system are listed for comparison. Geologic features are not to scale. Figure modified from Toomey et al. (2007). (a) Axial high associated with rise-centered melt supply. Lower crust is formed by subsiding cumulates originating within the AMC. Small amounts of crystallization may occur in the lower crust or upper mantle (~10%); question marks indicate uncertainty in the extent of lower crustal crystallization. (b) Axial low associated with the off-axis delivery of mantle melt. Lower crust is formed by a combination of Moho depth crystallization (~20-30%), subsiding cumulates from AMC crystallization and crystallizing melt sills in the lower crust and/or MTZ.

Thus far, I have focused on the geological consequences of off-axis melt accumulation and subsequent melt delivery to the rise axis. In the following chapter, I examine the sensitivity of *Pn* travel time data to marine crustal and mantle heterogeneity, which could potentially affect tomography results and associated interpretations.

CHAPTER IV

THE SENSITIVITY OF *Pn* IN MARINE SEISMIC TOMOGRAPHY

This chapter is co-authored by Douglas R. Toomey. I conducted the waveform modeling and analysis and wrote the chapter. Douglas R. Toomey conducted the travel time modeling, provided essential guidance with the research and edits to the chapter. This chapter is currently in preparation for publication.

4.1. Introduction

Head waves are seismic waves that intersect an interface separating lower-to-higher velocity media at or beyond the critical angle. The energy of the head wave, also known as a refracted wave, propagates at the higher velocity and is continuously refracted back into the lower velocity medium at the critical angle (e.g., Aki and Richards, 2002; Stein and Wyssesion, 2003). In the infinite frequency (ray path) approximation, head waves are often represented as traveling along the interface. However, when considering finite frequencies, head waves sample structure over a finite volume that is located at and below the interface. Oceanic *Pn* is a sub-crustal arrival that is taken to be a head wave and is commonly used in local travel time tomography (e.g., Dunn et al., 2000; Toomey et al., 2007). Even in the presence of a small vertical velocity gradient, *Pn* is typically treated as a true head wave at distances used in local seismic studies (<100 km) where *Pn* remains close to the crust-mantle boundary or Moho. Because *Pn* energy travels near the Moho, it is useful for resolving the topmost mantle velocity structure.

Here we present the results of a numerical study conducted to investigate the sensitivity of *Pn* travel time data to variations in structure near the Moho in a mid-ocean ridge environment. We use a combination of ray tracing and waveform modeling to evaluate the effects of sub-axial crustal thickness variations, mantle low-velocity zone (MLVZ) thickness variations, a vertical velocity gradient in the mantle and crust-mantle velocity contrast variations on travel times and Fresnel zones associated with *Pn* energy propagating through a cross-axis, mid-ocean ridge model (Fig. 4.1). We compare our results with a recent marine tomography study along the fast-spreading, northern East Pacific Rise (EPR) (Toomey et al., 2007), where the observed range of *Pn* travel time anomalies is ~350 ms. We also demonstrate the ability of using *Pn* in local travel time tomography to resolve velocity structure a few kilometers beneath the Moho and show that smoothing constrains can be used to effectively approximate *Pn* wave behavior.

4.2. *Pn* modeling

We use a combination of graph-theory-based ray tracing (Moser, 1994; Toomey et al., 1994) and 2-D finite difference waveform modeling to calculate *Pn* travel times. For our waveform modeling, we use E3D, which is an explicit 2D/3D elastic finite difference wave propagation code that is 4^{th}-order accurate in space and 2^{nd}-order accurate in time (Larsen and Harris, 1993; Levander, 1988). Our model space is 60 km long by 15 km deep with a nodal spacing of 10 m in each direction (Fig. 4.1). We use free-surface and absorbing boundary conditions along the top and sides of the model, respectively. A 5-km-wide attenuation boundary is added to the sides and bottom of the model space to reduce reflected boundary energy that remains within the model, thereby

producing a total of 7001 x 2001 nodes. The model space consists of a 1-km-thick water layer, 6-km-thick crust (0.5-km-thick extrusive layer (2A), 1.5-km-thick sheeted dike layer (2B) and 4-km-thick gabbroic layer (3)) and an 8-km-thick mantle section. No topography is included in the models. The source consists of a Ricker wavelet with a center frequency of 10 Hz placed at 5 km range (above station 1) and 10 m below sea level (Fig. 4.1, star). Background velocity (Fig. 4.2a) and attenuation profiles as well as density calculations are similar to those used by Durant and Toomey (2009).

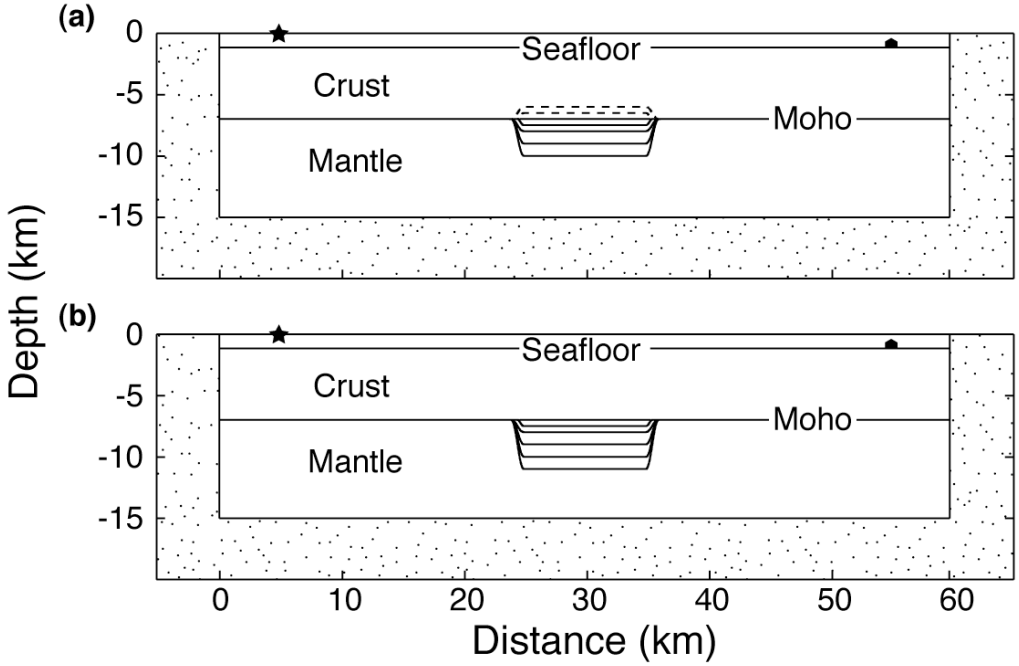

Figure 4.1. Finite difference models for crustal thickness and MLVZ thickness variation. Cross-axis mid-ocean ridge model space that is 60 km wide x 15 km deep with a 5-km-wide attenuation buffer added to the sides and bottom (dotted region) to improve boundary conditions. Center of the model represents the ridge axis. Source (solid star, left) and receiver (solid dome, right) locations are shown. (a) Finite-difference Models 1-7. Model 1 is the reference model (flat Moho), and Models 2-7 contain a 10-km-wide sub-axial crustal root (solid lines) or anti-root (dashed lines). (b) Finite-difference Models 8-12, which include a sub-axial MLVZ of varying thickness (see Table 4.1).

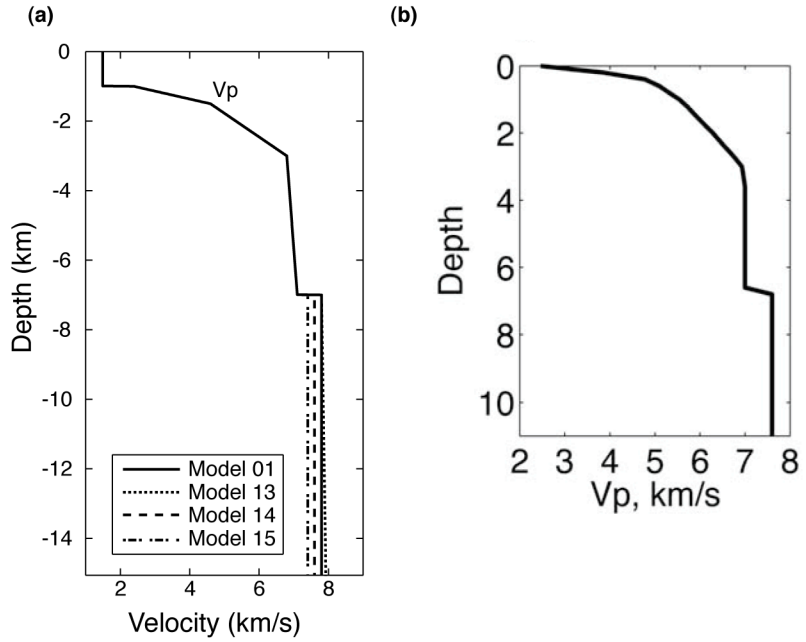

Figure 4.2. Velocity-depth profiles for finite difference and ray tracing models. (a) *P* wave velocity depth functions for our finite difference reference model (Model 1, solid line), model with mantle vertical velocity gradient of ~0.015 s^{-1} (Model 13, dotted line) and models with crust-mantle velocity contrast variations of 7.1-7.6 km s^{-1} (Model 14, dashed line) and 7.1-7.4 km s^{-1} (Model 15, dot-dashed line). (b) *P* wave velocity depth function for ray tracing models. Mantle velocity is 7.6 km s^{-1} with 6% anisotropy (fast axis lies in the plane of Figs. 4.3 (top), 4.5 and 4.6).

We run 15 separate finite difference models, which include a variety of crustal or mantle velocity anomalies. Model 1 is laterally homogeneous and is used as our reference model (Fig. 4.2a). The effects of sub-axial crustal thickness variations on *Pn* travel times are evaluated in Models 2-7 by adding a 10-km-wide crustal root with thickness values that range between -1 and 3 km at 500 m increments (Fig 4.1a). *Pn* travel time sensitivity to a low-velocity anomaly (Δv = 0.4 km s^{-1}) beneath the Moho is evaluated in Models 8-12 with a 10-km-wide MLVZ that begins at the Moho and varies in thickness by 0.5, 1, 2, 3 and 4 km, respectively (Fig. 4.1b). We also test the effects of

a vertical velocity gradient (~0.015 s^{-1}) in the mantle on *Pn* travel time in Model 13 (Fig. 4.2a), and in Models 14 and 15 we investigate *Pn* travel time sensitivity to crust-mantle velocity contrast variations by lowering mantle velocities from 7.8 to 7.6 and 7.4 km s^{-1}, respectively (Fig. 4.2a). Travel time data are collected for a synthetic station located 50 km from the source (Fig. 4.1, dome), and resultant *Pn* delays are determined by comparing *Pn* arrival times from our anomalous models (Models 2-15) with those from our reference model (Model 1).

We also estimate the first Fresnel zone for a 10 Hz head wave by using the single-scatterer Born approximation, where the Fresnel zone is determined by evaluating forward-propagating energy from the source and backward-propagating energy from the receiver to every single scatterer near the minimum travel time path (or ray path) (Dahlen et al., 2000; Nolet et al., 2005). Arrival times and amplitudes for head waves are found to be influenced by the 3-D velocity structure surrounding the ray path in a pattern that is generally consistent with the Fresnel zones, and they are most sensitive to velocity perturbations within the first Fresnel zone (Zhang et al., 2007). The *Pn* Fresnel zone for our reference model in shown in Figure 4.3, where the first Fresnel zone coincides with the 0.03 s contour. Figure 4.3 (top) shows that once the head wave pierces the Moho (red dashed line), the Fresnel zone does not sample the crust. Cross-sections through the head wave near to the piercing point and to the center of the *Pn* path (Fig. 4.3, top) reveal that the associated Fresnel zones are in the mantle in both locations, and their widths are identical (Fig. 4.3, bottom). The vertical extent of the head wave is ~1.5 km near the piercing point and over 2 km near the center. The minimum travel time path is indicated

by the black dot near the top of the Fresnel zone (Fig. 4.3, bottom). The *P* wave velocity depth function used for minimum travel time path and Fresnel zone calculations is shown in Figure 4.2b.

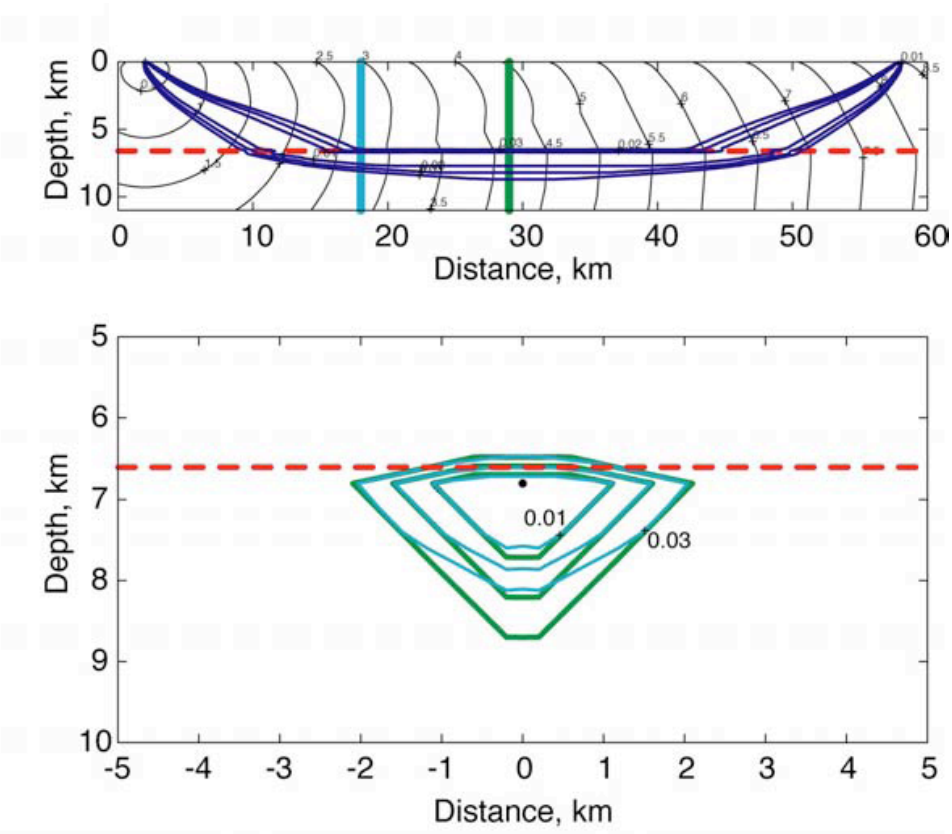

Figure 4.3. *Pn* Fresnel zones and minimum travel time paths. *P* wave velocity depth function used for these models is shown in Fig. 4.2b. (top) Travel time field for first arriving *P* waves and contours of the time difference between non-minimum time paths and the *Pn* path. The first Fresnel zone for a 10 Hz wave coincides with the outer (0.03 s) contour. Red dashed line indicates base of crust. Cyan and green vertical lines show location of cross-sections for bottom plot. (bottom) Contour plot of the time difference between non-minimum time paths and the *Pn* path (black dot) from the cyan and green cross-sections above. The first Fresnel zone coincides with the outer (0.03 s) contour.

4.3. Modeling results

Results from our finite difference waveform modeling (Table 4.1) indicate that sub-axial crustal thickness variations do not significantly affect *Pn* travel times when crustal thickness remains less than 2 km (Fig. 4.4a). Negative crustal thickness values of 1 km and 0.5 km (Models 2 and 3, respectively) generate *Pn* delay times that are less than our mean picking error (10 ms). A positive root of 0.5 km (Model 4) likewise produces a *Pn* delay time (~10 ms) that is approximate to the typical arrival time uncertainty (Fig. 4.4a). The *Pn* delay time resulting from a 1-km-thick root (Model 5) is ~20 ms, and for a crustal thickness anomaly of 2 km (Model 6) the predicted *Pn* delay time is ~60 ms, which is a more significant signal. Increasing the crustal thickness anomaly to 3 km (Model 7) or more increases the *Pn* delay to 120 ms. Amplitude variations observed in the *Pn* coda for Models 2-7 are the result of waveform interference between reflected *P* wave energy generated along the crustal root and *Pn* energy.

The effects of a ±1 km crustal thickness increase/decrease between Moho piercing points (i.e., beneath the ridge axis) on the minimum travel time path for *Pn* are illustrated in Figure 4.5. In the case of a 1 km increase (Fig. 4.5, top), the ray path dips beneath the crustal anomaly, which generates a negligible delay time (Δt=25 ms) similar to our waveform modeling results. In the case of a 1 km decrease (Fig. 4.5, bottom), the *Pn* ray path is virtually unaffected and no *Pn* delay time is observed (Δt=0 ms); this result also agrees with our waveform modeling results. Black and blue contour lines show the travel time fields for the model that includes a flat Moho and the models that include the crustal thickness anomalies, respectively.

Table 4.1. *Pn* delay times for finite difference waveform models.

Anomaly types:

CTV - Crustal thickness variation (sub-axial)

MLVZ - Mantle low-velocity zone thickness variation

MVG - Mantle velocity gradient (vertical)

VCV - Velocity contrast variation (crust-mantle)

Model #	Anomaly type	Model description	Anomaly width (km)	~ Delay time (ms)
01	N/A	Reference model (flat Moho)	N/A	N/A
02	CTV	Crustal thickness anomaly of -1.0 km	10	<10
03	CTV	Crustal thickness anomaly of -0.5 km	10	<10
04	CTV	Crustal thickness anomaly of 0.5 km	10	10
05	CTV	Crustal thickness anomaly of 1.0 km	10	20
06	CTV	Crustal thickness anomaly of 2.0 km	10	60
07	CTV	Crustal thickness anomaly of 3.0 km	10	120
08	MLVZ	MLVZ thickness of 0.5 km	10	<10
09	MLVZ	MLVZ thickness of 1.0 km	10	15
10	MLVZ	MLVZ thickness of 2.0 km	10	60
11	MLVZ	MLVZ thickness of 3.0 km	10	80
12	MLVZ	MLVZ thickness of 4.0 km	10	80
13	MVG	Velocity gradient of ~0.015 s^{-1}	N/A	<10
14	VCV	Velocity contrast of 7.1-7.6 km s^{-1}	N/A	90
15	VCV	Velocity contrast of 7.1-7.4 km s^{-1}	N/A	180

The impact of crustal thickening on the *Pn* Fresnel zone is illustrated in Figure 4.6, where a 1 km crustal thickness increase again occurs between Moho piercing points. As with the model with a flat Moho (Fig. 4.3), the *Pn* Fresnel zone does not sample the crust between Moho piercing points. The top of the Fresnel zone, however, is depressed beneath the crustal anomaly (as observed with the minimum travel time path) while the bottom of the Fresnel zone is virtually unaffected.

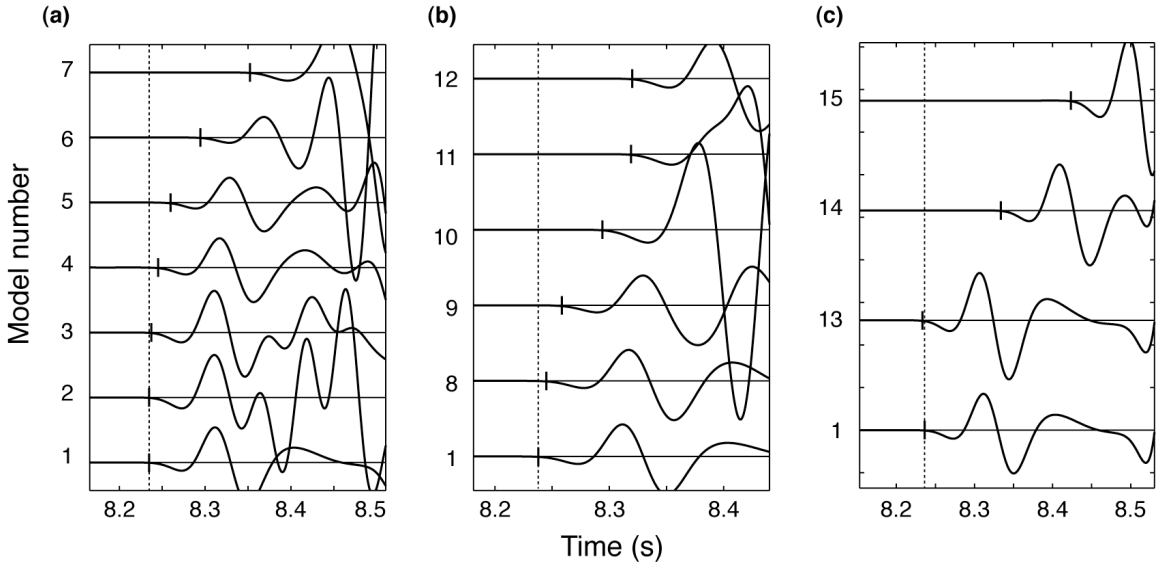

Figure 4.4. Synthetic *Pn* arrival times from finite difference modeling. *P* wave velocity depth function used for these models is shown in Fig. 4.2a. (a) *Pn* arrival times for crustal thickness variation (Models 2-7) having thickness anomalies of -1, -0.5, 0.5, 1.0, 2.0 and 3.0 km, respectively. (b) *Pn* arrival times for mantle low-velocity zone (Models 8-12) with MLVZ thicknesses of 0.5, 1.0, 2.0, 3.0 and 4.0 km, respectively. (c) *Pn* arrival times for a mantle vertical velocity gradient of ~0.015 s^{-1} (Model 13) and for crust-mantle velocity contrast variations of 7.1-7.6 and 7.1-7.4 km s^{-1} (Models 14 and 15, respectively). All arrival times are for a synthetic station located 50 km from the source. The *Pn* arrival time for the reference model (Model 1) is shown in each for comparison (dashed line).

The results from our waveform modeling (Table 4.1) associated with variations in MLZV thickness (Models 8-12) are similar to those for crustal thickness variation (Fig. 4.4b). When the MLZV is 1 km thick or less (Models 8 and 9), *Pn* delay times are negligible (<20 ms). When the MLVZ is 2 km thick (Model 10), the delay time increases to 60 ms. *Pn* delay times begin to stabilize around 80 ms, however, when the MLVZ reaches 3 km or more (Models 11 and 12). Amplitude variations are also observed in the *Pn* coda associated with the MLVZ models for the same reason noted previously.

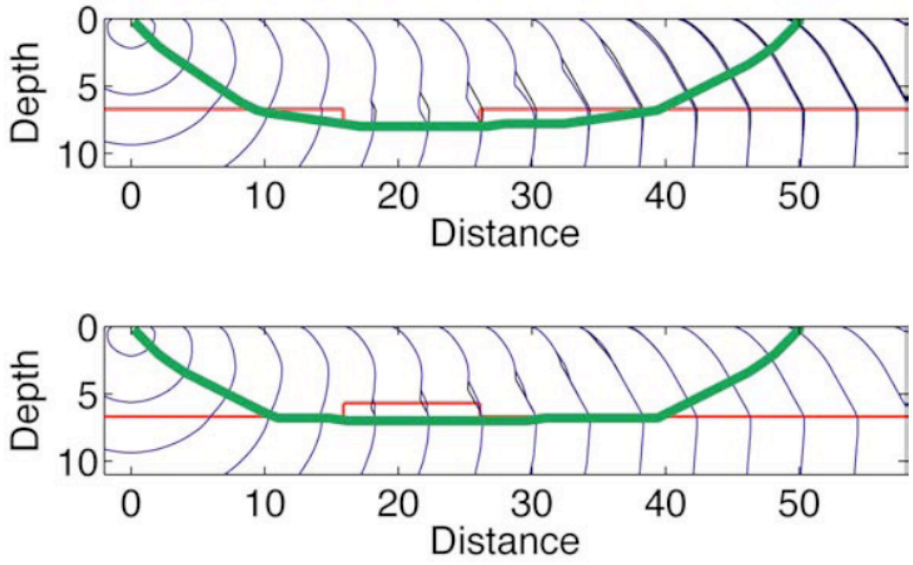

Figure 4.5. Effects of varying crustal thickness by ±1 km between *Pn* piercing points on the travel time field and the minimum time path. *P* wave velocity depth function used for these models is shown in Fig. 4.2b. For each figure, two travel time fields are contoured. Black contours are for a model with a flat Moho; blue contours are for a model that includes a 1 km change in crustal thickness. Green line is minimum time path at 50 km. Crustal thickness anomaly is 10 km wide in each case. (top) Crustal thickness is increased by 1 km. (bottom) Crustal thickness is decreased by 1 km.

Waveform modeling results (Table 4.1) show that a small, vertical velocity gradient (~0.015 s^{-1}) in the mantle also has little effect on *Pn* travel times. Model 13 (Fig. 4.4c) data show the anomalous *Pn* arrives just ahead of *Pn* in the reference model but well within our picking error (<10 ms). The slight decrease in *Pn* arrival time is a result of the higher velocity within the gradient. *Pn* delay times are larger for models with velocity contrast variations (Fig. 4.4c, Models 14 and 15). *Pn* delay times resulting from a lower crust to upper mantle velocity contrast of 7.1 to 7.6 km s^{-1} (Model 14) is ~90 ms, which is doubled to 180 ms when the mantle velocity is lowered to 7.4 km s^{-1} (Model 15).

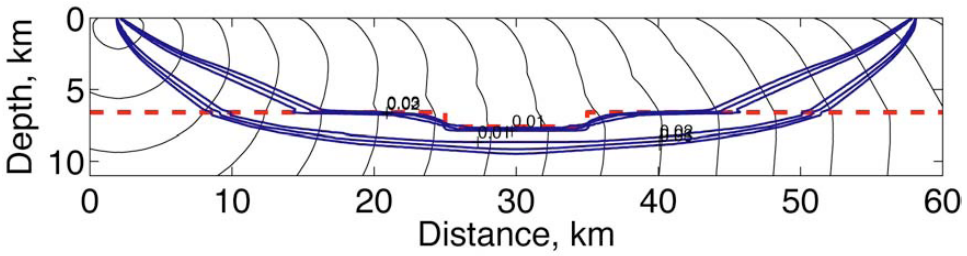

Figure 4.6. *Pn* non-minimum travel time paths for crustal thickness variation. *P* wave velocity depth function used for these models is shown in Fig. 4.2b. Effect of changing crustal thickness by 1 km on the Fresnel zone of *Pn*. Travel time field for first arriving *P* waves and contours of the time difference between non-minimum time paths and the *Pn* path. The first Fresnel zone coincides with the outer (0.03 s) contour. Red dashed line indicates base of crust.

Although *Pn* delay times associated with crust-mantle contrast variations seem significant, they result only because of changes in lower mantle velocity. This is illustrated by the fact that the *Pn* Fresnel zone does not sample the crust as shown in Figure 4.7. The *Pn* Fresnel zones associated with mantle velocities of 7.6 and 7.2 km s^{-1} are identical in shape and similar in size, and they remain in the mantle regardless of the increase in velocity contrast.

4.4. Discussion

4.4.1. Crustal thickness

Uncertainty in crustal thickness near sources and/or receivers can have a significant impact on *Pn* travel times since *Pn* energy propagates at crustal velocities between sources/receivers and Moho piercing points (or *Pn* piercing points). In the case of the Toomey et al. (2007) tomography study, however, crustal thickness beneath

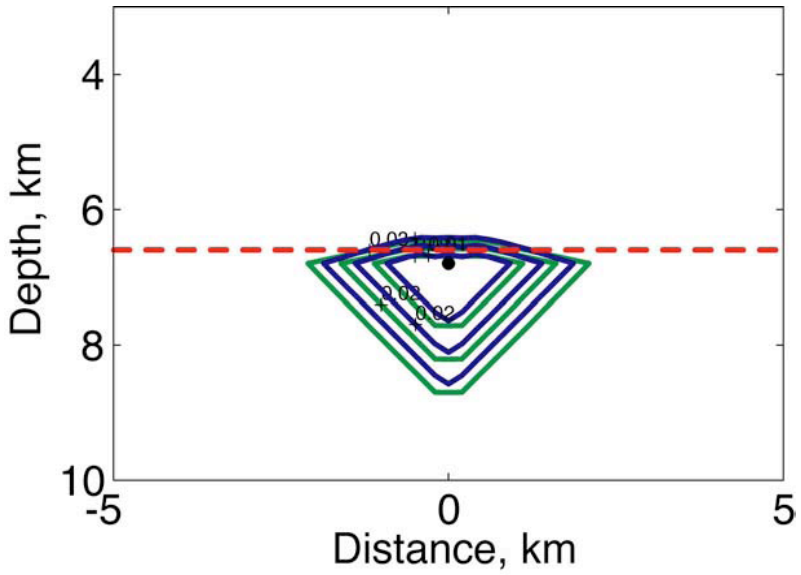

Figure 4.7. Effect of changing the crust-mantle velocity contrast on the *Pn* Fresnel zone. *P* wave velocity depth function used for these models is shown in Fig. 4.2b. Green contours are for a mantle velocity of 7.6 km s^{-1}; blue contours are for a mantle velocity of 7.2 km s^{-1}. The outer contour in each case (0.03 s) approximates the first Fresnel zone.

shooting lines and instrument locations has been measured (Barth and Mutter, 1996; Canales et al., 2003), and the off-axis crustal velocity structure is well constrained by inversions of *Pg* and *PmP* data with a common root-mean-square misfit of only 12 ms and 22 ms, respectively (Canales et al., 2003). What is less well constrained is crustal thickness below the rise axis, which creates an uncertainty in Moho topography between *Pn* piercing points. Zhang et al. (2007) show that a down-bending or up-bending of the interface between head wave piercing points compresses or stretches the travel time sensitivity kernels, which results in increased or decreased sensitivities beneath the interface topography, respectively. The maximum vertical (10 km down, 5 km up) and horizontal (35 km) dimensions of their interface perturbations, however, are far greater

that what we find beneath the fast-spreading mid-ocean ridge axis, where vertical interface uncertainty is typically considered less than ± 1 km (e.g., Barth and Mutter, 1996) over a maximum lateral distance of ~10 km (e.g., Detrick et al., 1987). We also see a compression of the *Pn* Fresnel zone associated with a 1 km crustal thickness increase (Fig. 4.6). Our travel time modeling results indicate that no significant delays are observed in *Pn* travel times until crustal thickness perturbations (i.e., changes in Moho topography) reach 2 km or more, which we consider unlikely. Therefore, normal sub-axial crustal thickness variations do not significantly affect *Pn* travel times.

4.4.2. Mantle low-velocity zone

Accurately resolving the velocity structure of the topmost mantle beneath mid-ocean ridges is critical for understanding the magma plumbing systems that drive the volcanic and hydrothermal systems observed along spreading axes. However, because travel time tomography utilizes ray theory, a first-order approximation to wave behavior where infinitely thin rays define minimum travel time paths between source and receiver (e.g., Aki and Richards, 2002; Stein and Wyssesion, 2003), uncertainty arises in the ability of *Pn* to accurately resolve mantle structure beyond Moho depths (i.e., away from the minimum travel time path). Because seismic waves do not behave like rays, some tomography methods (like that used in our referenced EPR study (Toomey et al., 2007)) compensate by integrating ray theory approximation with wave behavior using a vertical smoothing constraint that approximates the combined effects of wavefront healing and Fresnel zones (finite-frequency theory), which is argued to be a valid approximation (van der Hilst and de Hoop, 2005; de Hoop and van der Hilst, 2005). Wavefront healing

theory (Wielandt, 1987; Nolet and Dahlen, 2000) requires structural anomalies to be sufficiently large to generate significant *Pn* travel time anomalies, and Finite-frequency theory (e.g., Dahlen et al., 2000; Nolet et al., 2005; Zhang et al., 2007) accounts for travel time and amplitude sensitivities to structure both along and away from the minimum travel time path.

MLVZs with vertical extents of several kilometers are indicative of an established system of magma transport, and determining the ability of *Pn* to resolve these anomalies is critical for accurate interpretation of tomographic data. Our travel time calculations show that for a sub-axial MLZV with a vertical extent of 2 km or less, the shortest time path is below the anomaly and the predicted delay time is 5 or more times smaller than the observed range of *Pn* anomalies found in the EPR data (~350 ms). It is only when the MLVZ is 3 km or greater that the shortest time path passes through and not below the MLVZ, and resulting *Pn* delay times stabilize to a near-constant value (~80 ms). Waveform healing also requires that a velocity anomaly be of sufficient vertical extent to significantly effect *Pn* travel time (Wielandt, 1987; Nolet and Dahlen, 2000). Our modeling results, along with waveform healing theory, indicate that MLVZs must be of significant size in order to generate *Pn* delay times on the order observed in the EPR study. We note that the difference between our modeling result (Δt=~80 ms) and the range of delay times observed in the EPR study (~350 ms) may be attributed to a variety of factors not addressed in this study such as mantle anisotropy, melt transport and storage processes and thermal structure of the uppermost mantle.

4.4.3. Mantle velocity gradient

A vertical velocity gradient in the upper mantle could affect *Pn* travel times, as a head wave will become a turning wave in the presence of a sufficiently large gradient. Our modeling results, however, show that mantle velocity gradients on the order observed in fast-spreading mid-ocean ridge environments have little effect on *Pn* travel times within the range of local seismic studies (<100 km). Although using a slightly larger gradient than we use in our model (0.02 s^{-1} and 0.015 s^{-1}, respectively), Zhang et al. (2007) show that the travel time sensitivity kernel associated with the velocity gradient is about an order of magnitude less than their reference kernel over a horizontal distance almost twice that of our model. On the scale of our study, we determine that no significant *Pn* delay time occurs as a result of a mantle velocity gradient.

4.4.4. Crust-mantle velocity contrast

The velocity contrast between the lower crust and upper mantle across the Moho can also have an impact on *Pn* travel times, since *Pn* is particularly sensitive near Moho piercing points (Zhang et al., 2007). Off-axis crustal velocity structure near regions where *Pn* propagates through the crust, however, is well constrained in the EPR study (as noted above). Although a change in the velocity contrast will change the geometric ray path, the apparent velocity and overall travel time of *Pn* (Fig. 4.4c, Models 14 and 15), there is little impact on *Pn* sensitivity as demonstrated by the lack of any significant changes to the Fresnel zone (Fig. 4.7). We determine, therefore, that realistic velocity contrast variations across the Moho have little effect on *Pn* Fresnel zones or associated travel times.

This concludes the body of my work. In the next chapter, I present conclusions and inferences from all three studies.

CHAPTER V

CONCLUSIONS

Thus far, I have presented motivations, methods and outcomes for all three mid-ocean ridge studies. Here, I present the conclusions and inferences, which stem from our data and modeling results.

5.1. Off-axis crustal magmatism

On the basis of our travel time and waveform modeling, along with seismic refraction data from the UNDERSHOOT experiment (see Chapter II), we conclude or infer the following:

1) A seismic velocity and attenuation anomaly is located ~20 km east of the spreading center in 300-ka-old crust. The anomaly is the result of a crustal-level magmatic complex, which consists of a 1-km-long (±0.5 km) melt sill located at a depth of 2 km beneath the seafloor that is underlain by a broader region (4.5-km-long, ±1 km) of crust that is anomalously hot and perhaps partially molten. Attenuation within the anomaly is an order of magnitude higher than normal, off-axis oceanic crust.

2) Waveform data can better resolve relatively small crustal magma bodies like the one we detect when compared to two-dimensional travel time tomographic methods.

3) The high-attenuation LVV we detect is consistent with the injection of a significant amount of heat into the ridge flank and marks a site of repeated intrusive activity, which we attribute to underlying mantle melt accumulation.

4) The off-axis delivery of mantle melt gives rise to magmatic underplating and intrusive activity that thickens both the MTZ and the crust, thereby fundamentally altering crustal architecture. Repeated intrusive activity may act as a source for off-axis lava flows and drive off-axis hydrothermal circulation.

5.2. Axial depth and crustal density variation

On the bases of our thermodynamic modeling results, along with geochemical and geophysical observations along the 9°-10°N region of the EPR (see Chapter III), we conclude or infer the following:

1) Crustal density variations on the order inferred along the northern EPR (~0.1 g/cm^3) can result from differences in both crystallization depth and degree of fractionation (i.e., magma chamber residence time).

2) Regions where lower crustal formation occurs by a combination of deep crystallization and longer AMC residence times have higher average crustal density than those where the lower crust is generated by subsiding cumulates originating within the AMC with shorter residence times.

3) Cumulate density variations are primarily attributed to differences in the crystallization sequence of major mineral phases at different pressures, especially that of clinopyroxene. An increase in the percentage of clinopyroxene within the cumulate assemblage can sufficiently increase average cumulate density by as much as 0.1 g/cm^3.

4) Our modeling results support the magma differentiation hypothesis and quantitatively link segment-scale variations in axial depth and crustal density to segment-scale variations in crystallization depth. In this view, axial highs are associated with magmatic systems that crystallize melt preferentially within upper-crustal magma bodies. Conversely, along-axis deeps are associated with magmatic systems that have significant near-Moho crystallization, a condition that we attribute to off-axis delivery of mantle melt.

5.3. *Pn* sensitivity in travel time tomography

On the basis of our results from ray tracing, waveform modeling and Fresnel zone calculations (see Chapter IV), we conclude or infer the following:

1) Sub-axial crustal thickness variations do not significantly effect *Pn* travel times until crustal thickness reaches 2 km or more, which is beyond realistic uncertainty.

2) Mantle low-velocity anomalies must be at least 2 km thick to be detectable and at least 3 km thick in order to generate stabilized, near-constant *Pn* delay times that are significant.

3) A vertical velocity gradient in the upper mantle, as well as crust-mantle velocity contrast variations across the Moho, prove to be inconsequential to *Pn* travel time uncertainties under the conditions found along the northern EPR.

4) Vertical smoothing constrains utilized by Toomey et al. (2007) in their local travel time tomography method do an effective job at approximating *Pn* wave behavior, and our findings support the validity and interpretation of their tomographic results.

5.4. Concluding thoughts

Since the mid-twentieth century, marine geoscientists have endeavored to unravel the complexities of mid-ocean ridge processes. A great deal of progress has been made over the past couple of decades, mostly due to improvements in technology, yet many questions remain unanswered. Although the discovery of off-axis melt accumulation along the northern EPR adds another level of complexity, the results of our first two studies show that it provides a logical means by which we can explain several enigmatic observations like off-axis volcanic and hydrothermal activity as well as axial depth variation along fast-spreading ridges. The results of our work also indicate that mid-ocean ridge research should be expanded to include more off-axis studies, especially in regions overlying mantle melt accumulation. Other topics such as processes for lateral, sub-crustal melt flow or potential thickening of the MTZ associated with the off-axis delivery of mantle melt to the rise axis we leave for future study.

As for our *Pn* study, our results eliminate several potential factors that could affect *Pn* travel times and resulting travel time tomography interpretations. However, the question remains as to what may yet affect head waves and resulting travel times in the mid-ocean ridge environment. Although we have suggested possible factors to explain the difference between the range of *Pn* delay times observed in the UNDERSHOOT data (~350 ms) and our modeling results (~80 ms), more work is required to fully answer this question. The solution could prove to be consequential to our understanding of the thermal structure of the uppermost mantle as well as melt transport and storage processes beneath mid-ocean ridges. We leave answering this question to future study as well.

APPENDIX A

WAVEFORM MODEL PARAMETERIZATION

We use E3D, an explicit 2D/3D elastic finite difference wave propagation code that is 4^{th}-order accurate in space and 2^{nd}-order accurate in time, for our finite difference modeling (Larsen and Harris, 1993; Levander, 1988). The finite difference crustal model consists of a 5001 x 1401 nodal grid with a 10 m nodal spacing in the horizontal and vertical directions (50 x 14 km^2). Absorbing boundary conditions are used on the sides and bottom and a free surface boundary condition at the top. Some reflecting energy, however, remains within the model space. To further reduce boundary effects, we add additional nodes to the sides and bottom that make the overall model dimensions 7001 x 2001 nodes (70 x 20 km^2) (Fig. A.1a). We place a 5-km-wide high attenuation (Q = 5) boundary along the sides and bottom as well (Fig. A.1b). Topography is excluded from the model. For most models, the layer 2A-2B velocity discontinuity is replaced by a continuous gradient in order to remove the many converted phases that are outside the scope of our study. Crustal Vp/Vs ratios and Q values are slightly modified from Vera et al. (1990) and Wilcock et al. (1992), respectively (Fig. A.1), and crustal densities (ρ) are calculated using the density-velocity relationship $\rho = 0.165Vp + 1.852$ (Christensen and Shaw, 1970). The source consists of a Ricker wavelet with a center frequency of 10 Hz. Shots (1 per run) are spaced at 1 km intervals and begin 10 m below sea level. We perform 51 separate runs for each synthetic model (one for each shot position) in order to construct record sections that are comparable to data. Synthetic data are band-pass filtered between 5 and 30 Hz.

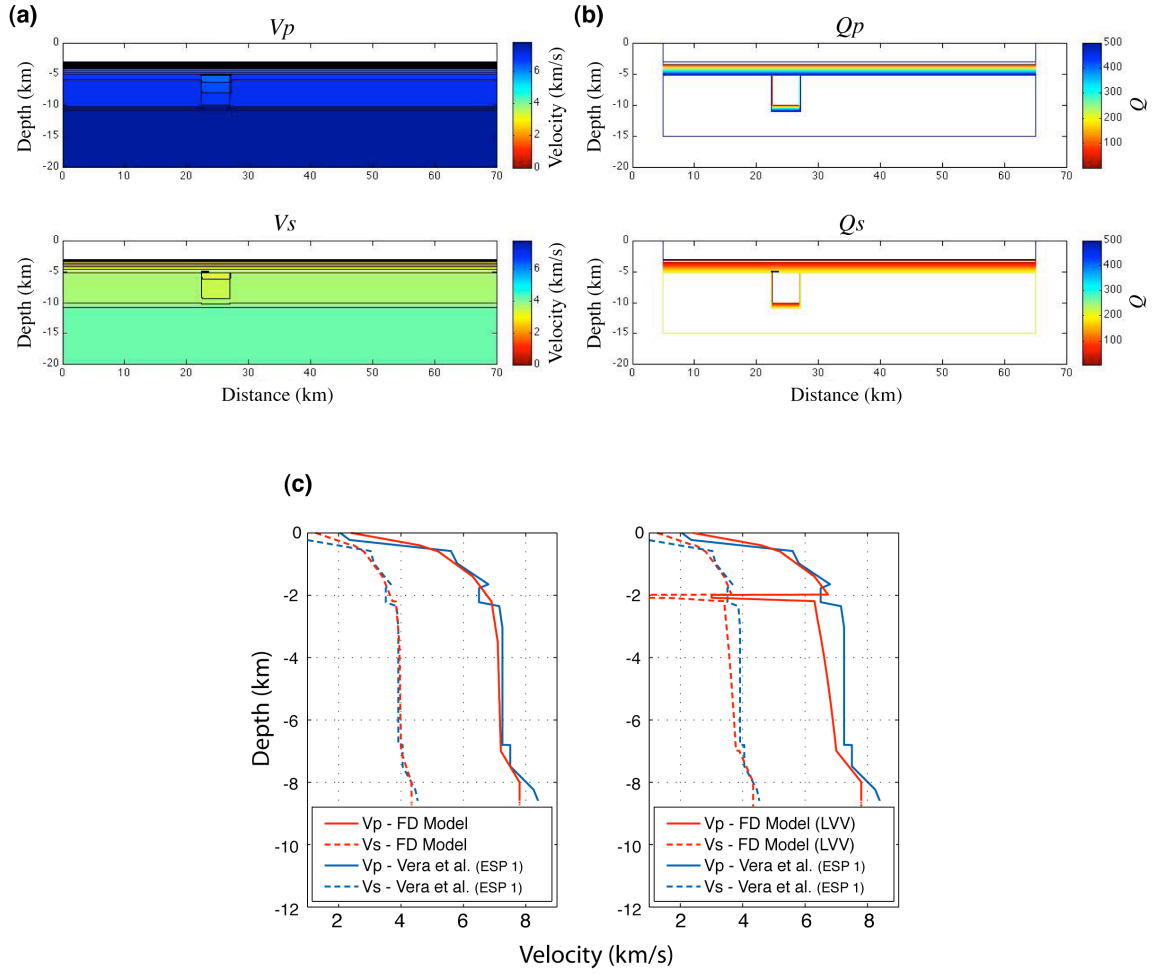

Figure A.1. Preferred finite difference model. (a) velocity contours; *P* wave (top) and *S* wave (bottom), (b) attenuation contours; *Qp* (top) and *Qs* (bottom); *Q* contours show the side and bottom boundaries added to reduce model boundary effects, (c) velocity-depth functions outside the LVV region (left) and within the LVV region (right); a velocity-depth profile from Vera et al. (1990) is shown for comparison.

APPENDIX B

HEAT CALCULATIONS

We estimate the amount of heat being injected into the ridge flank by calculating the amount of heat required to generate the velocity anomaly observed in our seismic data. We use the velocity and attenuation results from our modeling and add a 1-km-width to our LVV. We begin with the temperature derivative of seismic velocity κ (Karato, 1993),

$$\kappa = \frac{\partial \ln V}{\partial T} = \frac{\partial \ln V_0}{\partial T} - F(\alpha)\left(\frac{Q^{-1}(\omega,T)}{\pi}\right)\left(\frac{H^*}{RT^2}\right). \quad (1)$$

where V_0 is a reference velocity corresponding to the unrelaxed state of the medium, Q^{-1} is the reciprocal of the quality factor, ω is frequency, T is temperature, H^* is activation enthalpy, R is the gas constant and $F(\alpha) = (\pi\alpha/2)\cot(\pi\alpha/2)$ where α is the exponent of the power law dependence of Q on frequency ($Q \sim \omega^{\alpha}$). The first term in this equation represents anharmonic effects (no seismic energy loss), and the second term represents anelastic effects (entails seismic energy loss). Anelasticity can significantly increase the temperature derivative, thereby reducing the thermal anomaly required to generate the observed velocity anomaly. To obtain a minimum value for the thermal anomaly, we maximize the effects of anelasticity by setting $F(\alpha) = 1$. We use a value of -8.1×10^{-5} K^{-1} for the anharmonic term (Christensen, 1979), and use the following values for the remaining variables: $Q^{-1} = 0.02$ (a viable estimate from our modeling results), $H^* = 276$ kJ mol^{-1} (Caristan, 1982)) and $R = 8.314$ J mol^{-1} K^{-1}. For T, we use 400, 600 and 800 °C,

which is a range of average mid-crustal temperatures expected for normal off-axis crust (Dunn et al., 2000; Maclennan et al., 2005). Using these values in Eqn. (1) gives us the following solutions for κ_n, where n = 400, 600 and 800: κ_{400} = -5.47×10^{-4} K^{-1}, κ_{600} = -3.58×10^{-4} K^{-1} and κ_{800} = -2.65×10^{-4} K^{-1}. Figure B.1a shows that the magnitude of κ decreases with increasing Q as anelastic effects diminish.

To determine the temperature anomaly associated with each value of κ, we use the relation

$$\partial Vp = \kappa Vp \, \partial \mathrm{T}. \tag{2}$$

We estimate the derivatives in Eqn. (2) by using Δ and rearrange the equation to get

$$\Delta T_n = \frac{\Delta Vp}{\kappa_n Vp_{\mathrm{crust}}} \quad (n = 400, 600, 800). \tag{3}$$

ΔVp (ΔVp = -0.3 km s^{-1}) is determined by taking the average of the velocity values within the modeled LVV (Vp_{LVV} = 6.7 km s^{-1}) and comparing it to the average mid- to lower-crustal velocity value near OBS 51 (Vp_{crust} = 7.0 km s^{-1}) (Canales et al., 2003). Using our values for κ_n and ΔVp, we get the following solutions for ΔT_n: ΔT_{400} = 78 °C, ΔT_{600} = 120 °C and ΔT_{800} = 162 °C. These ΔT values assume a Q value of 50 everywhere, however Figure B.1b shows that as Q increases the thermal anomaly required to generate the observed velocity anomaly also increases.

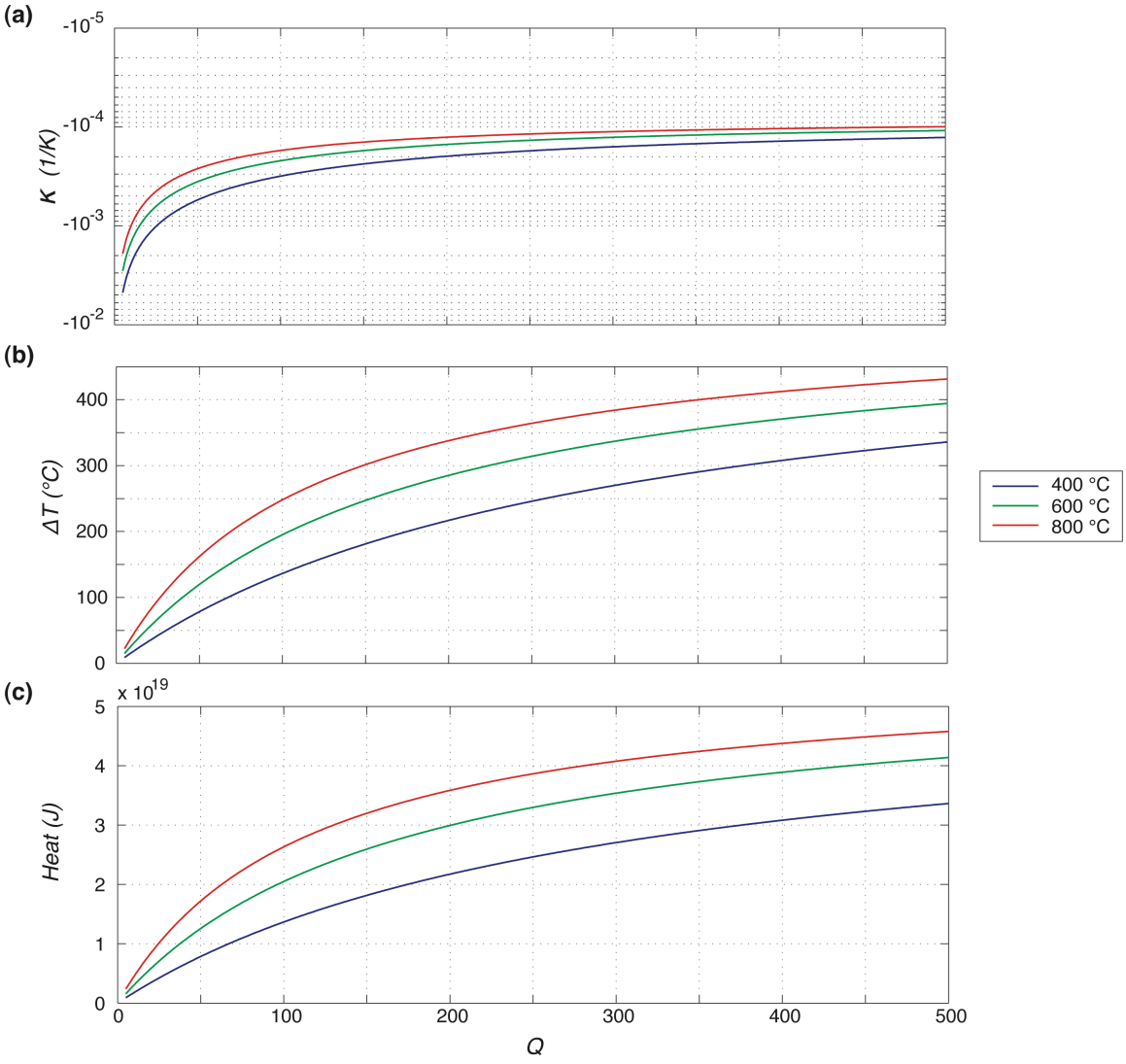

Figure B.1. Heat calculation variables and their relationships with the quality factor Q. Calculations for all three variables are made using crustal temperatures of 400, 600 and 800 °C as shown, (a) temperature derivative of seismic velocity κ (Eqn. (1)) with respect to Q, (b) temperature anomaly ΔT (Eqn. (3)) with respect to Q, (c) heat (Eqn. (4)) with respect to Q. Values in (b) and (c) are based upon a velocity anomaly of -0.3 km s^{-1}.

We calculate the amount of heat (Q_{heat}) required to generate the temperature anomaly within the LVV using the standard heat equation,

$$Q_{\text{heat}}(n) = m_{\text{LVV}} Cp_n \Delta T_n \quad (n = 400, 600, 800), \tag{4}$$

where m_{LVV} is the mass of the rock within the LVV, Cp_n is the specific heat capacity of the rock at constant pressure and ΔT_n is change in temperature. Using the density of gabbro (ρ_{gabbro} = 2970 kg m^{-3}) (Waples and Waples, 2004) and an LVV volume of 22.5 km^3 (4.5 km L × 5 km H × 1 km W), we get $m_{\text{LVV}} = 6.7 \times 10^{13}$ kg. Because specific heat capacity is temperature dependent, we use the method of Waples and Waples (2004) to calculate values for Cp_n. The regression equation

$$Cp_{n_T} = 8.95 \times 10^{-10} T^3 - 2.13 \times 10^{-6} T^2 + 0.00172T + 0.716 \tag{5}$$

gives us a normalized heat capacity of a mineral or nonporous rock at any temperature T (°C). As long as a measured value for the specific heat capacity (Cp_{T1}) is available for the rock or mineral at any given temperature T_1, then Eqn. (6) can be used to calculate the theoretical specific heat capacity (Cp_{T2}) for the same rock or mineral at a new temperature T_2:

$$Cp_{T_2} = Cp_{T_1} \left(\frac{Cp_{n_{T_2}}}{Cp_{n_{T_1}}} \right). \tag{6}$$

We thus obtain the following values for the specific heat capacity of gabbro (Cp_n), where the measured value for gabbro is 1000 J kg^{-1} K^{-1} at 20 °C (Waples and Waples, 2004): Cp_{400} = 1495 J kg^{-1} K^{-1}, Cp_{600} = 1567 J kg^{-1} K^{-1} and Cp_{800} = 1584 J kg^{-1} K^{-1}. Using our values for m_{LVV}, Cp_n and ΔT_n in Eqn. (4) gives us the following solutions for heat: $Q_{heat}(400) = 7.5 \times 10^{18}$ J, $Q_{heat}(600) = 1.2 \times 10^{19}$ J and $Q_{heat}(800) = 1.6 \times 10^{19}$ J. From these solutions, we use an estimate of 1×10^{19} J for the amount of heat being injected into the ridge flank at our study site. Figure B.1c illustrates that the amount of heat required to generate a specific velocity anomaly increases with respect to increasing Q, thus our heat estimate via a Q value of 50 is rather conservative. Similar analyses using velocity anomalies (ΔVp) of -0.2 and -0.1 km s^{-1} for comparison yield a reduction in heat values of 33 and 66%, respectively.

To estimate the heat contributed by a single melt sill, like the one in our model, we calculate the amount of heat given off during sill solidification. We use a value of 5.0 $\times 10^5$ J kg^{-1} for the latent heat of crystallization for basaltic melts in the crust (Cannat et al., 2004). A melt density of 2600 kg m^{-3} and a sill volume of 0.1 km^3 (1 km L × 0.1 km H × 1 km W) yields a mass for the melt sill of 2.60×10^{11} kg. If the sill were to totally crystallize, it would generate ~1.3×10^{17} J of heat (latent heat of crystallization × mass), which is less than 2% of the estimated heat required to generate the observed LVV.

REFERENCES CITED

Chapter I

Batiza, R., Niu, Y., 1992. Petrology and magma chamber processes at the East Pacific Rise ~9°30'N. J. Geophys. Res. 97 (B5), 6779-6797.

Buck, W. R., Su, W., 1989. Focused mantle upwelling below mid-ocean ridges due to feedback between viscosity and melting. Geophys. Res. Lett. 16 (7), 641-644.

Carbotte, S., Macdonald, K., 1992. East Pacific Rise 8°-10°30′N: Evolution of ridge segments and discontinuities from SeaMARC II and three-dimensional magnetic studies. J. Geophys. Res., 97 (B5), 6959-6982.

Durant, D. T., Toomey, D. R., 2009. Evidence and implications of crustal magmatism on the flanks of the East Pacific Rise. Earth Planet. Sci. Lett. 287 (1-2), 130-136.

Gripp, A. E., Gordan, R. G., 2002. Young tracks of hotspots and current plate velocities. Geophys. J. Int. 150 (2), 321-361.

Haymon, R. M., Fornari, D. J., Edwards, M. H., Carbotte, S., Wright, D., Macdonald, K. C., 1991. Hydrothermal vent distribution along the East Pacific Rise crest (9°09'-54'N) and its relationship to magmatic and tectonic processes on fast-spreading mid-ocean ridges. Earth Planet. Sci. Lett. 104 (2-4), 513-534.

Langmuir, C., Bender, J., Batiza, R., 1986. Petrologic and tectonic segmentation of the East Pacific Rise from 6°-14°N. Nature 332, 422-429.

Macdonald, K. C., Fox, P. J., Perram, L. J., Eisen, M. F., Haymon, R. M., Miller, S. P., Carbotte, S. M., Cormier, M.-H., Shor, A. N., 1988. A new view of the mid-ocean ridge from the behaviour of ridge-axis discontinuities. Nature 335, 217-225.

Macdonald, K. C., Scheirer, D. S., Carbotte, and S. M., 1991. Mid-ocean ridges: discontinuities, segments, and giant cracks. Science 253, 986-994.

Perfit, M. R., Fornari, D. J., Smith, M. C., Bender, J. F., Langmuir, C. H., Haymon, R. M., 1994. Small-scale spatial and temporal variations in mid-ocean ridge crest magmatic processes. Geology 22 (4), 375-379.

Phipps Morgan, J., 1987. Melt migration beneath mid-ocean spreading centers. Geophys. Res. Lett. 14 (12), 1238-1241.

Phipps Morgan, J., Chen, Y. J., 1993. Dependence of ridge-axis morphology on magma supply and spreading rate. Nature 364, 706-708.

Scheirer, D. S., Macdonald, K. C., 1993. Variation in cross-sectional area of the axial ridge along the East Pacific Rise: Evidence for the magmatic budget of a fast-spreading center. J. Geophys. Res. 98 (B5), 7871-7885.

Smith, M. C., Perfit, M. R., Fornari, D. J., Ridley, W. I., Edwards, M. H., Kurras, G. J., Von Damm, K. L., 2001. Magmatic processes and segmentation at a fast spreading mid-ocean ridge: Detailed investigation of an axial discontinuity on the East Pacific Rise crest at 9°37′N. Geochem. Geophys. Geosyst. 2, 1040.

Toomey, D. R., Jousselin, D., Dunn, R. A., Wilcock, W. S. D., Detrick, R. S., 2007. Skew of mantle upwelling beneath the East Pacific Rise governs segmentation. Nature 446, 409-414.

Chapter II

Bazin, S., Harding, A. J., Kent, G. M., Orcutt, J. A., Tong, C. H., Pye, J. W., Singh, S. C., Barton, P. J., Sinha, M. C., White, R. S., Hobbs, R. W., Van Avendonk, H. J. A., 2001. Three-dimensional shallow crustal emplacement at the 9°03'N overlapping spreading center on the East Pacific Rise: Correlations between magnetization and tomographic images. J. Geophys. Res. 106 (B8), 16101-16117.

Canales, J. P., Detrick, R. S., Toomey, D. R., Wilcock, W. S. D., 2003. Segment-scale variations in the crustal structure of 150-300 kyr old fast spreading oceanic crust (East Pacific Rise, 8º15'N-10º5'N) from wide-angle seismic refraction profiles. Geophys. J. Int. 152, 766-794.

Cannat, M., Cann, J., Maclennan, J., 2004. Some hard rock constraints on the supply of heat to mid-ocean ridges, in: German, C. R., Lin, J., Parson, L. M. (Eds.), Mid-Ocean Ridges: Hydrothermal Interactions Between the Lithosphere and Oceans. Geophysical Monograph 148, American Geophysical Union, Washington, D. C., pp. 111-149.

Caristan, Y., 1982. The transition from high temperature creep to fracture in Maryland diabase. J. Geophys. Res. 87 (B8), 6781-6790.

Christensen, N. I., 1979. Compressional wave velocities in rocks at high temperatures and pressures, critical thermal gradients, and crustal low-velocity zones. J. Geophys. Res. 84 (B12), 6849-6857.

Christensen, N. I., Shaw, G. H., 1970. Elasticity of mafic rocks from the Mid-Atlantic Ridge. Geophys. J. Int. 20, 271-284.

Christeson, G. L., Shaw, P. R., Garmany, J. D., 1997. Shear and compressional wave structure of the East Pacific Rise, 9º-10º N. J. Geophys. Res. 102 (B4), 7821-7835.

Detrick, R. S., Buhl, P., Vera, E., Mutter, J., Orcutt, J., Madsen, J., Brocher, T., 1987. Multi-channel seismic imaging of a crustal magma chamber along the East Pacific Rise. Nature 326, 35-41.

Dunn, R. A., Toomey, D. R., Solomon, S. C., 2000. Three-dimensional seismic structure and physical properties of the crust and shallow mantle beneath the East Pacific Rise at 9°30'N. J. Geophys. Res. 105 (B10), 23537-23555.

Feig, S. T., Koepke, J., Snow, J. E., 2006. Effect of water on tholeiitic basalt phase equilibria: an experimental study under oxidizing conditions. Contrib. Mineral. Petrol. 152, 611-638.

Fornari, D. J., Haymon, R. M., Perfit, M. R., Gregg, T. K. P., Edwards, M. H., 1998. Axial summit trough of the East Pacific Rise 9°-10°N: Geological characteristics and evolution of the axial zone on fast spreading mid-ocean ridges. J. Geophys. Res. 103 (B5), 9827-9855.

Garmany, J., 1989. Accumulations of melt at the base of young oceanic crust. Nature 340, 628-632.

Haymon, R. M., Fornari, D. J., Edwards, M. H., Carbotte, S., Wright, D., Macdonald, K. C., 1991. Hydrothermal vent distribution along the East Pacific Rise crest (9°09'-54'N) and its relationship to magmatic and tectonic processes on fast-spreading mid-ocean ridges. Earth Planet. Sci. Lett. 104 (2-4), 513-534.

Haymon, R. M., Macdonald, K. C., Benjamin, S. B., Ehrhardt, C. J., 2005. Manifestations of hydrothermal discharge from young abyssal hills on the fast-spreading East Pacific Rise flank. Geology 33, 153-156.

Juteau, T., Ernewein, M., Reuber, I., Whitechurch, H., Dahl, R., 1988. Duality of magmatism in the plutonic sequence of the Sumail Nappe, Oman. Tectonophysics 151, 107-135.

Karato, S., 1993. Importance of anelasticity in the interpretation of seismic tomography. Geophys. Res. Lett. 20 (15), 1623-1626.

Kent, G. M., Harding, A. J., Orcutt, J. A., 1990. Evidence for a smaller magma chamber beneath the East Pacific Rise at 9°30'N. Nature 344, 650-653.

Korenaga, J., Kelemen, P. B., 1997. Origin of gabbro sills in the Moho transition zone of the Oman ophiolite: Implications for magma transport in the oceanic lower crust. J. Geophys. Res. 102 (B12), 27729-27749.

Larsen, S., Harris, D., 1993. Seismic wave propagation through a low-velocity nuclear rubble zone. Lawrence Livermore Natl. Lab. Tech. Rep. UCRL-ID-115729.

Levander, A., 1988. Fourth-order finite-difference P-SV seismograms. Geophysics 53, 1425-1436.

Macdonald, K. C., Fox, P. J., 1988. The axial summit graben and cross-sectional shape of the East Pacific Rise as indicators of axial magma chambers and recent volcanic eruptions. Earth Planet. Sci. Lett. 88 (1-2), 119-131.

Maclennan, J., Hulme, T., Singh, S. C., 2005. Cooling of the lower oceanic crust. Geology 33, 357-366.

Nicolas, A., Boudier, F., Ildefonse, B., 1996. Variable crustal thickness in the Oman ophiolite: Implication for oceanic crust. J. Geophys. Res. 101 (B8), 17941-17950.

Nicolas, A., Mainprice, D., 2005. Burst of high-temperature seawater injection throughout accreting oceanic crust: a case study in Oman ophiolite. Terra Nova 17, 326-330.

Sims, K. W. W., Blichert-Toft, J., Fornari, D. J., Perfit, M. R., Goldstein, S. J., Johnson, P., DePaolo, D. J., Hart, S. R., Murrell, M. T., Michael, P. J., Layne, G. D., Ball, L. A., 2003. Aberrant youth: Chemical and isotopic constraints on the origin of off-axis lavas from the East Pacific Rise, 9°-10° N. Geochem. Geophys. Geosys. 4, 8621.

Singh, S. C., Kent, G. M., Collier, J. S., Harding, A. J., Orcutt, J. A., 1998. Melt to mush variations in crustal magma properties along the ridge crest at the southern East Pacific Rise. Nature 394, 874-878.

Toomey, D. R., Hooft, E. E. E., 2008. Mantle upwelling, magmatic differentiation, and the meaning of axial depth at fast-spreading ridges. Geology 36, 679-682.

Toomey, D. R., Jousselin, D., Dunn, R. A., Wilcock, W. S. D., Detrick, R. S., 2007. Skew of mantle upwelling beneath the East Pacific Rise governs segmentation. Nature 446, 409-414.

Toomey, D. R., Solomon, S. C., Purdy, G. M., 1994. Tomographic imaging of the shallow crustal structure of the East Pacific Rise at 9°30'N. J. Geophys. Res. 99 (B12), 24135-24157.

Vera, E. E., Mutter, J. C., Buhl, P., Orcutt, J. A., Harding, A. J., Kappus, M. E., Detrick, R. S., Brocher, T. M., 1990. The structure of 0- to 0.2-m.y.-old oceanic crust at 9°N on the East Pacific Rise from Expanded Spread Profiles. J. Geophys. Res. 95 (B10), 15529-15556.

Waples, D. W., Waples, J. S., 2004. A review and evaluation of specific heat capacities of rocks, minerals, and subsurface fluids. Part 1: Minerals and nonporous rocks. Nat. Resour. Res. 13, 97-122.

Wilcock, W. S. D., Dougherty, M. E., Solomon, S. C., Purdy, G. M., Toomey, D. R., 1993. Seismic propagation across the East Pacific Rise: Finite difference experiments and implications for seismic tomography. J. Geophys. Res. 98 (B11), 19913-19932.

Wilcock, W. S. D., Solomon, S. C., Purdy, G. M., Toomey, D. R., 1992. The seismic attenuation structure of a fast-spreading mid-ocean ridge. Science 258, 1470-1474.

Zou, H., Zindler, A., Niu, Y., 2002. Constraints on melt movement beneath the East Pacific Rise from ^{230}Th-^{238}U disequilibrium. Science 295, 107-110.

Chapter III

Allan, J. F., Batiza, R., Perfit, M. R., Fornari, D. J., Sack, R. O., 1989. Petrology of lavas from the Lamont Seamount chain and adjacent East Pacific Rise, 10°N. J. Petrol 30 (5), 1245-1298.

Asimow, P. D., Ghiorso, M. S., 1998. Algorithmic modifications extending MELTS to calculate subsolidus phase relations. Am. Mineral. 83, 1127-1132.

Barth, G. A., Mutter, J. C., 1996. Variability in oceanic crustal thickness and structure: Multichannel seismic reflection results from the northern East Pacific Rise. J. Geophys. Res. 101 (B8), 17951-17975.

Batiza, R., Allan, J. F., Bach, W., Boström, K., Brophy, J. G., Fryer, G. J., Goldstein, S. J., Harpp, K., Haymon, R. M., Hekinian, R., Johnston, J. E., Niu, Y., Polyak, B. G., 1995. Petrology, geochemistry and petrogenesis of Leg 142 basalts – Synthesis of results. Proc. ODP, Sci. Results 142, 3-8.

Batiza, R., Niu, Y., 1992. Petrology and magma chamber processes at the East Pacific Rise ~9°30'N. J. Geophys. Res. 97 (B5), 6779-6797.

Batiza, R., Niu, Y., Karsten, J. L., Boger, W., Potts, E., Norby, L., Butler, R., 1996. Steady and non-steady state magma chambers below the East Pacific Rise. Geophys. Res. Lett. 23 (3), 221-224.

Bezos, A., Humler, E., 2005. The $Fe^{3+}/\Sigma Fe$ ratios of MORB glasses and their implications for mantle melting. Geochim. Cosmochim. Acta 69 (3), 711-725.

Boudier, F., Nicolas, A., Ildefonse, B., 1996. Magma chambers in the Oman ophiolite: Fed from the top and the bottom. Earth Planet. Sci. Lett. 144 (1-2), 239-250.

Canales, J. P., Detrick, R. S., Toomey, D. R., Wilcock, W. S. D., 2003. Segment-scale variations in the crustal structure of 150-300 kyr old fast spreading oceanic crust (East Pacific Rise, 8º15'N-10º5'N) from wide-angle seismic refraction profiles. Geophys. J. Int. 152, 766-794.

Carbotte, S., Macdonald, K., 1992. East Pacific Rise 8°-10°30′N: Evolution of ridge segments and discontinuities from SeaMARC II and three-dimensional magnetic studies. J. Geophys. Res., 97 (B5), 6959-6982.

Carbotte, S.M., Small, C., Donnelly, K., 2004. The influence of ridge migration on the magmatic segmentation of mid-ocean ridges. Nature 429, 743-746.

Carlson, R., Herrick, C., 1990. Densities and porosities in the oceanic crust and their variations with depth and age. J. Geophys. Res. 95 (B6), 9153-9170.

Combier, V., Singh, S., Cannat, M., Escartin, J., 2008. Mechanical decoupling and thermal structure at the East Pacific Rise axis 9°N: Constraints from axial magma chamber geometry and seafloor structures. Earth Planet. Sci. Lett. 272 (1-2), 19-28.

Coogan, L. A., Gillis, K. M., MacLeod, C. J., Thompson, G. M., Hékinian, R., 2002. Petrology and geochemistry of the lower ocean crust formed at the East Pacific Rise and exposed at Hess Deep: A synthesis and new results. Geochem. Geophys. Geosyst. 3 (11), 1-30.

Danyushevsky, L.V., Eggins, S. M., Falloon, T. J., Christie, D. M., 2000. H_2O Abundance in depleted to moderately enriched mid-ocean ridge magmas; Part I: Incompatible behaviour, implications for mantle storage, and origin of regional variations. J. Petrol. 41 (8), 1329-1364.

Detrick, R. S., Buhl, P., Vera, E. E., Mutter, J. C., Orcutt, J. A., Madsen, J. A., Brocher, T. M., 1987. Multi-channel seismic imaging of a crustal magma chamber along the East Pacific Rise. Nature 326, 35-41.

Detrick, R. S., Needham, H. D., Renard, V., 1995. Gravity anomalies and crustal thickness variations along the Mid-Atlantic Ridge between 33°N and 40°N. J. Geophys. Res. 100 (B3), 3767-3787.

Dunn, R. A., Toomey, D. R., Solomon, S. C., 2000. Three-dimensional seismic structure and physical properties of the crust and shallow mantle beneath the East Pacific Rise at 9°30'N. J. Geophys. Res. 105 (B10), 23537-23555.

Durant, D. T., Toomey, D. R., 2009. Evidence and implications of crustal magmatism on the flanks of the East Pacific Rise. Earth Planet. Sci. Lett. 287 (1-2), 130-136.

Fornari, D. J., Haymon, R. M., Perfit, M. R., Gregg, T. K. P., Edwards, M. H., 1998. Axial summit trough of the East Pacific Rise 9°-10°N: Geological characteristics and evolution of the axial zone on fast spreading mid-ocean ridges. J. Geophys. Res. 103 (B5), 9827-9855.

Ghiorso, M. S., Sack, R. O., 1995. Chemical mass transfer in magmatic processes IV: A revised and internally consistent thermodynamic model for the interpolation and extrapolation of liquid-solid equilibria in magmatic systems at elevated temperatures and pressures. Contrib. Mineral. Petrol. 119 (2-3), 197-212.

Ghiorso, M. S., 1997. Thermodynamic models of igneous processes. Annu. Rev. Earth Planet. Sci. 25 (1), 221-241.

Goss, A. R., Perfit, M. R., Ridley, W. I., Rubin, K. H., Kamenov, G. D., Soule, S. A., Fundis, A., Fornari, D.J., 2010. Geochemistry of lavas from the 2005-2006 eruption at the East Pacific Rise, 9°46′N-9°56′N: Implications for ridge crest plumbing and decadal changes in magma chamber compositions. Geochem. Geophys. Geosyst. 11, Q05T09.

Grove, T. L., Kinzler, R. J., Bryan, W. B., 1992. Fractionation of mid-ocean ridge basalt (MORB), in: Morgan, J. P., Blackman, D. K., Sinton, J. M. (Eds.), Mantle Flow and Melt Generation at Mid-ocean Ridges. Geophysical Monograph 71, American Geophysical Union, Washington, D. C., pp. 281-310.

Haymon, R. M., Fornari, D. J., Edwards, M. H., Carbotte, S., Wright, D., Macdonald, K. C., 1991. Hydrothermal vent distribution along the East Pacific Rise crest (9°09'-54'N) and its relationship to magmatic and tectonic processes on fast-spreading mid-ocean ridges. Earth Planet. Sci. Lett. 104 (2-4), 513-534.

Henstock, T. J., Woods, A. W., White, R. S., 1993. The accretion of oceanic crust by episodic sill intrusion. J. Geophys. Res. 98 (B3), 4143-4161.

Hooft, E. E. E., Detrick, R. S., Toomey, D. R., Collins, J. A., Lin, J., 2000. Crustal thickness and structure along the axial valley of three contrasting spreading segments of the Mid-Atlantic Ridge, 33.5º-35ºN. J. Geophys. Res. 105 (B4), 8205-8226.

Iturrino, G. J., Christensen, N. I., Kirby, S., Salisbury, M. H., 1991. Seismic velocities and elastic properties of oceanic gabbroic rocks from Hole 735B. Proc. Ocean Drill. Program Sci. Results, 118, 227-244.

Kelemen, P. B., Koga, K., Shimizu, N., 1997. Geochemistry of gabbro sills in the crust-mantle transition zone of the Oman Ophiolite: Implications for the origin of the oceanic lower crust. Earth Planet. Sci. Lett. 146 (3-4), 475-488.

Kelemen, P. B., Aharonov, E., 1998. Periodic formation of magma fractures and generation of layered gabbros in the lower crust beneath oceanic spreading ridges, in: Buck, W. R., Delaney, P. T., Karson, J. A., Lagabrielle, Y. (Eds.), Faulting and Magmatism at Mid-Ocean Ridges, Geophysical Monograph 106, American Geophysical Union, Washington, D. C., pp. 267-289.

Kent, G. M., Harding, A. J., Orcutt, J. A., 1993. Distribution of magma beneath the East Pacific Rise between the Clipperton Transform and the 9º17'N Deval from forward modeling of common depth point data. J. Geophys. Res. 98 (B8), 13945-13970.

Klein, E. M., Langmuir, C. H., 1987. Global correlations of ocean ridge basalt chemistry with axial depth and crustal thickness. J. Geophys. Res. 92 (B8), 8089-8115.

Korenaga, J., Kelemen, P. B., 1997. Origin of gabbro sills in the Moho transition zone of the Oman ophiolite: Implications for magma transport in the oceanic lower crust. J. Geophys. Res. 102 (B12), 27729-27749.

Langmuir, C. H., 1989. Geochemical consequences of in situ differentiation. Nature 340, 199-205.

Langmuir, C. H., 1999. Submitted data set: Major and trace element composition of basalt glasses from the CHEPR cruise, East Pacific Rise. Retrieved from http://www.petdb.org

Langmuir, C. H., Bender, J. F., Batiza, R., 1986. Petrological and tectonic segmentation of the East Pacific Rise, 5º30'-14º30'N. Nature 322, 422-429.

Lehnert K., Su, Y., Langmuir, C. H., Sarbas, B., Nohl, U., 2000. A global geochemical database structure for rocks. Geochem. Geophys. Geosyst. 1, 1012.

le Roux, P., Shirey, S., Hauri, E., Perfit, M., 2006. The effects of variable sources, processes and contaminants on the composition of northern EPR MORB (8-10°N and 12-14°N): Evidence from volatiles (H_2O, CO_2, S) and halogens (F, Cl). Earth Planet. Sci. Lett. 251 (3-4), 209-231.

Lin, J., Purdy, G. M., Schouten, H., Sempere, J.-C., Zervas, C., 1990. Evidence from gravity data for focused magmatic accretion along the Mid-Atlantic Ridge. Nature 344, 627-632.

Macdonald, K. C., Fox, P. J., Perram, L. J., Eisen, M. F., Haymon, R. M., Miller, S. P., Carbotte, S. M., Cormier, M.-H., Shor, A. N., 1988. A new view of the mid-ocean ridge from the behaviour of ridge-axis discontinuities. Nature 335, 217-225.

Macdonald, K. C., Scheirer, D. S., Carbotte, and S. M., 1991. Mid-ocean ridges: discontinuities, segments, and giant cracks. Science 253, 986-994.

Madsen, J. A., Detrick, R. S., Mutter, J. C., Buhl, P., Orcutt, J. A., 1990. A two- and three-dimensional analysis of gravity anomalies associated with the East Pacific Rise at 9°N and 13°N. J. Geophys. Res. 95 (B4), 4967-4987.

Melson, W. G., O'Hearn, T., 2003. Smithsonian volcanic glass file. Retrieved from http://www.petdb.org

Michael, P. J., Chase, R. L., 1987. The influence of primary magma composition, H_2O and pressure on mid-ocean ridge basalt differentiation. Contrib. Mineral. Petrol. 96 (2), 245-263.

Natland, J. H., Dick, H. J. B., 2009. Paired melt lenses at the East Pacific Rise and the pattern of melt flow through the gabbroic layer at a fast-spreading ridge. Lithos 112 (1-2), 73-86.

Nicolas, A., Boudier, F., Ceuleneer, G., 1988. Mantle flow patterns and magma chambers at ocean ridges: Evidence from the Oman ophiolite. Mar. Geophys. Res. 9 (4), 293-310.

Pan, Y., Batiza, R., 2003. Magmatic processes under mid-ocean ridges: A detailed mineralogic study of lavas from East Pacific Rise 9°30′N, 10°30′N, and 11°20′N. Geochem. Geophys. Geosyst. 4 (11), 1-33.

Perfit, M. R., 2000. Submitted data set: Major element compositions of basalt glasses from the East Pacific Rise, 9°N. Retrieved from http://www.petdb.org

Perfit, M. R., Fornari, D. J., Smith, M. C., Bender, J. F., Langmuir, C. H., Haymon, R. M., 1994. Small-scale spatial and temporal variations in mid-ocean ridge crest magmatic processes. Geology 22 (4), 375-379.

Perfit, M. R., Fornari, D. J., Ridley, W. I., Kirk, P. D., Casey, J., Kastens, K. A., Reynolds, J. R., Edwards, M., Desonie, D., Shuster, R., Paradis, S., 1996. Recent volcanism in the Siqueiros transform fault: Picritic basalts and implications for MORB magma genesis. Earth Planet. Sci. Lett. 141 (1-4), 91-108.

Perfit, M. R., Chadwick Jr., W. W., 1998. Magmatism at mid-ocean ridges: Constraints from volcanological and geochemical investigations, in: Buck, W. R., Delaney, P. T., Karson, J. A., Lagabrielle, Y. (Eds.), Faulting and Magmatism at Mid-Ocean Ridges, Geophysical Monograph 106, American Geophysical Union, Washington, D. C., pp. 59-115.

Perk, N. W., Coogan, L. A., Karson, J. A., Klein, E. M., Hanna, H. D., 2007. Petrology and geochemistry of primitive lower oceanic crust from Pito Deep: implications for the accretion of the lower crust at the Southern East Pacific Rise. Contrib. Mineral. Petrol. 154 (5), 575-590.

Phipps Morgan, J., Chen, Y. J., 1993. The genesis of oceanic crust: Magma injection, hydrothermal cooling, and crustal flow. J. Geophys. Res. 98 (B4), 6283-6297.

Quick, J. E., Denlinger, R. P., 1993. Ductile deformation and the origin of layered gabbro in ophiolites. J. Geophys. Res. 98 (B8), 14015-14027.

Schouten, H., Denham, C., 1995. Virtual ocean crust. EOS 76, S48.

Smith, M. C., Perfit, M. R., Fornari, D. J., Ridley, W. I., Edwards, M. H., Kurras, G. J., Von Damm, K. L., 2001. Magmatic processes and segmentation at a fast spreading mid-ocean ridge: Detailed investigation of an axial discontinuity on the East Pacific Rise crest at 9°37′N. Geochem. Geophys. Geosyst. 2, 1040.

Tighe, S. A., Detrick, R. S., Fox, P. J., Langmuir, C. H., Mutter, J. C., Ryan, W. B., Tyce, R. C., 1988. East Pacific Rise Data Synthesis Final Report, Vol. 1, Joint Oceanographic Institutions, Inc., Washington, D.C.

Tolstoy, M., Harding, A. J., Orcutt, J. A., 1993. Crustal thickness on the Mid-Atlantic Ridge: Bull's-eye gravity anomalies and focused accretion. Science 262, 726-729.

Toomey, D. R., Hooft, E. E. E., 2008. Mantle upwelling, magmatic differentiation, and the meaning of axial depth at fast-spreading ridges. Geology 36 (9), 679-682.

Toomey, D. R., Jousselin, D., Dunn, R. A., Wilcock, W. S. D., Detrick, R. S., 2007. Skew of mantle upwelling beneath the East Pacific Rise governs segmentation. Nature 446, 409-414.

Toomey, D. R., Purdy, G. M., Solomon, S. C., Wilcock, W. S. D., 1990. The three-dimensional seismic velocity structure of the East Pacific Rise near latitude 9°30'N. Nature 347, 639-645.

Villiger, S., Müntener, O., Ulmer, P., 2007. Crystallization pressures of mid-ocean ridge basalts derived from major element variations of glasses from equilibrium and fractional crystallization experiments. J. Geophys. Res. 112, B01202.

Wang, X., Cochran, J. R., Barth, G. A., 1996. Gravity anomalies, crustal thickness, and the pattern of mantle flow at the fast spreading East Pacific Rise, 9°-10°N: Evidence for three-dimensional upwelling. J. Geophys. Res. 101 (B8), 17927-17940.

White, S. M., Mason, J. L., Macdonald, K. C., Perfit, M. R., Wanless, V. D., Klein, E. M., 2009. Significance of widespread low effusion rate eruptions over the past two million years for delivery of magma to the overlapping spreading centers at 9°N East Pacific Rise. Earth Planet. Sci. Lett. 280 (1-4), 175-184.

Chapter IV

Aki, K., Richards, P. G., 2002. Quantitative Seismology, second ed., University Science Books, Sausalito, CA.

Barth, G. A., Mutter, J. C., 1996. Variability in oceanic crustal thickness and structure: Multichannel seismic reflection results from the northern East Pacific Rise. J. Geophys. Res. 101 (B8), 17951-17975.

Canales, J. P., Detrick, R. S., Toomey, D. R., Wilcock, W. S. D., 2003. Segment-scale variations in the crustal structure of 150-300 kyr old fast spreading oceanic crust (East Pacific Rise, 8º15'N-10º5'N) from wide-angle seismic refraction profiles. Geophys. J. Int. 152, 766-794.

Dahlen, F. A., Hung, S. H., Nolet, G., 2000. Frechet kernels for finite-frequency traveltimes - I. Theory. Geophys. J. Int. 141, 157-174.

de Hoop, M. V., Van der Hilst, R. D., 2005. Reply to comment by F. A. Dahlen and G. Nolet on: "On sensitivity kernels for 'wave-equation' transmission tomography." Geophys. J. Int. 163, 952-955.

Detrick, R. S., Buhl, P., Vera, E., Mutter, J., Orcutt, J., Madsen, J., Brocher, T., 1987. Multi-channel seismic imaging of a crustal magma chamber along the East Pacific Rise. Nature 326, 35-41.

Dunn, R. A., Toomey, D. R., Solomon, S. C., 2000. Three-dimensional seismic structure and physical properties of the crust and shallow mantle beneath the East Pacific Rise at 9°30'N. J. Geophys. Res. 105 (B10), 23537-23555.

Durant, D. T., Toomey, D. R., 2009. Evidence and implications of crustal magmatism on the flanks of the East Pacific Rise. Earth Planet. Sci. Lett. 287 (1-2), 130-136.

Larsen, S., Harris, D., 1993. Seismic wave propagation through a low-velocity nuclear rubble zone. Lawrence Livermore Natl. Lab. Tech. Rep. UCRL-ID-115729.

Levander, A., 1988. Fourth-order finite-difference P-SV seismograms. Geophysics 53 (11), 1425-1436.

Moser, T. J., 1991. Shortest path calculation of seismic rays. Geophysics 56 (1), 59-67.

Nolet, G., Dahlen, F. A., 2000. Wave front healing and the evolution of seismic delay times. J. Geophys. Res. 105 (B8), 19043-19054.

Nolet, G., Dahlen, F. A., Montelli, R., 2005. Traveltimes and amplitudes of seismic waves: a re-assessment, in: Levander, A., Nolet, G. (Eds.), Seismic Earth: Analysis of broadband seismograms, Geophysical Monograph 157, American Geophysical Union, Washington, D. C., pp. 37-48.

Stein, S., Wysession, M., 2003. An Introduction to Seismology, Earthquakes, and Earth Structure, Blackwell Publishing Ltd., Malden, MA.

Toomey, D. R., Jousselin, D., Dunn, R. A., Wilcock, W. S. D., Detrick, R. S., 2007. Skew of mantle upwelling beneath the East Pacific Rise governs segmentation. Nature 446, 409-414.

Toomey, D. R., Solomon, S. C., Purdy, G. M., 1994. Tomographic imaging of the shallow crustal structure of the East Pacific Rise at 9°30'N. J. Geophys. Res. 99 (B12), 24135-24157.

van der Hilst, R. D., de Hoop, M. V., 2005. Banana-doughnut kernels and mantle tomography. Geophys. J. Int. 163, 956-961.

Wielandt, E., 1987. On the validity of the ray approximation for interpreting delay times in: Nolet, G. (Ed.), Seismic Tomography, Reidel, Dordrecht, pp. 85-98.

Zhang, Z., Shen, Y., Zhao, L., 2007. Finite-frequency sensitivity kernels for head waves. Geophys. J. Int. 171, 847-856.

Chapter V and Appendices

See Chapter II references.